Ions in MXene: Characterization and Control of Interlayer Cations and their Effects on Structure and Properties of 2D Transition Metal Carbides

A Thesis Submitted to the Faculty of Drexel University

by

Michael John Ghidiu

in partial fulfillment of the

requirements for the degree

of

Doctor of Philosophy

June 2018

DEDICATIONS

Growth as a person, as a researcher, has only come

Under the umbrella of support,

Year after year, of family –

Some chosen, some not

This is dedicated to them

ACKNOWLEDGMENTS

I have a great deal of gratitude for those who have helped me through all aspects of the time spent during the course of this research. First and foremost, for my adviser, Prof. Michel Barsoum, who has encouraged and led me to be independently functioning with great academic freedom since the very beginning; for his unwavering support through personal struggles; and for instilling scientific curiosity and rigor. I would like to thank Prof. Yury Gogotsi for helping to mold me as a scientist and for the seemingly unlimited resources he has offered, including helping to initiate many collaborations. It is difficult to overstate what a solid base my faculty mentors have provided me with.

I would like to thank all of my committee members: Profs. Michel Barsoum, Yury Gogotsi, Caroline Schauer, Steven May, and Aaron Fafarman, for their continued time and support through the development and evaluation of this work.

Many collaborations have been necessary for some of the most fundamental work of this project: Prof. David Bish of Indiana University, Prof. Vadym Mochalin of Missouri University of Science and Technology (and formerly of Drexel University), Dr. Vadym Drozd of Florida International University. Their time, expertise, and assistance has been invaluable. Further, work at Drexel University required the technical expertise and time of the staff at the Centralized Research Facilities (CRF), specifically Drs. Edward Basgall and Dmitri Barbash.

I would like to thank everyone in the Drexel MSE community for helping to ease some burdens of the program and make the entire course of studies a deeper

experience. Particularly my peers who helped with this work through chats, critiques, mentoring, and assistance in the laboratory, as well as continued friendship and support: Drs. Michael Naguib, Joseph Halim, Darin Tallman, Kelsey Hatzell, Katie van Aken, Maria Lukatskaya, and Olya Mashtalir; Sankalp Kota, Matthias Agne, Cooper Voigt, Andrew Lang, Elisa Mayerberger, and Jamie Hart.

The funding that has made this research possible has come from generous grants from Drexel University (Provost Fellowship), the National Science Foundation, and primarily the National Science Foundation Graduate Research Fellowship Program (grant No. 283036-3304; any opinions, findings, and conclusions or recommendations expressed in this material are those of the author and do not necessarily reflect the views of the NSF). Funding for parts of the work presented here has also come from the Swedish Research Council (Vetenskapsrådet), as well as the Swedish Foundation for Strategic Research through the Synergy Grant FUNCASE (Functional Carbides for Advanced Surface Engineering).

My time in the program could not have gone smoothly without the behind-the-scenes staff at the Drexel MSE department: Keiko Nakazawa, Yenneeka Long, Sarit Kunz, Danielle Kopicko. They have been helpful, resourceful, and always ready to answer my many questions, especially when presented in a rushed nature.

Finally, I want to say that this would not have been possible without the tireless support and encouragement of my family and friends.

TABLE OF CONTENTS

List of common abbreviations in this work

2D	Two-Dimensional
AA	Alkylammonium
CEC	Cation Exchange Capacity
CV	Cyclic Voltammetry
DAC	Diamond Anvil Cell
DFT	Density Functional Theory
EDS	Energy-Dispersive Spectroscopy
LDH	Layered Double Hydroxide
LIB	Lithium Ion Battery
LP	Lattice Parameter
MD	Molecular Dynamics
ML	Multilayer
RH	Relative Humidity
SEM	Scanning Electron Microscopy
TEM	Transmission Electron Microscopy
TGA	Thermogravimetric Analysis
TMD	Transition Metal Dichalcogenide
WAXS	Wide-Angle X-ray Scattering
XPS	X-ray Photoelectron Spectroscopy
XRD	X-Ray Diffraction

LIST OF TABLES

LIST OF FIGURES

ABSTRACT

Ions in MXene: Characterization and Control of Interlayer Cations and their Effects on Structure and Properties of 2D Transition Metal Carbides

Michael John Ghidiu

Adviser: Prof. Michel Barsoum

MXene, a new family of materials comprised of ternary carbonitrides of the early transition metals, has exploded into the field of two-dimensional materials since their discovery in 2011. They draw interest due especially to their unique combinations of hydrophilicity and high electrical conductivity with extremely large compositional variability. Since their introduction, they had been explored in applications of ion-intercalation-based energy storage, *i.e.* lithium-ion batteries and electrochemical capacitors (supercapacitors), and had been hailed as 'conductive clays', but no major work had been undertaken to provide a more detailed picture of the structural effects of chemically-intercalated ions and what exactly 'clay-like' behavior meant in the context of MXene.

This work endeavored to fill this gap in the literature, focusing primarily on $Ti_3C_2T_x$, the most well-studied MXene (where T is a variable surface termination of the nanosheets). Based on a review of various literatures, we define 'clay-like' properties to include intercalated ions that are exchangeable and that can influence dynamic structural responses to the host material to stimuli, based on the chemistry of the intercalated ions. We successfully intercalated, by chemical means alone, cations of alkali metals (Li^+, Na^+, K^+, Rb^+, Cs^+), alkaline earth metals (Mg^{2+}, Ca^{2+}), transition

metals (Mn^{2+}, Fe^{2+}, Co^{2+}, Ni^{2+}), and alkylammonium cations of the form $[(CH_3)_3NC_nH_{2n+1}]^+$, where *n* ranges from 1 to 16. We have also demonstrated control of exchange of initially-intercalated cations to other cations; X-ray photoelectron spectroscopy and X-ray diffraction results confirm that the process is a true exchange, as experienced in clay minerals.

For the alkali and alkaline earth metal cations, we have found that the basal planes of the host MXene expand and contract their interlayer distance when H_2O enters and leaves the structure, and that the magnitude of this response correlates with the hydration enthalpy of the intercalated cation. This is a quantitative link to the same phenomena experienced in clays. The transition metal-intercalated samples also demonstrated similar expansion from intercalated H_2O. In addition, in $Ti_3C_2T_x$ without added cations, we found an effect of pseudonegative compressibility along the *c* axis; that is, when pressure was applied in the presence of H_2O, the basal spacing *expanded*. This was determined to be due to the forced intercalation of H_2O, and the presence of intercalated K^+ was found to hamper this effect. Such expansion was known in the literature of other materials, but we have found shearing of the nanosheets with respect to one another to be a potential cause.

For the alkylammonium cation-intercalated samples, we observed a discontinuous expansion in the basal spacing correlated to the chain length of the intercalated organocations; this was quantitatively described both by simple volume-packing arguments as well as by more sophisticated computational results. This further led to a determination of the ion-exchange capacity of $Ti_3C_2T_x$. The results were found to be analogous to those of the clay minerals, providing further strength in

the connection between MXenes and clays. Finally, the intercalation of alkylammonium cations was expanded to both Ti_2CT_2 and Nb_2CT_x, to demonstrate compatibility and universality with both changes to n (of $M_{n+1}X_nT_x$) as well as with changes to the transition metal M; these samples demonstrated the same kind of discontinuous expansion in basal spacing.

CHAPTER 1 - INTRODUCTION

Though the history of naturally occurring and man-made nanomaterials is a long one, the associated phenomena began to be described by quantum size effects in the 20th century when it was realized that structurally identical materials could demonstrate very different properties when the size of the sample was decreased to the nanoscale.[1] Materials were described as being zero-, one-, two-, or three-dimensional based on how many dimensions were invariable and on the nanoscale. The field of two-dimensional (2D) materials was jump-started in 2004-2005 when graphene was isolated in large crystals and its unique properties began to be studied experimentally. Graphite, a 3D material, is composed of stacked sheets of carbon in hexagonal arrangement, each sheet one atom thick. Isolation of these sheets (named with the -ene suffix to reflect the sp^2 bonding of the carbon atoms) and exploration of their properties revealed some very interesting phenomena: zero-gap semiconduction, ballistic conductivity, high carrier mobility, and high mechanical strength, with high transparency to visible light. Thus the material was hailed as having high potential in applications in the fields of electronics (such as new transistor materials) and optoelectronics.

Other 2D materials were quickly added to the growing family: hexagonal boron nitride (hBN), transition metal dichalcogenides, oxides and hydroxides, clay minerals, silicene, germanene, phosphorene, stannene, and many others. Each was shown to have very interesting properties, but most of these materials had little compositional variation (and hence property tunability) aside from surface

modification. For example, graphene can be changed from a zero-gap to a p-type semiconductor by addition of metal particles, but its chemical composition and structure is limited. The same is true of most groups of 2D materials.

A strong answer to these limitations came in 2011 with the introduction of MXene, yet another new member to the 2D family.[2] This material is of the form $M_{n+1}X_nT_x$, where M is an early transition metal, X is carbon and/or nitrogen, and T is a variable surface termination. First and foremost, it offers an immense compositional variability unlike the other groups of 2D materials. The M sites can be occupied by a large variety of transition metals, and are not limited to pure elements; random solid solutions of multiple metals, as well as various modes of structural ordering of the atoms, have been demonstrated.[3,4] The X sites can be occupied by carbon, nitrogen, or solid solutions of both.[5] The thickness of the MX blocks, denoted by *n*, is variable and easily controlled; this can lead to *e.g.* differences in reactivity and conductivity. Further, a new dimension of control is introduced that other 2D materials lack: variable bending ridigity.[6] T stands in for a variable surface termination. The groups on the MXene surface have been predicted to have a very strong influence on properties.[7]

Taken together, the ability to precisely control structure, and as a result properties, with a broad palette, is one of the driving factors of MXene's success, and one that sets it apart from other materials. Further, MXene has many other inherent attractive properties. It is hydrophilic (a main limitation to the ease of processing graphene is that it is hydrophobic, and for bulk processing in water, surfactants or conversion to graphene oxide must be used). It has high densities of mobile electronic

carriers, leading to excellent conductivities, while maintaining good optical transparency.[8]

Nearly since its inception, MXene was named a 'conductive clay' due to its high electronic conductivity, hydrophilicity, and ability to interact with ions.[9] However, at the start of this project, what was missing from the literature was a comprehensive and quantitative study on what it meant for MXene to be 'clay-like'. This work attempts to outline such properties, to explore dynamic response of MXene structure to stimuli that are commonly found in the clay literature, to outline how to control the structure and resulting properties, and to understand where they fit into practicality.

CHAPTER 2 - BACKGROUND AND LITERATURE REVIEW

2.1 - Introduction to layered intercalation compounds

Layered materials encompass many diverse structures and compositions that feature thin sheets of material stacked to make larger particles, with interlayer spaces in between the sheets. Sheet thickness is generally on the order of the nanoscale. Lateral dimensions can range from nm to cm and beyond. Some common examples of these materials are graphite, dichalcogenides, and clay minerals. One of the most important reactions with these materials is *intercalation* – the insertion or removal of ions, molecules, or other species, in between the stacked layers. This process can cause changes to the volume of the interlayer space or other structural parameters,[10,11] change the surface chemistry of the host (*e.g.* from hydrophilic to hydrophobic),[12] endow the material with dynamic responses to changes in environment,[13,14,15] or even drastically change the electronic structure of the host material.[16]

2.1.1 Clay-like materials

Clay minerals have been known and used since the dawn of humankind, and still represent important materials for everyday life and industrial applications such as soil science, agriculture, industrial products, and oil and gas. These materials are based on the structure of phyllosilicates, which are composed of stacked sheets of silicate tetrahedra. The silicon, e.g. Si^{4+} in tetrahedra, can be isomorphously substituted with elements of lower charge such as Al^{3+}; this leads to a permanent negative charge in the sheets.[10] The charge is then balanced by cations that sit in the interlayer space (Fig. 2.1). Charges can also arise from other means such as

(de)protonation of surface hydroxyl groups;[17] while this mechanism can be important *e.g.* for clays in soils, it is not a focus for this work. Important aspects of intercalated cations is that they can be mobile within the structure,[18] and can be exchanged for different cations.[10] Based on the fraction of atoms in the host structure that are isomorphously substituted with lower-charge replacements, the material will have an inherent number of cations per formula unit that balance the charge (which can be described in terms of various densities such as volumetric or areal), but not all may be easily removed.

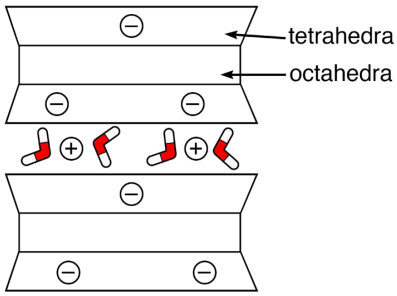

Figure 2.1: Basic simplified structure of montmorillonite, containing cations and hydrating H2O molecules in a monolayer configuration. The different layers are composed of octahedra or tetrahedra.

The *cation exchange capacity* (CEC) describes the fraction of these that are exchangeable. A vast variety of cations can sit in the interlayer space, from alkali and alkaline earth metals,[19,20] to transition metals,[21] to ammonium-based and other polyatomic cations.[11] The intercalated ion can cause the basal spacing of the layered host to change, based on the size and electronic structure of the ions.[22] Ammonium ions are especially attractive due to their wide structural variety – the basal spacing of clays can be easily tailored,[12] and even toggled between multiple spacings

dynamically using external stimuli such as UV irradiation in the case of cations containing azobenzene moieties (which have a thermal and UV-activated *cis-trans* isomerization.[14]

Ions, based on their chemical properties, have an affinity for H_2O molecules, which can organize into hydration shells; the affinity is described thermodynamically by the hydration enthalpy (which generally follows the same trend as volumetric charge density of the ions).[10] When the ions are intercalated, H_2O can enter the structure to hydrate the ions. If the electrostatic forces holding the layers and ions of the host together are exceeded by the driving force of ion hydration, the layers can be pushed apart. This happens typically in a uniform manner across the structure, and as such is called *crystalline swelling*.[23] The expansions are linked to the relative humidity (thermodynamically, the activity of water) of the atmosphere.[20] Generally, this process is reversible (with some hysteresis),[24] with H_2O de-intercalating as the humidity is decreased. Molecules such as alcohols and other organic solvents are also able to intercalate,[25] but their treatment is beyond the scope of this work. The intercalation of H_2O is especially relevant due to the common occurrence of clay/water systems in nature, such as in agriculture or in geologic processes.

The intercalation often has a tendency to proceed stepwise, with changes in layer spacing corresponding roughly to dimensions of the H_2O molecule.[20] The intercalated H_2O can be arranged in a monolayer (Fig. 2.2a), a bilayer (Fig. 2.2b), or regularly interstratified phases (Fig. 2.2c), as well as random interstratifications. Osmotic swelling can occur, where H_2O enters in excess of the hydration shells of the ions and pushes the clay layers apart even further.[26] Of course, the H_2O molecules

don't necessarily stack in discreet layers even though this is implied by the term 'bilayer' – rather, they can form a hydration shell around each ion;[27] larger hydration shells (larger coordination number) lead to expansion of the clay layers, and the hydration shell is oriented so that multiple H_2O fit into the vertical space of the interlayer.

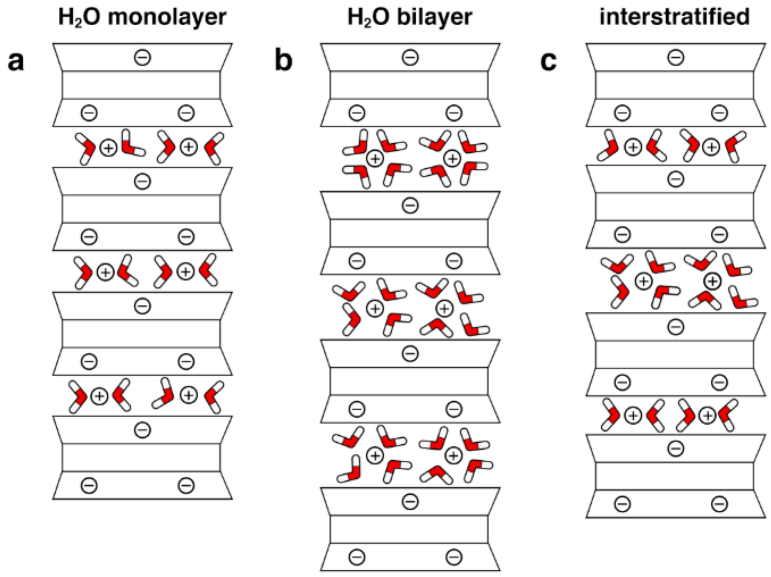

Figure 2.2: Select types of crystalline swelling in clay minerals: a) monolayer of H_2O molecules; b) bilayer of H_2O; c) interstratified mono- and bilayers. Note that the orientation of H_2O molecules is not meant to be representative of their actual orientations.

Similar materials are layered titanates,[28,29] and the layered double hydroxides (LDH).[30,31] The former, like clay minerals, are comprised of nanosheets holding negative charge, balanced by intercalated cations. The negative charge can arise from isomorphous substitution of lower-valence metals or from titanium vacancies.[32] Layered double hydroxides are opposite of clay minerals in that their isomorphous substitution (of *e.g.* Al^{3+} for Mg^{2+}) creates a net positive charge on the sheets, which is counterbalanced by interlayer anions.[30] The materials can display many of the same

type of behaviors as clay minerals such as ion exchange, crystalline swelling,[33] and delamination,[34] with properties determined in part by the anion characteristics such as hydration enthalpy.[31] Like clay minerals, both layered titanates and LDH can be naturally occurring or synthesized and have found use in applications of ion exchange, as sorbents, and as catalysts.[35]

A final example is that of a structure that does not begin with an inherent charge due to substitution. Transition metal dichalcogenides (TMDs) have the general structure MX_2, where M is a transition metal and X is a chalcogen (S, Se, or Te); they are generally layered, with strong in-plane bonding and week sheet-to-sheet bonding.[36] Separated into individual nanosheets, 2D TMDs show unique properties that can be useful in applications like transistors and optoelectronics.[37] With no isomorphous substitution in the parent layered structure, there is no inherent charge developed on the sheets. However, it was found that reacting TMDs with elemental alkali metals, such as Li, could cause a donation of the valence shell electron from the alkali metal into the lowest unoccupied levels (transition metal d bands) of the TMD, resulting in negatively charged sheets with intercalated cations.[38] Because of the charge transfer, the cations were found to be exchangeable, and even more clay-like behaviors such as crystalline swelling have been observed.[39] Furthermore, as in clay minerals, ammonium-based cations have also been explored.[39,40]

If the individual sheets of a layered material can be pulled apart to a sufficient separation, they can be permanently removed from the original structure. This general process is called either *delamination* or *exfoliation*, depending upon whom one asks. Mechanically, it was one of the earlier methods of producing large sheets of graphene

which led to a Nobel prize.[41] If performed in a solvent, and the energy of the sheets being solvated is lower than that of the sheets restacking, then a suspension can be formed; the stability of these colloidal suspensions is described by zeta (ζ) potential, which describes the potential difference between the bulk dispersion medium and that surrounding the suspended particles. A zeta potential of high magnitude amounts to particles that tend to repel each other, hence forming a stable suspension rather than aggregating and precipitating. The process of delamination can be assisted by intercalation to help separate the layers, ultrasonication, or surfactants to help stabilize nanosheets in the chosen solvent.[42]

Given this introduction to clays and clay-like materials, the purpose of this work is, in a large part, to define "clay-like behavior" and evaluate MXene in this regard. Based on analysis of various literatures, we define some essentials of this behavior as:

1. Composition of nanosheets that are weakly bonded to each other (relative to bonding within each sheet), and separable (delamination).
2. A host material able to hold inherent charge, with permanent interlayer ions counterbalancing that charge.
3. Ability to exchange the interlayer ions, with the potential for structure and properties to change, dependent upon the ions.
4. Possibility of crystalline swelling.

2.1.2 Dimensionality in materials

Because the sheet-to-sheet bonding in these types of layered materials (electrostatic or van der Waals) is much weaker than the bonding within the sheets (covalent), the nanosheets can often be readily separated and isolated. The crystal

structure of each nanosheet has infinite lateral dimensions but is constrained in thickness, so the material is called two-dimensional (2D), even though it is not two-dimensional in the mathematical sense. Materials can also be zero-, one-, or three-dimensional as well. The dimensionality of a material is determined by the number of infinite dimensions of the crystal structure, or in other words, the number of dimensions that are variable without altering the structural definition and hence properties of the material. Using macroscale examples (Fig. 2.3), a ball bearing (0D) is defined by its diameter, with no dimensions variable; a metal rod is defined by its diameter as well, but length is variable without changing its classification (1D); metal sheeting is defined by its thickness, regardless of length or width (2D); and a bulk metal ingot need not be constrained in length, width, or thickness (3D). Carbon materials are used here as nanoscale examples: C_{60} 'buckyballs' as 0D, carbon nanotubes as 1D, graphene as 2D, and graphite as 3D. Layered materials offer a bridge between the 2D and 3D worlds, with the availability of bulk intercalation chemistry when stacked as 3D particles, and exciting physics when isolated as 2D sheets. Graphite has long been known for its intercalation chemistry,[43] and graphene has captivated the world, with phenomena such as ballistic conductivity, high carrier concentrations, excellent electrical and thermal conductivity, and high strength.[44]

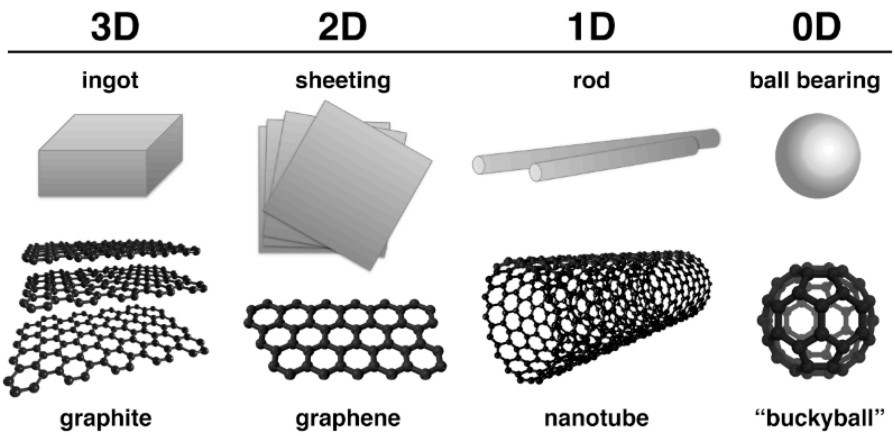

Figure 2.3: Dimensionality in materials. Macroscale objects (top) and carbon-based nanomaterials (bottom) as examples of three-, two-, one-, and zero-dimensional objects.

2.2 From MAX to MXene

Two-dimensional materials such as graphene or TMDs can be made one of two ways: *bottom-up*, in which source materials are reacted to immediately synthesize the desired material (such as vapor deposition methods of MoS_2),[45] or *top-down*, in which a precursor must first be obtained or made, and subsequently treated to yield the desired material (such as chemical exfoliation of bulk MoS_2).[46] MXene, the two-dimensional material that is the subject of this work, is thus far only able to be produced in a *top-down* fashion, starting from the 3D nanolaminate material MAX phase. Because MAX phase is not naturally occurring, this adds an extra step to MXene production.

2.2.1 Discovery and development

In the 1960s, an interesting class of materials dubbed H-phases were discovered by Nowotny *et al*.[47] These were further developed by Barsoum *et al*. and named the MAX phases,[48] with structure $M_{n+1}AX_n$, where M is a transition metal, A

is an element from groups 11-16 such as Al, Ga, Ge, Sn, *etc.*, and X is C or N. Mixtures of elements on all sites M, A, and X are possible. The structure is comprised of metal MX layers sandwiched with layers of A elements; the MX layers can be of varying thickness as described by *n*, which ranges from 1 to 3; symmetry is described by the hexagonal space group $P6_3/mmc$, thus the MX layers are twinned along the *c* direction. Notable structural variations in the MAX phases (shown in Fig. 2.4) include:

1. Modification of the A-layers, with solid solutions,[48] or a doubling of the layer (*e.g.* in the case of Mo_2Ga_2C as opposed to Mo_2GaC).[49,50]
2. Modification of the MX layers, either through solid solutions,[48] or ordered distribution of different transition metals within the MX layers (either in a core/surface layer type arrangement,[51] or in-plane ordering, so-called 'i-MAX').[52]
3. Changing of *n*, leading to different thickness of the MX blocks (such as Ti_2AlC *vs.* Ti_3AlC_2).

A huge variety of MAX phases has been synthesized. These are summarized graphically in Fig. 2.5 to highlight the variety of metals, A elements, and structural types that have been reported to date. While synthesis is typically performed with bulk ceramic processing techniques, select compositions have also been made in thin film form by deposition methods.[53]

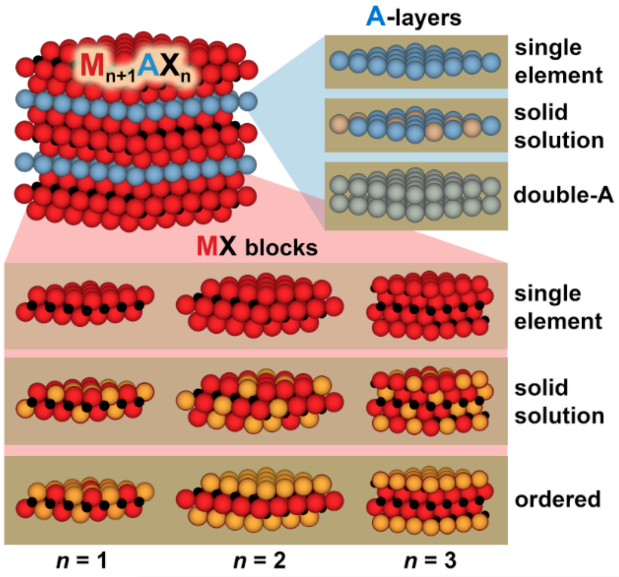

Figure 2.4: Compositional and structural variability in MAX phases, highlighting changes to the A layers and MX blocks. Ordered compositions comprise in-plane ordering 'i-MAX' for n = 1 and segregated layer out-of-plane ordering for n = 2,3. Blue spheres represent A-group elements (Groups 11-16) and red and yellow spheres represent various transition metals. Black spheres represent carbon or nitrogen, which can also form solid solutions on the X sites.

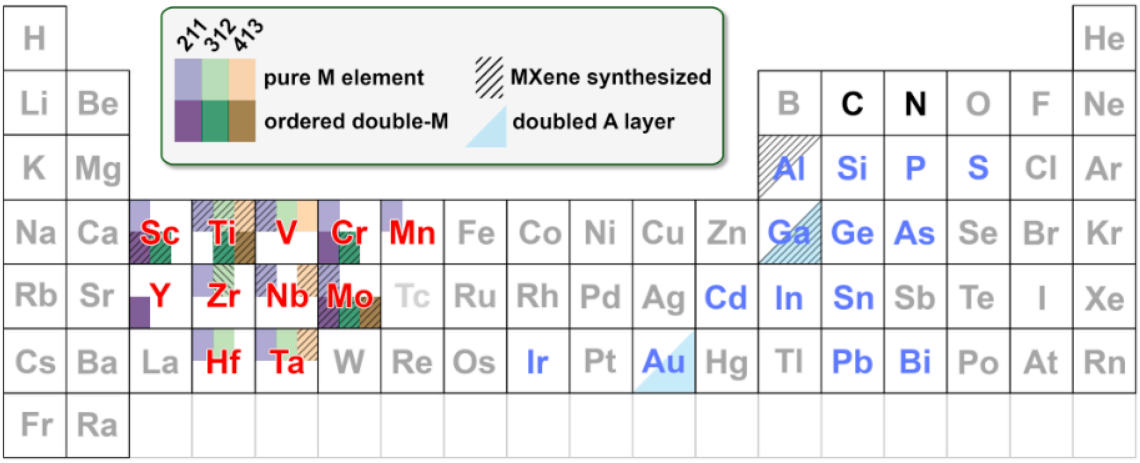

Figure 2.5: MAX phase compositions synthesized to date. Colored symbols represent MAX phases successfully synthesized containing various M elements (red), A elements (blue), and X elements (black). See the key for added colors (on the M elements) to distinguish 211/312/413 phases, phases with pure M element, ordered phases with multiple M; or on the A elements to distinguish special doubled A-layer phases, and those from which MXene has successfully been produced. Zr_3C_2 MXene is an exception, since it was made from the phase $Zr_3Al_3C_5$.[54] Solid solutions (non-ordered) have not been listed here; however, many such compositions have been made. Note that this graphic is not comprehensive.

While the MAX phases are interesting in their own right due to their combinations of high temperature stability, thermal and electronic conductivity, and machinability,[48] because of the weak metallic bonding of the A-layers relative to the covalent bonding of the MX layers, acids or bases that react with the A elements should be able to etch them and release the MX sheets as 2D materials. Removing the A layers was, however, difficult in practice (especially without collateral damage to the MX layers), but was achieved in 2011 by Naguib *et al*. with the use of concentrated hydrofluoric acid.[2] The new material was dubbed MXene because of its derivation from the MAX phases, the removal of the A element, and its similarity to graphene as another conductive 2D material. M and A elements contained in the MAX phases that have been successfully etched to date are marked with shading in Fig. 2.5. The structural variability alone of MAX phases demonstrated in this figure gives great excitement for the tailorability of structure and composition, and therefore properties, of the resulting MXenes.

2.2.2 MXene structure

MXene's basic structure remains relatively unchanged from the parent MAX phase, as removal of the A layer is accomplished with the MX layers still in place. Initially, the resulting exfoliated particles resembled accordions, where it was clear that the A-layers had been removed, leaving stacks of MX sheets called multilayer (ML) particles. An example of this morphology is shown in Fig. 2.6b. This was in stark contrast to the general appearance of MAX phase particles (Fig. 2.6a).

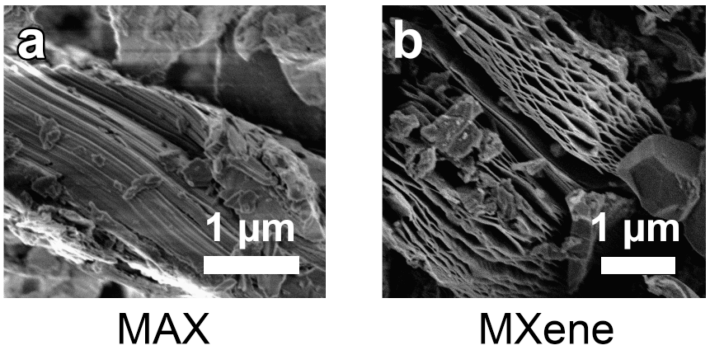

Figure 2.6: SEM images of a) MAX (in this case Nb_4AlC_3) and b) MXene (in this case Nb_2CT_x) produced using HF, highlighting the resulting accordion-like structure. While these are different compositions, the same morphology phenomena are general.

An overview of structures discussed here is shown in Fig. 2.7. A simple view is that the structure, after etching, retains the parent MAX phase symmetry of $P6_3/mmc$ (Fig. 2.7a–c); however, as will be discussed later, from a crystallographic point of view this can change with any movement of the nanosheets relative to one another, but the MX layers (nanosheets) are still twinned alternately in the stacked arrangement (Fig. 2.7d). This leads to a choice of assuming symmetry retained as $P6_3/mmc$ for the material as a whole, with disregard for disturbances in the lateral relation of the nanosheets (and random distribution of surface terminations, which will be discussed in the next section), or of assigning symmetry as that of individual nanosheets that are stacked together. This begs the practical question of how to index diffraction patterns. The highest-intensity basal reflection can be indexed as either (002) for the $P6_3/mmc$ case, or called simply 'basal spacing' for the case that the nanosheets are not stacked orderly. Regardless, this reflection, one of the most important for the study of MXenes thus far, describes the same value. The $a = b$ parameters essentially remain unchanged regardless of how the nanosheets are stacked. Publications have used both conventions, so they are referenced

interchangeably in this work. On a final note, the composition and structure within the nanosheets is retained from the parent MAX phase during the etching process; thus if a MXene is desired with *e.g.* double ordered transition metals, the corresponding MAX phase is selected for etching.[4] A notable exception to this is cases where specific transition metals can be selectively etched out along with the A elements; this is the case for $(Mo_{2/3}Sc_{1/3})_2AlC$, which gives rise to $(Mo_{2/3}\square_{1/3})_2CT_x$, also designated $Mo_{1.33}CT_x$, containing in-plane ordered divacancies (□) resulting from the preferential etching of the ordered Sc atoms from the MAX phase.[55]

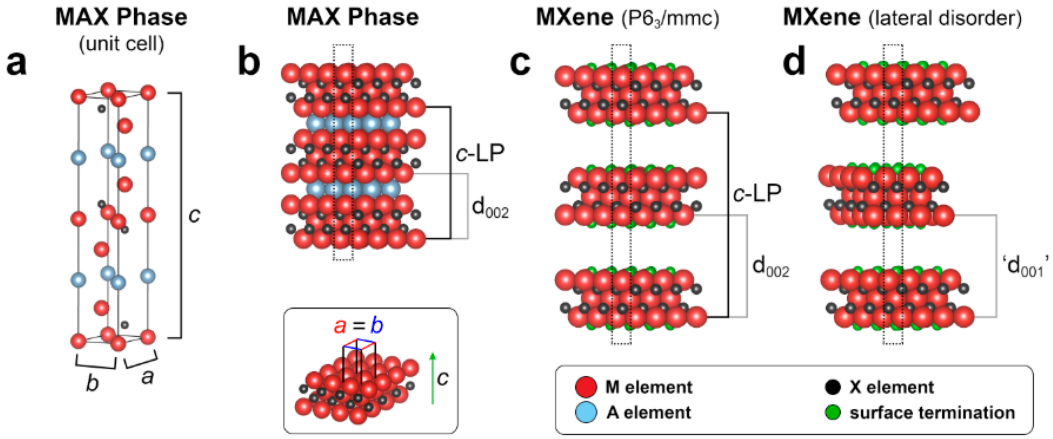

Figure 2.7: Structural overview of MAX and MXene. a) MAX phase ($P6_3/mmc$ symmetry), showing $a = b$ and c lattice parameters (LP) of the unit cell and, b) expanded structure to show sheet arrangement. c) MXene structure retaining $P6_3/mmc$ symmetry. Note that c-LP is twice d_{002}. d) MXene structure maintaining the same basal spacing of (c), but with lateral or rotational (turbostratic) disorder of the sheets, so that the $P6_3/mmc$ symmetry is broken and the structure is better described by a basal spacing 'd_{001}'. Each MXene nanosheet in the structure still retains its $a = b$ parameters.

Because the etching process is performed in a solvent, the exposure of the basal planes of the MX layers results in reactions to form surface terminations. The makeup and organization of these surface terminations has been elucidated through

much work. They can include moieties such as –O, –OH, –F, –Cl, –OH•H_2O (Fig. 2.8),[56,57] and others (including groups from theoretical studies such as –OCH_3 or –N),[58] are more or less randomly distributed spacially,[59] and can be mobile, with the possibility of decomposition reactions that enable, for example, –OH groups to leave as H_2O,[60] with chemistry similar to the surface reactions of titania (this work also brought to light that perhaps a larger area of the surface T sites than previously thought was left unoccupied). Later work has attempted to elucidate the origins and stability of surface terminations.[61]

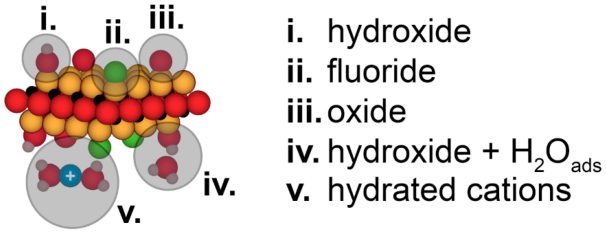

Figure 2.8: Types of MXene surface terminations based on work from XPS, NMR, and other characterization tools. Hydrated cations are not a surface termination but are present in the vicinity and have been suggested to interact with deprotonated –OH surface groups (i.).[62]

Early work with base-forming salts (*e.g.* hydroxides and acetates) showed that cations could be inserted into the MXene interlayers by immersing the material in aqueous salt solutions, with resulting structural changes; variation of the anion size while maintaining the same structural changes showed that only the cations are intercalated as opposed to their anion counterparts.[9]

Unlike well-studied materials like clays, there was, at time of writing, little consensus on exactly where the counter-balancing negative charge (the counterpart to the cation) resides in the MXene. Zeta potential analyses suggested that the separated

nanosheets in suspension held a negative charge,[63] and more recent work with Raman spectroscopy gives evidence[64] to earlier ideas that the negative charge in MXene may reside in deprotonated hydroxyl groups.[62] Another possibility was that the negative charge resides in bands of the metal carbide layers, as was discussed previously for MoS_2, or for electrochemical ion intercalation of $Ti_3C_2T_x$.[65]

2.2.3 MXene synthesis and processing techniques

As stated previously, the first reported etching of MAX to MXene was done with concentrated hydrofluoric acid.[2] This is obviously not the friendliest of reagents, so early on, efforts were made to find alternatives. Bifluoride salts (in this case NH_4HF_2) were used with some success;[53] however at the time, HF remained the dominant reagent. Regardless of etchant, the general technique is a wet chemical etching to remove the A layers. This also works on MAX phase that has been produced epitaxially by deposition methods.[53] After the etching step, the byproducts and excess acid must be removed. This is accomplished with a washing process, which is typically stepwise and comprises cycles of adding distilled water, agitation, centrifugation, and decanting of the waste supernatant, until a neutral pH is reached. An overall simplified reaction scheme, to use Ti_3AlC_2 as the most common example, could be

$$Ti_3AlC_2 + aHF + bH_2O = Ti_3C_2T_x + AlF_3 + cH_2$$

where the resulting $Ti_3C_2T_x$ is functionalized by some combination of HF and H_2O to yield O- and F-containing surface terminations *T*, as well as the byproducts AlF_3 and hydrogen, H_2, gas.[66]

This process has been explored briefly in terms of kinetics.[67] It was found, understandably, that etching rates increased with increases in time and temperature. Neutron / x-ray diffraction pair distribution function (PDF) analyses showed that the concentration of the HF etchant could have profound effects on the resulting structure, especially with regard to surface structure and hydrogen bonding.[68] The etching process, while generally applicable across MAX phase compositions, behaves very differently between different MAX chemistries. This is evident theoretically,[69] as well as experimentally – for example, Ti_2AlC (n = 1) is more reactive toward HF than Ti_3AlC_2 (n = 2), a trend which seems to carry through other MAX phases.[70] As to the stability of MXene, it was discovered early on, and further studied later, that nearly all MXenes are sensitive to oxidation, especially by reaction with dissolved oxygen in water,[71] and to a much lesser degree atmospheric oxygen;[56] Ti_2CT_x is much more prone to oxidation than $Ti_3C_2T_x$,[72] and this is likely a trend in other MXenes as well. As a result, care should be taken when storing MXenes to avoid exposure to oxidizing agents. That said, the vulnerability can be exploited to easily partially oxidize the MXene to yield MXene/oxide nanocomposites.[73,74,75]

One of the struggles of experimental studies of MXene is that despite many interesting structures predicted theoretically (such as Sc_2C),[76] it can still be a difficult business to actually produce the desired compositions synthetically; some MAX phase compositions tend to either be too slow to etch (*e.g.* Mo_2GaC, Ti_3SiC_2) or do not etch selectively, with the MX blocks being consumed completely along with the A layers (*e.g.* Cr_2AlC). In some cases, workarounds can be applied to compositions that refuse, or have too long of a reaction time, to be readily etched. As an example,

the A layer in Mo_2GaC proved very difficult to remove, but the transformation of Mo_2GaC into the new phase Mo_2Ga_2C (a very unusual MAX phase with doubled A layers but retention of the metal carbide layer structure) allowed for etching into the MXene Mo_2CT_x.[77] Another example is the production of $Zr_3C_2T_x$ by starting with the MAX-like material $Zr_3Al_3C_5$ (which is actually comprised of layers of Zr_3C_2 sandwiching 'A-layers' of Al_3C_3), and etching the Al_3C_3 layers with hydrofluoric acid.[54] The resulting MXene is structurally equivalent to those derived from MAX phases, despite the different starting material.

Like many other weakly-bonded layered materials, MXene layers can be readily separated from one another. In a departure from graphene, which is hydrophobic and must be processed with surfactant or as graphene oxide in aqueous solutions, MXene is inherently hydrophilic and makes stable colloidal suspensions of nanosheets in water. In the early stages of MXene research, going from stacked *viz*. multilayered (ML) particles to suspensions of individual nanosheets involved intercalation of dimethylsulfoxide (DMSO), which increased the interlayer spacing, drew in H_2O, and further weakened the bonding of the layers;[78] this was followed by ultrasonication to physically separate the layers. This process was time-consuming and also used additional reagents, but was successful in producing high-concentration suspensions of MXene nanosheets. Later work showed that reaction of ML MXene with tetrabutylammonium hydroxide (TBAOH) could be a powerful method for producing high-concentration suspensions of nanosheets, and was useful across a variety of MXene compositions.[63] Suspensions of MXene can be described simply in terms of mass concentration (e.g. mass of MXene per volume of suspension, typically

mg/mL), but because the flakes are not of uniform dimensions, they can also be described in terms of distributions of flake lateral sizes or layer number (in the case that delamination was incomplete or that there are populations of nanosheets that have begun to restack).[79] The distributions of nanosheet size and stacking number can be controlled by centrifugation conditions.[71]

The first nanosheet processing method to be explored was filtration.[78] This involves suction filtration of a suspension of MXene nanosheets in water over a filter, typically nitrocellulose or a porous polypropylene material like CelGard polypropylene membrane. As the solvent is removed, the nanosheets re-stack flat to form a turbostratically disordered film, which can be detached and is free-standing. This process is the basis for production of MXene composite films as well, from polymers (such as polydiallyldimethylammonium (PDDA) chloride),[80] to carbon nanotubes,[81] to metal oxides.[82] The production of composites using MXene nanosheets has developed into an important branch of research; applications will be discussed later. Filtration is also an important method in determining the mass concentration of suspended MXene; this can be determined by filtering a known volume of suspension to form a film and weighing the film once dried.

Nanosheet suspensions can also be made into thin films by various processes. Spin-coating involves placing a concentrated suspension on a substrate, followed by spinning at controlled rotational speeds to distribute the nanosheets evenly across the substrate, and has been shown to produce high quality thin films for optical studies (this was shown for both $Ti_3C_2T_x$ and Ti_2CT_x).[8,83] Films were also produced *via* spray-coating, which at the most rudimentary level involved loading MXene

suspension into an airbrush and painting it onto a substrate. These large-area spray-coated films showed stable conductivity under bending conditions up to a radius of 5 mm, and further showed transmittance that was tunable *via* electrochemical intercalation of ions.[84] Nanosheet suspensions have also been mixed with the polymers poly(acrylic acid) (PAA), polyethylene oxide (PEO), poly(vinyl alcohol) (PVA), and alginate/PEO, and electrospun to produce fibers containing MXene; the additions of small amounts of MXene (1 wt %) allowed the crystallinity of the polymers to be tuned.[85] Finally, it has been shown that electrophoretic deposition (EPD) is a very scalable and rapid method for high-throughput production, and can produce MXene films with conductivity and capacitance on par with those produced by other less-scalable methods.[86] This process, as well as the others described previously, all require MXene suspension. Understanding, controlling, and optimizing aspects of the process of creating MXene suspensions is thus very important because they are such crucial starting points for many further processing techniques.

Since the start of this project, many more synthetic techniques have been developed for MXene that are not covered in the body of this work, so they are worth mentioning here. One method, which was explored quite early on but was determined to only produce fluorinated/oxygenated binary carbides rather than MXene, is etching with molten fluoride salts.[87] This process obviously requires that the reaction be carried out at least at the melting temperature of the salt. The initial report using LiF (melting point of 845 ºC) was likely at too high a temperature, as it is now known that MXene (if any was formed) may decompose at around 800 ºC.[88] Success was later

achieved using a eutectic mixture of LiF, NaF, and KF (heated to 550 ºC), to produce the first purely nitrogen-based MXene, $Ti_4N_3T_x$.[89]

It was assumed that the A layer of MAX phases could also be removed electrochemically. This was explored in a few publications. It was found to be possible, but the process may be limited by degradation of the metal carbide layers competing with etching of the A layers.[90,91] However, it was also found recently that the process can be completed without the use of F-containing reagents, which offers possibilities for increased safety and surface termination control.[92] Finally, we note that there are additional F-containing systems that can accomplish etching in addition to hydrofluoric acid - *e.g.* FeF_3/HCl.[93] Reactions with bases have been proposed to etch the MAX phase without constant reaction with HF, but these still found an HF pre-treatment to be necessary.[94]

2.2.4 Ions in MXene

To explore the effects of intercalated ions, especially with MXene beginning to be targeted at the time for electrochemical energy storage applications, early attempts were made to introduce ions into the interlayer space; this was accomplished to a high degree only with salts that formed basic solutions, e.g. hydroxides.[9] The MXene sheets can be susceptible to attack from hydroxides,[72] so at the time of the initiation of this project, a non-destructive method of reliably intercalating cations was desired. Further, while the intercalation of cations was known to have some structural changes, the control of cation composition and understanding of its effects on structure was not fully developed. Investigations were limited to brief XRD study (with more emphasis on structural change during electrochemical intercalation),[9] and

changes on scales well beyond that of the unit cell.[95,96] The presence of ions combined with the high electrical conductivity of MXene led to their being dubbed 'conductive clays'.[97] However, this was not substantiated methodically at the time.

As noted earlier, initial work with salts of various sized anions established that only the positively-charged cations intercalated into the MXene, when structural changes were seen to be independent of anion size. Ions could also be intercalated electrochemically. This was demonstrated in applications by early reports of electrodes for lithium-ion batteries or electrochemical capacitors using $Ti_3C_2T_x$ as active material.[9] Ions were also electrochemically inserted so that the resulting structure of the interlayer could be characterized with TEM, leading to the observation, in some cases, of cation bilayers.[98] Further, electrochemical quartz crystal microbalance (EQCM) measurements were used to better understand the migration of ions in MXene through electrochemical intercalation.[95] In all cases, the intercalation of cations was performed *after* the etching reaction to produce MXene. In the time since the start of this project, more advanced techniques have been applied towards the study of ions and water confined in the MXene interlayer.[99,100,101]

After removal of the A element, MXene remains comprised of nanosheets that are stacked in a relatively weakly-bonded ML structure. Early applications involving MXene-based electrodes contained such ML particles, typically mixed with poly(vinylidene fluoride) (PVDF) as a stabilizing binder, and carbon black as a conductive additive due to the insulating nature of the binder. This required a somewhat lengthy process and use of additional reagents.[102]

On a final note, computational studies have been very helpful in adding to understanding of interlayer ion behavior, such as adding to understanding of how the interlayer separation should be expected to respond to various ions, as well as the effect of surface terminations on selectivity.[103] These are further discussed in the next chapter.

2.3 Applications

There already exist good reviews on the applications of MXenes, so they will only be covered briefly here. MXene can be utilized in a variety of morphologies, from single isolated nanosheets and thin films, to pristine stacks of undisturbed nanosheets (multilayer MXene), to restacked films (generally on the macroscale and produced by filtration, referred to here as 'filtered films').

Energy storage

Intercalation-based electrochemical energy storage applications were some of the first studied, and have continued to be popular, for MXene.[104,105] The material has shown great promise in electrodes for batteries, ranging from lithium-ion,[106] to lithium-sulfur,[107] to other alkali and alkaline-earth ion such as Na^+, Mg^{2+}, *etc*.,[108,109] as well as outstanding performance in electrochemical capacitors, using both aqueous and organic electrolytes, and a large variety of ions.[81,110] New production methods (after the start of this work), without the use of additives, allowed MXene to perform with extremely high volumetric capacitance, with only moderate capacitance loss when electrode thickness was increased, approaching technical thicknesses.[79] The capacitance values have been on the increase since the initial reports. Other methods

of increasing capacitance have been to use additives to the MXene, such as carbon nanotubes or alkylammonium cations followed by Sn^{4+} intercalation,[110,111] to act as pillars to the interlayer space in an attempt to increase electrolyte access. MXene is particularly interesting in that it can support extremely high cycling rates (up to 10 V s^{-1}) as an electrochemical capacitor electrode – this high-power application is not seen in other pseudocapacitive materials.[112]

Some materials offer the possibility of high capacitance but limited electrical conductivity, and so have become attractive for combination with MXene to increase the overall capacitance. Electrodes have been made combining MXene with metal oxides.[82] Another approach is to intentionally partially oxidize MXenes (for use in batteries), which develops composite structures combining the benefit of the two materials in the same structure, with the MXene making up a conductive core.[74,73] The total number of MXenes produced so far outnumbers those that have been well-studied in energy storage applications, so it is clear that the material holds much more potential than has been investigated to date, especially given suggestions predicted by theoretical work.[108,113,114]

Environmental and sensing applications

Like other layered materials, MXene has been demonstrated in applications involving ion exchange and sequestration. It has proven or been predicted to be useful in the removal of lead,[62] chromium,[115] mercury,[116] and uranium species,[117] as well as larger ions like phosphates.[118] The MXene has also proven useful as a starting material to form specific TiO_2-based structures that excel at metal sequestration.[119] In

the form of filtered films, it has demonstrated selective filtering of ions based on charge and size,[120] and capacitive deionization has also been shown.[121]

MXene has also proven useful as a sensor material. Using hemoglobin immobilized in the structure, nitrite and H_2O_2 could be electrochemically detected;[122,123] glucose is detected by Au/MXene composites;[124] Cd(II), Pb(II), Cu(II), and Hg(II) could be detected electrochemically;[125] and MXene has proven useful for the detection of gases, such as ammonia and CO_2, as well as acetone, methanol, and ethanol.[126,127,128] Based on their well-studied interaction with H_2O, they can also been employed as humidity sensors.[100]

Electronics

MXene has inherently high electrical conductivity, a property it shares with the parent MAX phase. This property has allowed it to have such a wide application in electrodes for energy storage, but also lends it to many other applications where high conductivity can compliment 2D properties. Its high conductivity has enabled it to be explored for applications such as thin-film optoelectronics (especially due to its high conductivity at thicknesses low enough to remain transparent),[84,8] piezoelectric sensors,[129] triboelectrics,[130] and electromagnetic interference shielding.[131,132] For the latter, MXenes' high electrical conductivity, internal reflections, and ease of processing into films make them ideal candidates for these applications.

MXene, being useful for energy storage, has also been used in state-of-the-art wearable electronics. It has proven a promising material for making fiber-based supercapacitors that can be woven into fabrics.[133,134]

Other applications

MXene has found use in a host of other applications – it has been explored for antimicrobial properties,[135] in methods for anticancer tumor targeting,[136,137] and as a probe for neural activity.[138] Many of these methods also demonstrate MXene's readiness for composite materials; for example, when utilized as a tumor targeting agent, it was used as a substrate to grow manganese oxide sheets.[136]

All in all, MXene has already found a plethora of applications in which it plays an exceptional role; many of these are based on the intercalation of ions, and the success and promise of MXene in these roles more than justifies deeper study into structure and interactions of ions with this material.

CHAPTER 3 - MATERIALS AND METHODS

This chapter covers procedures and details for the syntheses and experiments carried out in this work, as well as providing some details on select characterization techniques.

3.1 - Materials

Table 3.1 gives details on materials and reagents that are referenced in the following sections. The details listed apply to chemicals appearing in those sections unless noted otherwise.

Table 3.1: Details of chemicals used in this work

Chemical	*Abbrev.*	*Supplier*	*Particle Size (mesh)*[a]
Hydrobromic acid, conc.	HBr	Acros	--
Hydrochloric acid, conc.	HCl	Fisher	--
Hydrofluoric acid, conc.	HF	Acros	--
Sulfuric acid, conc.	H_2SO_4	Fisher	--
Cobalt (II) chloride	$CoCl_2$	Alfa Aesar	--
Iron (II) chloride	$FeCl_2$	Alfa Aesar	--
Lithium bromide	LiBr	Alfa Aesar	--
Lithium chloride	LiCl	Alfa Aesar	--
Lithium fluoride	LiF	Alfa Aesar	--
Lithium iodide	LiI	Alfa Aesar	--
Manganese (II) chloride	$MnCl_2$	Alfa Aesar	--
Nickel (II) chloride	$NiCl_2$	Alfa Aesar	--
Potassium chloride	KCl	Alfa Aesar	--
Phosphorus pentoxide	P_2O_5	Acros	--
Potassium fluoride	KF	Alfa Aesar	--
Rubidium chloride	RbCl	Alfa Aesar	--
Sodium chloride	NaCl	Alfa Aesar	--
Sodium fluoride	NaF	Alfa Aesar	--
Titanium carbide	TiC	Alfa Aesar	-325
Aluminum	Al	Alfa Aesar	-325
Argon	Ar	Airgas	--
Graphite	C	Alfa Aesar	-300
Titanium	Ti	Alfa Aesar	-325

[a]Particle size included only when relevant, i.e. ceramic sintering processes

3.2 - Synthetic methods

This first section deals with methods for synthesis of MAX phases and their etching to the corresponding MXenes that were developed and used in this work.

3.2.1 - MAX phase synthesis

The methods reported in this section, for MAX phases, are not novel, but are included for completeness. As a general procedure, a MAX phase is produced by reaction of powders of reactants in 20-40 g batches. Powders are added to a polypropylene container with zirconia milling balls and kept on a ball mill for 16-18 h. The mixed powders are then placed into a trough-shaped alumina crucible and into an alumina tube furnace, which is closed to the atmosphere and has a continuous flow of Ar gas (sometimes the powders are pre-compacted). The mixture is heated (pressureless sintering) to a specified soak temperature at a controlled heating rate, and is held for a specified time; it is then allowed to cool to ambient temperature and removed from the furnace.

The resulting weakly sintered brick is then milled into powders with a TiN-coated milling bit and sieved to -400 mesh (<38 μm particle size). This general procedure is applied with various reactants and conditions to synthesize the majority of the MAX phases used in this study, and summarized in Table 3.2. Ti_2AlC is available commercially as a powder from Sandvik AB (Hallstahammar, Sweden); however, it typically contains Ti_3AlC_2 as an impurity. The powder can still be used as a Ti_2AlC precursor to make phase-pure Ti_3AlC_2, but the impurity amount must be first accurately analyzed to determine the right amount of TiC to add.

Hot pressed samples: Nb_4AlC_3 was produced by mixing the powders as before, with the difference that the resulting mixture was compacted in a BN-sprayed graphite die at 3 MPa, followed by sintering in a flowing Ar atmosphere at a load corresponding to a stress of 30 MPa. See the included reference in Table 3.2 for more detail. This work was done by Dr. Chunfeng Hu.

Table 3.2: Synthetic parameters of MAX Phases used in this study

	reactants (molar ratios)	*mixing time (h)*	*heating rate (°C min^{-1})*	*soak temp. (°C)*	*soak time (h)*	*Ref*
211 phases						
Ti_2AlC	2 Ti : 1.1 Al : 1 C	18 [b]	5–10 [b]	1400	1	[83]
Nb_2AlC	2 Nb : 1.1 Al : 1 C	18 [b]	5–10 [b]	1600	4	[106]
312 phases						
Ti_3AlC_2	1 Ti_2AlC [c] : 1 TiC	18	5	1350	2	[79]
413 phases						
Nb_4AlC_3 [a]	4 Nb : 1.1 Al : 2.7 C	24	20	1700	1	[139]

[a] See notes for *hot pressed samples*
[b] These values are from our laboratory protocols and/or were not included in the methods of the reference
[c] This may be obtained from commercial sources, but care must be taken to account for Ti_3AlC_2 impurity amounts

3.2.2 - MXene production (general)

At the start of this project, etching MAX phase to produce MXene was mostly limited to HF, typically fully concentrated at 49-50 wt.% or 30 M. Unless otherwise noted, whenever an acid concentration in this chapter is described as a percent, a weight/weight percent is implied. This project introduced systematic study of methods for *in-situ* generation of HF, and eventually moved back to HF in conjunction with salts to study the effects of ions. An overall summary of etching methods explored in this section is shown in Table 3.3. Therefore the methods are

split into two parts (in addition to 'standard' etching with HF alone): etchings with mineral acids and fluoride salts, and etchings with HF and various halide salts.

Table 3.3: Summary of etching schemes attempted (dark squares) for $Ti_3C_2T_x$

Mineral acids	*Salts added to mineral acid*							
	LiF	CsF	CaF_2	LiCl	LiBr	LiI	NaCl	TMACl[a]
HF	■			■	■	■	■	■
HCl	■	■	■					
HBr	■							
H_2SO_4	■							

[a]TMACl = tetramethylammonium chloride

Mineral acids with fluoride salts

$Ti_3C_2T_x$. These etching reactions were set up with the parameters of acid concentration, volume of etchant relative to MXene mass, molar equivalents of salt relative to moles of MAX, etching time, and nominal etching temperature (controlled by immersion of the high-density polyethylene etching vessel in a temperature-controlled oil bath). After completion of the reaction, the mixture was transferred to centrifuge tubes (with roughly 0.5 g of mixture in each tube), and distilled water was added. Each tube was shaken vigorously for ~ 2 min, after which it was centrifuged at 3500 rpm / 2300 xG for 2 min to settle the powders. The clear supernatant (Some color in this waste solution on the first wash corresponds to dissolved transition metal complexes, probably of halides) was decanted, and replaced with fresh distilled water. This cycle was repeated until the pH reached neutral. Coinciding with this, the MXene had a tendency to spontaneously delaminate, causing the supernatant to have

a color and become darker. After this, the sediment was collected by suction filtration. Various parameters for this general scheme are shown in Table 3.4.

Ti_2CT_x. The same basic procedure was followed as for $Ti_3C_2T_x$, with an etchant of HCl (6 M; 10 mL per 1 g Ti_2AlC) mixed with LiF (5 molar equivalents), a reaction time of 24 h, and a temperature of 35 ºC. The washing procedures were the same. One important difference was that during addition of the MAX phase to the etchant solution, the solution was cooled in an ice bath due to the much higher reactivity of Ti_2AlC.

Table 3.4: Summary of $Ti_3C_2T_x$ etching conditions for mineral acid + fluoride salt etchings

entry	*acid*	*acid conc. (mol L^{-1})*	*salt*	*molar equiv. salt*	*Time (h)*	*temp. (ºC)*
1	HF	5.8	LiF	5	24	25
2	HCl	6	LiF	0.5	45	35
3				1	45	35
4				1.2	45	35
5				2	45	35
6				3	45	35
7				5	45	35
8	HCl	9	LiF	7.5	24	35
9	HCl	6	CsF	5	24	35
10	HCl	6	CaF_2	2.5	24	35
11	HBr		LiF	5	24	35
12	H_2SO_4	2.5	LiF	5	24	35

Hydrofluoric acid alone

$Ti_3C_2T_x$. Etchings with HF in this work were limited to 10 % HF (or 5.8 M, a roughly 1/5 dilution from concentrated stock HF). These were used as control samples against ion-intercalated MXenes. For each reaction, 10 mL of 10 % HF was prepared in a 60 mL high density polyethylene bottle, and 1 g of Ti_3AlC_2 was slowly

added over the course of ~ 5 min to avoid overheating by the exothermic reaction. The reaction was allowed to stir for a given time, after which the mixture was washed in cycles as with the acid/salt etchings, but with only distilled water; this was repeated until a neutral pH was reached, and the sediment was collected by suction filtration.

Hydrofluoric acid with halide salts

$Ti_3C_2T_x$. As with mineral acid and fluoride salt reactions, these were set up with the same parameters of acid concentration, volume of etchant relative to MXene mass, molar equivalents of salt relative to moles of MAX phase, etching time, and nominal etching temperature (controlled by immersion of the etching vessel in a temperature-controlled oil bath). After completion of the etching, the sediment was washed similarly to the mineral acid/fluoride salt etchings. Directly after etching, centrifuge tubes were loaded with roughly 0.5 g of MXene. HCl was then used (6 M; 40 mL) for two pre-washing cycles in order to remove any salt impurities. If ion-exchange was desired, additional steps outlined in section 3.2.3 were taken at this stage. Otherwise, after the HCl pre-wash, 40 mL of 1 M LiCl solution was used for one wash cycle. Re-washing with the salt is necessary to ensure that any H_3O^+ from the acid that may have ion-exchanged were replaced with the desired cation Li^+. The sediment was then washed with distilled water to a neutral pH. All reactions were carried out with 10 % HF (5.8 M), for 24 h, at 25 ºC. The salt added to the etchant was LiCl, LiBr, LiI, NaCl, or tetramethylammonium chloride (TMACl) all in 5 molar equivalents per mole of $Ti_3C_2T_x$; for LiCl, additionally 1, 3, 7, 9, and 20 equivalents were explored.

Ti_2CT_x. The etching procedure was followed as outlined for $Ti_3C_2T_x$, with the modification that the MAX phase was added after the etchant had been cooled in an ice bath. Washing protocols were the same as for $Ti_3C_2T_x$.

Nb_2CT_x. The procedures for $Ti_3C_2T_x$ were slightly modified. The overall scheme of etching and washing remained the same, but due to lower reactivity of the MAX phase, the HF concentration was increased to 50 %, the etching temperature was increased to 50 ºC. The Nb_2AlC:LiCl molar ratio was kept at 1:5.

3.2.3 - MXene processing (general)

MXene 'clay'

$Ti_3C_2T_x$, when etched with LiF+HCl, readily absorbed distilled water to become a clay-like spreadable paste. The paste could be shaped and dried, or sandwiched between two sheets of polypropylene CelGard and rolled with a rolling mill to shear the material into a film (under certain conditions: entries **7** and **8** in Table 3.4). The rolled films were allowed roughly 1.5 h of drying time before the CelGard membrane was peeled off. The spacing of the rollers was modulated to control the thickness of the resulting film.

Delamination

The best results for creating stable, concentrated MXene suspensions came from adding freshly-made MXene (immediately after the washing steps, before drying) to distilled water pre-purged with Ar (bath-sonicated for 10 minutes while Ar was bubbled through), followed by 1 h of sonication with continual Ar flow. After this, the suspension was centrifuged to ensure that it contained predominately single

nanosheets. Conditions for this were typically centrifugation for 1 h at 3500 rpm / 2300 xG. For films made for WAXS studies, the centrifugation conditions were 1 h at 5000 rpm / 5696 xG to ensure a majority of single, and not stacked, nanosheets.

Filtered films

MXene suspensions were placed in a multi-part glass suction filtration apparatus, with polypropylene CelGard as a filter material. A vacuum pump was used to create suction. For suspension concentration determinations, typically 10 mL of MXene suspension were measured and filtered. After the water was removed, the resulting film was dried in vacuum at least 50 ºC, for at least 12 h. The resulting film was weighed to determine the mass of MXene in the original volume of suspension.

Cold-pressed discs

MXene powders were loaded into a steel die, with diameter of 1 cm, and pressed, using a Baldwin hydraulic press, to various loads. The compacted discs were then carefully removed from the die.

Ion exchange

Exchange of cations in MXene was found to proceed best when the MXene powders, directly after production and washing, were exchanged immediately without allowing the MXene to dry. The best starting material for exchange was Li^+-intercalated MXene (in the majority of this work, using $Ti_3C_2T_x$). In general, directly after etching, centrifuge tubes were loaded with roughly 0.5 g of MXene. HCl was then used (6 M; 40 mL) for two additional washing cycles in order to remove any salt impurities, after which 40 mL of 1 N salt solution was used for one wash cycle (even

when Li^+-intercalated MXene was the desired product, re-washing with the salt is necessary to ensure that any H_3O^+ from the acid that may have ion-exchanged were replaced with the desired cations). Another 40 mL of the solution was added, and the tubes were shaken and allowed to sit for 24 h for exchange. After this, distilled water was used in at least 2 wash cycles to remove any traces of the salt.

Salt solutions of metals used were in a concentration of 1 N, corresponding to 1 M LiCl, NaCl, KCl, CsCl, and RbCl; 0.5 M $MgCl_2$, $CaCl_2$, $MnCl_2$, $FeCl_2$, $CoCl_2$, and $NiCl_2$. Salt solutions of alkylammonium (AA) cations were 0.5 M chlorides of tetramethylammonium (C_1), hexyl- (C_6), octyl- (C_8), decyl- (C_{10}), dodecyl- (C_{12}), and hexadecyltrimethylammonium (C_{16}), or the bromide of tetradecyltrimethylammonium (C_{14}). All AA salts were sourced from TCI America (Portland, OR, USA). For the AA salts, equilibration time was increased to 4 days, and the number of final washing cycles with water was increased to at least 4 due to the low solubility of the AA salts.

3.3 - Experimental details

Further details for specific experiments involving MXenes, beyond general synthetic approaches, are outlined in this section, as well as information on sample preparation, measurement conditions, and instrumentation relevant to characterizations.

3.3.1 - Powder X-ray diffractometry (XRD)

Since the discovery of MXenes, X-ray techniques have played a critical role in their characterization. The foremost of these is X-ray diffraction. Though it is an old and simple method for structural determinations, it has proven indispensible as a

high-throughput method for routine MXene structural determination, and simple laboratory-scale diffractometry offers a way to lay the groundwork for more in-depth studies later on. MXene belongs (nominally) to the hexagonal space group $P6_3/mmc$; the lattice parameters $a = b$ can be readily determined from (110) reflections, and the lattice parameter c (related to basal spacing) can be determined from (00l) series reflections. As discussed in Chapter 2, MXenes have been explored in many applications that involve ion intercalation; during intercalation processes, the a, b parameters do not change much (due to strong in-plane bonding; this is especially evident in the minimal change to these parameters even during the transformation from MAX to MXene),[2] but the c parameter can change drastically.[110] Therefore, changes to the c parameter are of the greatest interest – this is in line with the literature of intercalation in *e.g.* clay minerals and other layered materials reviewed earlier. As mentioned previously, the indexing of the reflections will depend upon the assigned symmetry of MXene – whether it is taken as retaining the $P6_3/mmc$ space group of the parent MAX Phase (where $c = 2 \times d_{002}$), or as having a lowered symmetry, where the separation is described simply as a 'basal spacing'.

The physics of diffraction are well-covered elsewhere (especially with advanced treatments in the literature of other layered materials),[140,141] but on the most basic level, reflections are described by

$$n\lambda = 2d \sin\theta \qquad \text{(Equation 3.1)}$$

The diffracting angle θ is determined by n (the order of reflection), λ (the X-ray wavelength), and d (the spacing of the diffracting planes or 'd-spacing'). Data are typically presented as diffraction intensity *vs*. twice the diffraction angle, 2θ, so the

separation of planes of interest can be extracted from the position of peaks along the 2θ axis. An exception, relevant to layered materials, is the case of interstratification, where mixtures of two or more phases with different basal spacings in the same particle are possible; this can lead to diffraction peaks at a location along 2θ corresponding to a basal spacing between the values of the spacings of the interstratified phases (also called irrational reflections since these do not represent a 'real' basal spacing) in the case that the distribution of the spacings along the *c* direction is random,[10] or a superstructure peak of the combined spacings if the ordering is regular.[142] The width of the diffraction peaks contains information about the degree of order of the structure through the Scherrer relation:

$$\tau = K \lambda (\beta \cos \theta)^{-1} \qquad \text{(Equation 3.2)}$$

which describes the crystallite size τ in relation to the width β, at half the maximum intensity, of a peak centered at θ, given diffraction at wavelength λ, and a dimensionless shape factor K. Practically, in layered materials, narrower diffraction peaks in the basal regions signify a higher uniformity of basal spacings from layer to layer or, in other words, a higher crystallinity. Peaks can become broadened by virtue of the crystallites being on the nanoscale, which is a concern for MXene stacked thinly, *i.e.* in a thin film. More generally, the diffraction condition can be described with momentum transfer q:

$$q = 4 \pi \sin \theta \lambda^{-1} = 2 \pi d^{-1} \qquad \text{(Equation 3.3)}$$

which is independent of the wavelength of the diffracting X-rays. Both q and 2θ are used throughout the literature. Most diffraction data in the MXene literature is reported in 2θ, and comes from powder diffractometers. This setup assumes a

completely random distribution of a large population of crystal orientations, leading to uniform diffraction rings; any path of the 1D detector will then give rise to peaks representing all rings (Fig. 3.1a). If a degree of preferred orientation exists, gaps in the diffraction rings can lead to missing peaks (Fig. 3.1b), or peaks of lower intensity than expected. Wide-angle x-ray scattering (WAXS) can be used to visualize the uniformity of the diffraction rings and obtain structural information that is not available readily from standard operations in powder diffractometers. This is a very low-level treatment of the topic but it is worth reinforcing for MXenes, which still rely heavily on XRD for characterization.

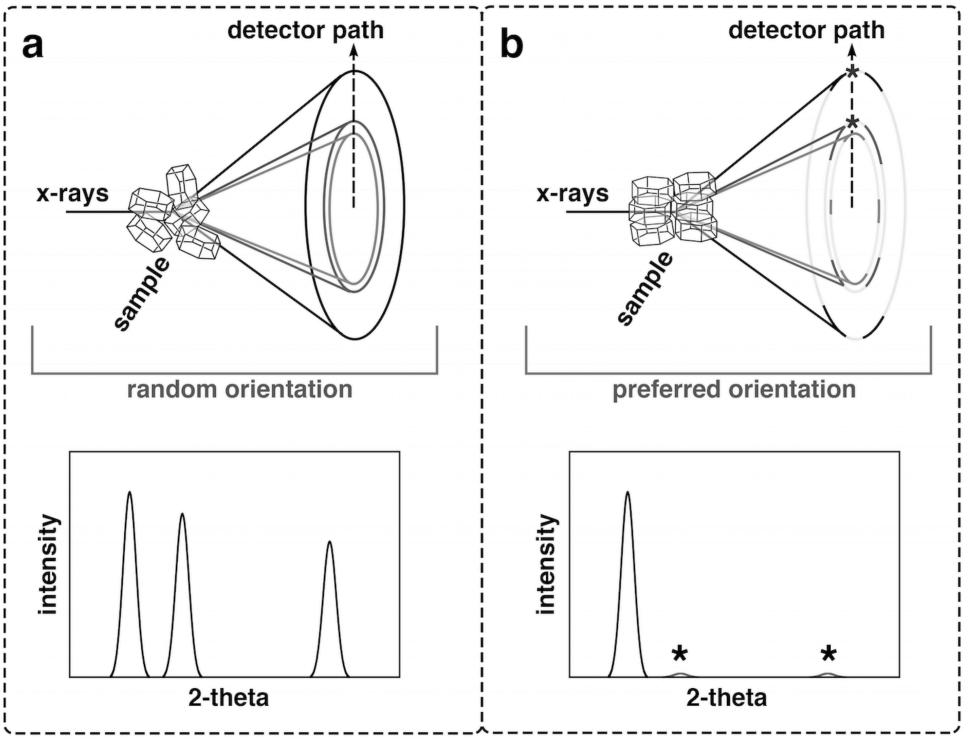

Figure 3.1: Effect of crystal orientation on powder diffractometry. a) Random orientation ensures that full diffraction rings are present and the path of the 1D detector covers all rings, leading to a diffraction pattern with a peak for every ring. b) Preferred orientation leads to gaps in the rings; if gaps are present in the path of the 1D detector (asterisks), peaks will be missing in the diffraction pattern. Changing the orientation of the sample may allow the missing parts of the rings to be observed. Note that these are not meant to represent actual data.

Sample preparation

Dry powders were simply added to a standard glass sample holder and leveled smooth with a glass slide. For measurements on fresh paste samples, before being allowed to dry, the paste was spread into a glass sample holder 0.2 mm deep with area of 4 cm^2 and scraped smooth with a glass slide. Crystalline Si was added as an internal standard for calibrating 2θ when appropriate. For samples of films, the film was typically laid flat atop a glass slide. Exceptions include films that were mounted in a custom polypropylene frame to stand vertically, or at a chosen angle.

Instrumental details

A Rigaku SmartLab diffractometer (Rigaku Corporation, Tokyo, Japan) was used to measure powder XRD patterns (Cu Kα radiation source). Samples were scanned at a step size of 0.02-0.04° and dwell time of 0.5-1.0 s per step.

3.3.2 - Humidity-controlled XRD

Because this project focuses on the structural response of MXenes to changes in environmental stimuli, *in-situ* diffraction techniques are desired, where measurements can be taken while environmental conditions are varied, such as temperature and humidity. Using humidified air (or carrier gas), the relative humidity can be varied from ~ 0 to 95 % while a given temperature is maintained (Fig. 3.2, right).

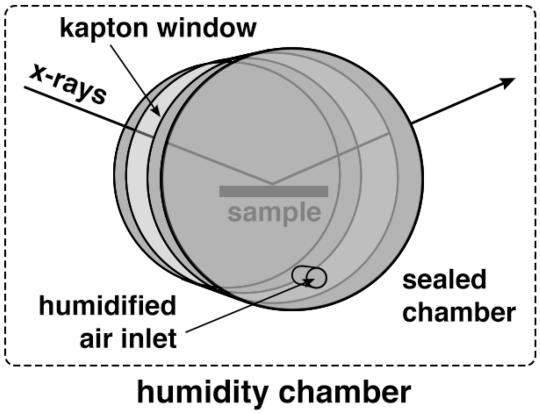

Figure 3.2: Schematic of a humidity-controlled XRD chamber. Kapton windows are mostly transparent to X-rays but maintain the chamber seal. Humidity is controlled by moving properly humidified air through ports on the chamber door.

The chamber is made with a window of Kapton, a polymer material that allows X-rays to pass through the cell while maintaining an environmental seal.[143] These techniques have been employed extensively with clay minerals to investigate structural changes (especially to study swelling phenomena).[144]

Sample preparation

$Ti_3C_2T_x$ was prepared from HF+LiCl, followed by ion exchange, as outlined in section 3.2.2, to give a series of ion-intercalated MXenes; all samples were then equilibrated for at least 2 days in ambient atmosphere (~ 55 % RH). Upon arrival at the humidity-controlled diffractometer, samples were rehydrated with distilled water to make a slurry, spread onto quartz zero-background sample plates, and allowed to dry in ambient atmosphere. The samples were then loaded into the diffractometer humidity chamber and sealed.

Instrumental details

Measurements were carried out on a Bruker D8 Advance X-ray powder diffractometer under controlled humidity with ambient temperature of ~23 °C. Samples were scanned at a step size of 0.02° and dwell time of 1.0 s per step. Each change in RH was accompanied by ~ 40 min of equilibration time prior to measurement. Experiments were performed with the help of Dr. David Bish (Indiana University, Bloomington, IN).

3.3.3 - Pressure-controlled XRD

High pressure experiments are performed typically in a diamond anvil cell (DAC), where pressure is applied by anvils made of diamond, through which X-rays pass for diffraction of the sample (Fig. 3.3, left). A gasket is placed around the sample to contain pressures; with the presence of a pressure-transmitting medium, the applied pressure becomes quasi-hydrostatic.[145]

XRD patterns recorded as a function of pressure were grouped into two sets of experiments: (**a**) those pre-compressed to various pressures and then recorded on a standard powder diffractometer *ex-situ*, and (**b**) those measured *in-situ* during application of a load in a DAC. Experiments and analysis of the DAC experiments were performed by Dr. Vadym Drozd (Florida International University, Miami, FL).

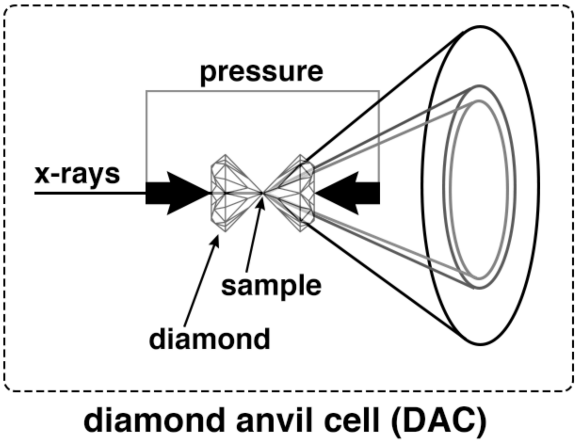

Figure 3.3: Setup of a diamond anvil cell. The sample is placed between two diamond anvils, to which pressure is applied. X-rays are sent through the diamonds to diffract from the sample.

Sample preparation

(**a**) *Ex-situ* experiments: Samples were produced with 10 % HF, or with HF+LiCl followed by K^+ exchange, according to methods outlined in section 3.2.2–3.2.3. They were equilibrated in ambient atmosphere ~ 55 % RH for 7 days, followed by equilibration for 7 days in sealed containers with saturated salt solutions[146] to produce desired humidities (dry P_2O_5 for 0 % RH; $MgCl_2$ for 30 % RH; ambient atmosphere for 55 % RH; KCl for 80 % RH; liquid water for 100 % RH). These were removed from the equilibration container and immediately transferred to a steel 1 cm diameter die, followed by pressing to 300 MPa to form a disc.

(**b**) *In-situ* experiments: $Ti_3C_2T_x$ was prepared using 10 % HF as outlined in section 3.2.2. It was sent to Florida International University where high-pressure XRD was carried out.

Instrumental details

(**a**) *Ex-situ* experiments: XRD was carried out on the pressed discs using a powder diffractometer as outlined in section 3.3.1. For experiments where material was removed from the surface of the discs, the height alignment capability of the diffractometer was used to ascertain the difference in sample height, and thus the depth of material removed.

(**b**) *In-situ* experiments: DAC experiments were performed using a symmetrical cell and diamond anvils of 900 μm culet size. A beryllium bronze gasket 350 μm thick was pre-indented to 150 μm thickness, with a 300 μm hole drilled to make the pressure chamber. Pressure was ascertained from the fluorescence shift of ruby crystals within the pressure chamber.[147] XRD patterns were collected using a GADDS/D8 diffractometer (Bruker, Billerica, Massachusetts, USA) equipped with an Apex Smart CCD detector and direct-drive molybdenum rotating anode (MacScience Co., Yokohama, Japan) with λ = 0.71073 Å. 2D diffraction images were integrated using FIT 2D.[148] Experiments were carried out by either wetting dry $Ti_3C_2T_x$ powder with enough water to make a paste before loading into the DAC, or by using water (in excess; roughly equal volumes of MXene and water) as a pressure-transmitting medium.

3.3.4 - Wide-angle X-ray scattering (WAXS)

Sample preparation

Samples were made from delaminated solutions of $Ti_3C_2T_x$ produced using the HCl+LiF methods outlined in section 3.2.2–3.2.3, and filtered to produce films as outlined in section 3.2.3.

Instrumental details

Analysis was performed on a Rigaku S-Max 3000 diffractometer (CuKa radiation source; Rigaku Corporation, Tokyo, Japan). The sample to image plate distance was 35 mm. Measurements were made in ~10^{-1} torr vacuum. Patterns were recorded on Fujifilm X-ray film and read using a RAXIA-Di system (Rigaku Corporation, Tokyo, Japan). The digitized pattern was processed using SAXSGUI version 2.08.03.

3.3.5 - Electron microscopy

Scanning electron microscopes (SEM) and transmission electron microscopes (TEM) are both widely employed in MXenes and the broader 2D materials fields. SEM, with relatively easy sample preparation, is important to MXenes mainly for morphology determination, which is critical for the study of structural changes between multilayer particles, nanosheets in various degrees of separation from one another, and films. TEM, with typically more intensive sample preparation, can reveal morphological information at much smaller scales (for example determining the number of stacked layers),[79] and the associated technique of electron diffraction is used to verify the preservation of hexagonal symmetry after etching MAX to MXene.[5] This ensures that the removal of the A layers has been a topotactic transition, and has not altered the structure, *e.g.* from hexagonal to cubic.[87]

Sample preparation

Samples were generally powders or discs attached directly to aluminum SEM stubs with double-sided conductive carbon tape. Bulk filtered films were simply

mounted with carbon tape onto the SEM stub. For deposited nanosheet samples in SEM, a drop of dilute suspension of MXene was placed on a piece of anodized alumina filter (0.1 μm pore diameter), the solvent (water) was wicked through using a paper towel, and the sample was allowed to dry before being sputter coated with Pt/Pd. The TEM samples were prepared by dropping two drops of diluted colloidal solution of MXene flakes onto a copper grid and drying in air.

Instrumental details

SEM was performed on a Zeiss Supra 50VP, typically with an accelerating voltage of 1-5 kV. TEM of the MXene flakes was performed on a JEM-2100 (JEOL, Japan) using an accelerating voltage of 200 kV. The flake size and number of layers per flake distributions were obtained through statistical analysis of more than 300 MXene flakes in the TEM images.

3.3.6 - Energy-dispersive spectroscopy (EDS)

Within the SEM, energy-dispersive spectroscopy (EDS) can also be performed. This is a useful technique for elemental analysis but has some specific limitations. Namely, that it does not distinguish chemical state (i.e. Al bound in MAX phase gives the same signal as Al bound in MXene), that the analysis is limited to the penetration depth of the incoming electrons (which can lead to improper analysis due to the sampling of surface impurities), that the standards used in interpreting signals coming from the sample are calibrated to flat and polished surfaces, which are very different than MXene powders, and that light elements such as Li, C, *etc.* are either

not observed or can tend to give inaccurate results. So while exact formula determination is out of the question, the technique can be good for rough estimates.

Sample preparation

Samples, experiments permitting, were of the form of powders pressed into discs at 300 MPa to give a flat surface. Otherwise, powders were gently compacted onto carbon tape attached to an aluminum SEM stub.

Instrumental details

EDS (Oxford EDS, with INCA software) was performed in the SEM, typically with an accelerating voltage of 10-18 kV. EDS scans were obtained at low magnification (100-200 x) at random points in the sample; at least three points per sample were used to obtain averages to calculate rough elemental ratios. XPP matrix correction was used for element quantitative analysis.[149]

3.3.7 - Thermogravimetric analysis (TGA)

Sample preparation

Ion-intercalated MXenes were prepared *via* 10 % HF+LiCl as outlined in section 3.2.2–3.2.3 and equilibrated at ambient atmosphere (~ 55 % RH) for at least 2 days prior to measurement. 8-12 mg were used for each measurement.

Instrumental details

TGA was performed on a TA Instruments SDT 2960 Simultaneous DSC-TGA in alumina crucibles under dry N_2 (Zero Grade 99.998%, passed through a molecular sieve drying column at 100 cm^3 min^{-1}), using a calibration standard of alumina

powder. Experiments were performed with the help of Dr. David Bish (Indiana University, Bloomington, IN).

3.3.8 - X-ray photoelectron spectroscopy (XPS)

XPS has been explored as a very useful technique for direct investigation of MXene surface structure.[56,72] More recent reports have utilized *in-situ* techniques to track the evolution of surface groups under changing conditions.[60] It measures the binding energy of core electrons, which is sensitive to the chemical environment of the elements. As a result, both the elemental composition and information about the charge and bonding of the elements can be examined. This has been used to determine the type and amount of MXene surface terminations, as well as general composition and presence of intercalated cations.[150] The technique is mainly limited to surface analysis, as penetration depth is relatively low; however, nanoscale materials are often not limited by this issue due to their scale. Samples may be sputtered with argon to remove potentially contaminated surface and expose clean material underneath, but in the case of MXene, care must be taken as this can alter the chemical composition or be otherwise destructive to the material.[72] Procedures in this section appear in references [150] and [151].

Sample preparation

Ion-intercalated $Ti_3C_2T_x$ was prepared as outlined in section 3.2.2–3.2.3 and pressed into discs at 300 MPa.

Instrumental details (for alkali and alkaline earth cation intercalated $Ti_3C_2T_x$)

A Physical Electronics VersaProbe 5000 instrument was used, with a 100 μm monochromatic Al Kα beam to irradiate the sample surface. Samples were in the form of pressed discs (pressed to ~1 GPa). Photoelectrons were collected by a 180° hemispherical electron energy analyzer. Samples were analyzed at a 70° angle between the sample surface and the path to the analyzer. High-resolution spectra of Ti 2p, C 1s, O 1s, F 1s, Rb 3d, Na 1s, and Cl 2p were taken at a pass energy of 23.5 eV, with a step size of 0.05 eV, while for the Li 1s region the pass energy used was 11.7 eV, with the same step size. Post-sputtering spectra were taken after the samples were sputtered with an Ar beam operating at 3.8 kV and 150 μA for 30 min. All binding energies were referenced to that of the valence band edge at 0 eV. Peak fitting details can be found in the associated reference.[150] Experiments were performed and analyzed by Dr. Joseph Halim (Linköping University, Linköping, Sweden).

Instrumental details (for alkylammonium cation intercalated $Ti_3C_2T_x$)

XPS measurements were performed on multilayer $Ti_3C_2T_x$ using a surface analysis system (Kratos AXIS UltraDLD, Manchester, U.K.) using monochromatic Al K_α (1486.6 eV) radiation. The samples were mounted on double-sided tape and grounded to the sample stage with copper contacts. The X-ray beam irradiated the surface of the sample at an angle of 45° with respect to the surface and provided an X-ray spot of 300 by 800 μm. Charge neutralization was performed using a coaxial, low energy (~0.1 eV) electron flood source to avoid shifts in the recorded binding energy (BE). XPS spectra were recorded for the elements expected, for most part, Ti

2p, C 1s, N 1s, and Li 1s. The analyzer pass energy used for all regions was 20 eV with a step size of 0.1 eV. The BE scale of all XPS spectra was referenced to the Fermi-edge (EF), which was set to a BE of 0 eV. Peak fitting was carried out using CasaXPS version 2.3.16 RP 1.6 in the same manner as in refs [56,72,77,150], while the global elemental percentage was quantified as in ref [150]. Experiments were performed and analysed by Dr. Joseph Halim (Linköping University, Linköping, Sweden).

3.3.9 - UV-Vis spectroscopy

Sample preparation

Samples of delaminated MXene suspension were taken for measurement directly after delamination, to prevent oxidation. They were diluted with distilled water to ensure that absorbance would be in an appropriate range.

Instrumental details

UV-vis spectrometry was performed in transmission mode in quartz cuvettes using a Perkin-Elmer Lambda-950 UV/visible/NIR spectrometer.

3.3.10 - Resistivity measurements

Sample preparation

Samples were in the form of films or cold-pressed discs (see previous sections for preparation method details).

Instrumental details

Resistivity measurements were performed with a 4-point probe (ResTest v1, Jandel Engineering Ltd., Bedfordshire, UK). Measured resistivity was automatically multiplied by the proper thickness correction factor by the Jandel software.

3.3.11 Computational methods

Computational techniques such as density functional theory (DFT) and molecular dynamics (MD) have been extensively employed in MXene. They have proven useful in predicting new interesting compositions to target synthetically as well as general screening,[152,114,153,154,155] shedding light on how etching reactions might proceed,[156,157] aiding in interpreting experimental results,[4,151] and suggesting what effects may arise from precise control of surface terminations (which is still somewhat elusive).[58] These procedures are taken from reference [151] and are based on a MXene $P6_3/mmc$ unit cell. They were carried out by Dr. Vadym Mochalin (Missouri University of Science and Technology, Rolla, MO).

Experimental Details

Density functional theory (DFT) and classical molecular dynamics (MD) studies were performed using Accelrys Materials Studio. A $Ti_3C_2(OH)_2$ cell was built and optimized using DFT (CASTEP module) with Perdew−Burke−Ernzerhof (PBE) generalized gradient approximation (GGA) exchange-correlation functional, energy cutoff 380 eV, 9×9×1 Monkhorst−Pack (MP) k-point set, and the following convergence criteria: energy, 5×10^{-6} eV/atom; maximal force, 0.01 eV/ Å; maximal stress, 0.02 GPa; and maximal displacement, 5×10^{-4} Å. The lattice parameters (a =

3.097, *b* = 3.097, and *c* = 20.192 Å) and angles (α = 90°, β = 90°, and γ = 120°) for the optimized cell are consistent with calculated[158] and experimental[78] literature data. Each atom in the optimized cell was assigned electric charge using a population analysis tool and Hirshfeld charging scheme.

Each AA cation was built and placed in the center of a 18×18×18 Å periodic cubic cell. The system was assigned +1 electric charge. The geometry of the cations was then optimized by DFT PBE-GGA using an energy cutoff of 310 eV on the 2×2×2MP k-point set and convergence criteria listed above for $Ti_3C_2(OH)_2$. Each atom in the optimized AA cation was assigned electric charge using a population analysis tool and Hirshfeld charging scheme. This charging scheme produced partial positive charges on N and H atoms and partial negative charges on C atoms in the AA cations as expected. For MD simulations, a 9×9×1 supercell of DFT optimized $Ti_3C_2(OH)_2$ was built and intercalated with a predefined number of each of the DFT optimized AA cations using Amorphous Cell module, producing a number of AA cation-intercalated $Ti_3C_2(OH)_2$ cells for subsequent studies. Classical MD simulations of intercalated MXenes are complicated since there is no general purpose force field that would include all atomic combinations present in MXenes and intercalants.[159] Therefore, we used the Universal force field, which has been shown to give reasonably good results for MXenes intercalated with molecular species before.[78] However, we kept the DFT calculated electric charges on all atoms in the system to achieve a better description of electrostatic interactions between the charged cations and $Ti_3C_2(OH)_2$. To release the initial stress without distorting the cell, the geometry of each AA cation intercalated $Ti_3C_2(OH)_2$ was optimized using the FORCITE

module until 2.0×10^{-5} kcal/mol (energy), 1×10^{-3} kcal/mol/Å (force), and 1×10^{-5} Å (displacement) convergence criteria were satisfied. In this step, no cell optimization was allowed. The optimized cells were subjected to thermal MD equilibration at 298 K over the period of time of 100 ps (1 fs time step) in the NVT ensemble (again no changes in cell geometry were allowed at this stage) with a simple velocity scale thermostat. By the end of the equilibration MD run, the temperature and all components of energy were well stabilized. The equilibrated cells were subjected to 500 ps NPT MD at 298 K (using Nose thermostat) and 1×10^{-4} GPa isotropic pressure (maintained with Berendsen barostat) using final configurations of the cells from the equilibration NVT MD runs as starting configurations for the data collection NPT MD. In this final step, the cells were allowed to change geometry (expand) against external pressure applied by the barostat until a new equilibrium established. During this process, the *c* lattice parameter increased according to the number of the intercalated AA cations. Snapshots of the system were saved every 1000 MD steps (500 snapshots in total) of which only the last 300 snapshots were used for analysis by the tools provided in Materials Studio. During geometry optimization and the MD runs, the electrostatic interactions were summed up using the Ewald scheme, and the van der Waals interactions were summed up using the atom-based scheme.

CHAPTER 4 - RESULTS AND DISCUSSION

4.1 - New Etching Methods

MXene is produced from MAX phase by removal of the A-layer, so techniques to produce MXene typically revolve around a chemical etchant system that selectively attacks the A elements of MAX phase without being so aggressive as to damage the metal carbide layers. From extensive trials it was determined that fluorine was an essential component of the etchant system, as most acids and bases that were tried would not attack the Al layers of Ti_3AlC_2 sufficiently. This has been recently reexamined for HCl without F through electrochemical etching, though the results are not as straightforward or efficient as established procedures.[92] Until the start of this work, MXenes were produced almost solely with HF, save for a few isolated studies, e.g. using NH_4HF_2 on thin films.[53] Due to its very hazardous nature and a desire to avoid usage of concentrated HF, we sought to generate HF *in-situ* using a mixture of an inorganic acid, HA, and a fluoride salt, MF, by the general reaction

$$HA + MF = HF + MA$$

It was known from early on that cations could be inserted into MXene structures,[9] but it had only been accomplished using fairly basic salts (e.g. hydroxides), and the insertion was done after the etching reaction had completed and the MXene was already formed. Because MXenes have been used in intercalation-based energy storage applications like batteries and supercapacitors (as discussed

previously), it was thought that the pre-intercalation of cations between MXene layers could help reduce first-cycle irreversibility (for MXenes used as electrodes in batteries, there was typically an irreversible loss of capacity after the first cycle due to ions becoming trapped permanently in the structure).[158] Further, the insertion of ions during the etching might keep deep internal areas of the MXene interlayers from collapsing, allowing better access to electrolyte during electrochemical cycling. We figured that having cations present during the etching in this new system might be able to realize these goals.

4.1.1 - Mineral Acids and Fluoride Salts

We began our study on $Ti_3C_2T_x$ (the most well-understood MXene) with a selection of alkali and alkaline earth fluoride salts LiF, CsF, and CaF_2, with HCl as the accompanying acid. LiF was chosen due to contemporary interest in MXene for Li-ion batteries, and the others for a more varied chemistry of cations. Etching was performed for 24 h at 35 ºC. After etching, washing, and drying, XRD for all three systems (Fig. 4.1) showed an expansion of the basal spacing, which was used as a positive sign that etching the *A*-layer from MAX phase was successful. In this case, as is evidenced by XRD, there are still remnants of MAX phase Ti_3AlC_2. However, the expansion was both larger than that reported for $Ti_3C_2T_x$ etched with HF alone,[2] and also dependent upon the nature of the fluoride salt used, with CaF_2 etchings showing a larger basal expansion than LiF or CsF.

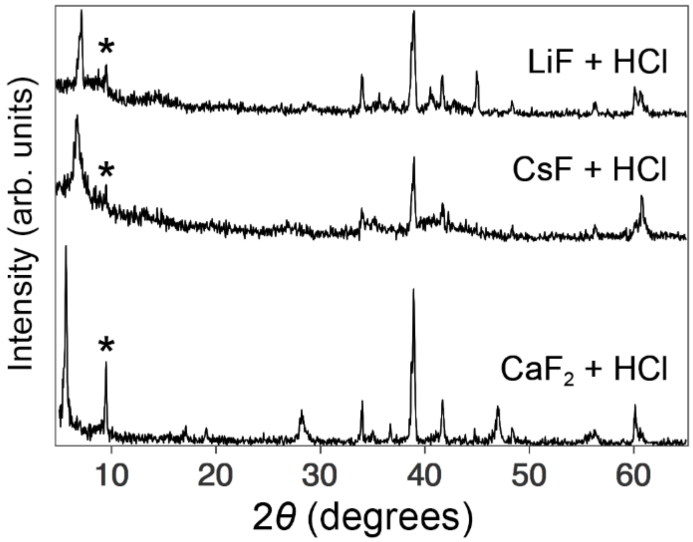

Figure 4.1: XRD of $Ti_3C_2T_x$ produced using LiF+HCl, CsF+HCl, and CaF_2+HCl. Asterisks denote the (002) reflection of residual unreacted Ti_3AlC_2.

The morphology of $Ti_3C_2T_x$ at this point in time (Fig. 4.2a), observed by SEM, was typically an exfoliated accordion-like structure.[2] However, when etched with LiF and CsF (Fig. 4.2b,c), morphologies very similar to the parent MAX phase were observed (initially this delayed the discovery of the success of this etchant system, as the particles were assumed to be unreacted MAX. This illustrates the value of not relying on one analytical technique for initial screenings. However, XRD suggested that there was only a small amount of Ti_3AlC_2 remaining, and the morphologies were similar to those observed for intercalated $Ti_3C_2T_x$,[78] so with the increased basal spacing, our first assumption was that intercalation of ions and co-intercalation of H_2O was achieved. Further, SEM of LiF+HCl etched powders showed unusual behavior (Fig. 4.2d) - it appeared that the etching caused thin sections of sheets to be easily separated from the main particles through agitation, which was not a feature of previous reports.

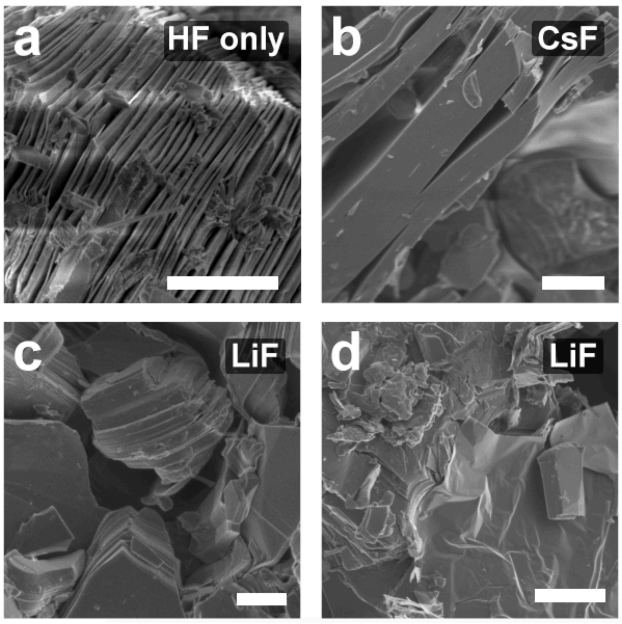

Figure 4.2: SEM images of $Ti_3C_2T_x$ produced using, a) HF only, b) CsF+HCl, and c,d) LiF+HCl. (d) Some delamination behavior and sheet separation of LiF+HCl etched particles. All scale bars are 4 μm.

To probe the effect of replacing the mineral acid, HF, HBr, and H_2SO_4 were chosen to substitute HCl, and were used under the same etching conditions (5 molar equivalents of LiF, 35 ºC and 24 h). XRD patterns of the resulting $Ti_3C_2T_x$ are shown in Fig. 4.3. The system HF+LiF resulted in high amounts of salt impurities and slower etching kinetics due to the low solubility of LiF in HF-containing solutions, in part from the common-ion effect. The other acids produced similar structures (with some differences in diffraction peak intensities), but the overall impression is that the etching from MAX to MXene is obviously not limited to HCl. This topic is left as an open route for future exploration as there could be useful findings from a full study of available acids and salts. H_2SO_4 is explored briefly at the end of this chapter in Section 4.2.3 as an alternative to HCl to help explore whether Cl is a necessary component for some behaviors and structural aspects.

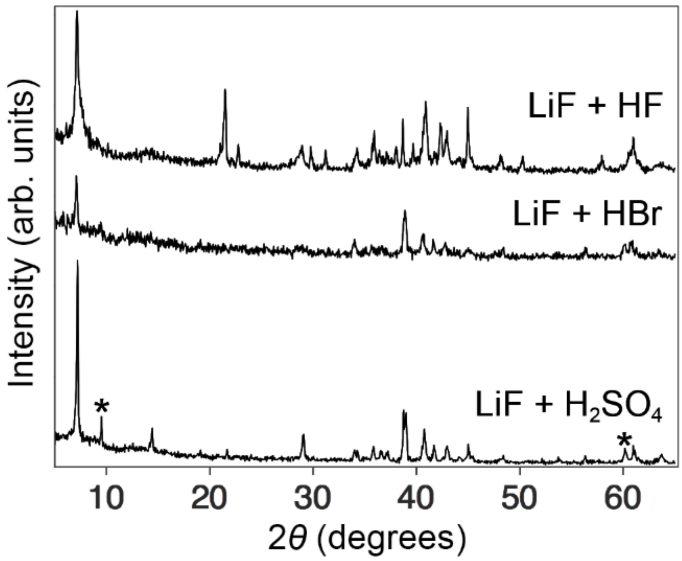

Figure 4.3: XRD of Ti_3AlC_2 powders after etching with, a) LiF+HF, b) LiF+HBr, and c) LiF+H_2SO_4. Asterisks denote the reflections of residual unreacted Ti_3AlC_2.

Focusing back on the LiF+HCl system, because the salt is the only source of F to form HF to react with Al, we sought to investigate the effect of the amount of LiF during etching. Both XRD and EDS data are presented in Fig. 4.4a. From XRD, the MAX {002} reflection only starts to be fully reduced at 5 equivalents LiF; this suggests that anything less will give incomplete reaction. This can be rationalized given that an expected byproduct, AlF_3, consumes 3 equivalents of F, and further F will react with the surface to form terminations.

The EDS results (Fig. 4.4b) give a slightly different picture when looking at the Al content (from which the percent conversion is derived as Ti_{MXene}/Ti_{MAX}, where Ti_{MXene} is calculated by taking the total Ti signal and subtracting Ti_{MAX}, assumed to be 3 times the Al signal) - it appears that the changes level off after ~ 2 to 3 equivalents. This, however, shows the limits of EDS or broad chemical analysis techniques in estimating the conversion of MAX to MXene: trapped Al-containing

byproducts are not differentiated from MAX Al and throw off the estimation. Though more painstaking, XPS can be a better technique for estimating conversion, as it is sensitive to the chemical environment of the Al.[72] From here on out, systems with at least 5 equivalents of F were used to ensure complete reaction.

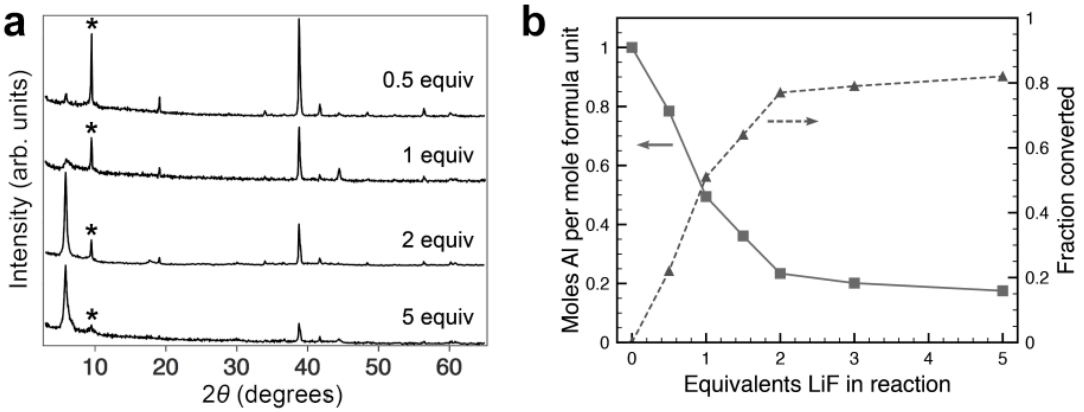

Figure 4.4: a) XRD of Ti_3AlC_2 powders after 24 h at 35 ºC, at various equivalents of LiF; b) EDS of the same samples. Asterisks denote the {002} reflection of residual unreacted Ti_3AlC_2.

As there was still some MAX present after reaction with 5 equivalents LiF, evidenced by the (002) and {*hkl*} reflections in Fig. 4.4a, the reaction time was extended to 48 h to ensure complete conversion. This had some unexpected side effects; foremost, the resulting material was observed to behave like a clay, able to be shaped, molded, and dried, as well as rehydrated and rolled into freestanding films (Fig. 4.5a-f).[79] This resulted in the largest freestanding MXene film at the time (Fig. 4.5g), far exceeding the lateral size constraints of films produced by filtering nanosheet suspensions, which were *ca.* 3 cm in diameter.

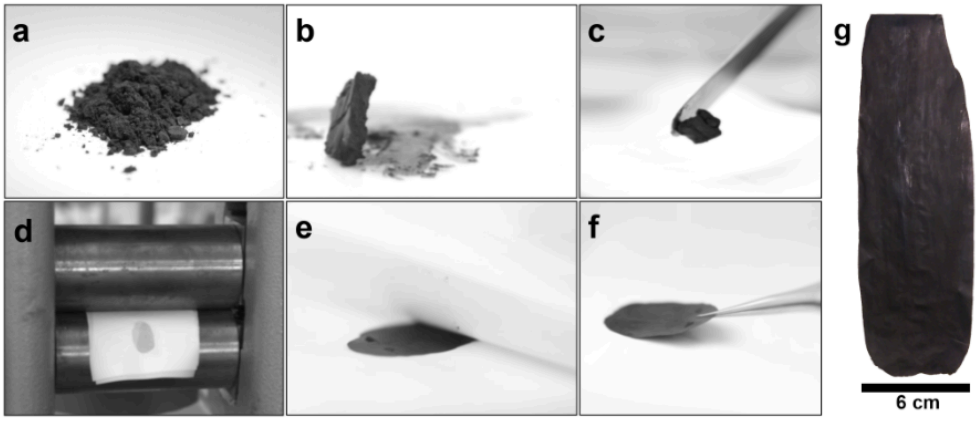

Figure 4.5: New processing techniques of LiF+HCl MXene. a) The material can be stored as a dry powder. b) As water is gradually introduced, the material takes on a clay-like consistency. c) Adding more water allows the material to be easily spread, or d) rolled on a CelGard membrane. e) The CelGard easily detaches once dry leaving, f) a free-standing film. The entire process inclusive of drying lasts about 0.5 h. g) The largest continuous MXene film of its time, produced by rolling.

SEM revealed the morphological reasons behind the stability of these films - the particles tended to shear, producing regions of tangled and interlocked nanosheets, which was not replicated in powders etched with HF alone (Fig. 4.6a). Some porosity in the middle of the film is also evident due to mostly-intact particles (with shearing highest near the surfaces). The particles etched with LiF+HCl were also observed to have a dynamic response to water, swelling reversibly in the *c* direction, which could facilitate higher lubricity during film rolling (Fig. 4.6b). When equilibrated in ambient atmosphere (roughly 50 % RH), the basal spacing ranged from 12.5-13.5 Å (this variability will be addressed later); when liquid water was introduced, the basal spacing increased to ~ 16 Å.

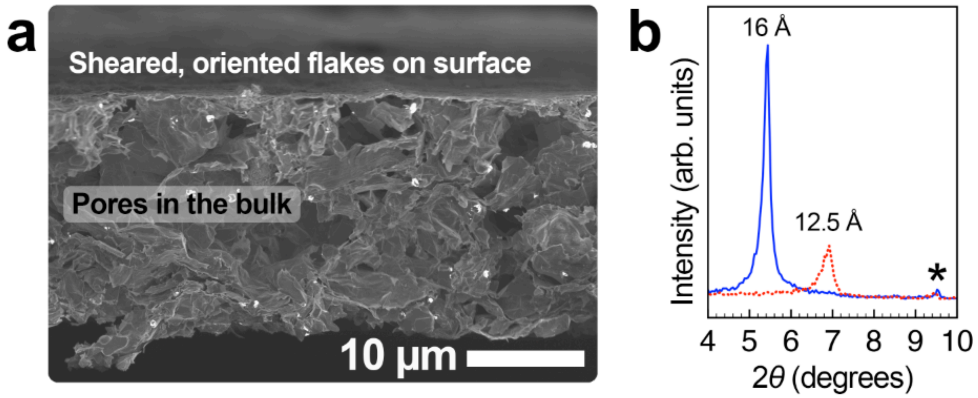

Figure 4.6: a) SEM image of the cross section of a rolled film, showing sheared nanosheets on the surface oriented with their basal planes along the film surface and pores in the bulk, as the inside is composed of mostly undisturbed multilayer particles. b) XRD of the LiF+HCl $Ti_3C_2T_x$ in the ambient state (dotted trace) and the wet state (solid trace), showing its crystalline swelling ability. Asterisks denote the {002} reflection of residual unreacted Ti_3AlC_2.

Attributed to the expanded interlayer spacing, presence of H_2O, and porosity, these rolled films proved to be excellent anodes for asymmetrical supercapacitors, produced quickly and in one step, taking about a tenth of the time of contemporary production.[79] The phenomena behind the electrochemical energy storage particular to MXene have since begun to be elucidated (such as mechanisms for pseudocapacitance, changes to oxidation state of M atoms in the MX sheets, and participation of surface terminations),[65,95,64,160] while the rest of this work has been focused on other physical phenomena arising from the new etching methods.

Given the observed ability for the nanosheets to slide and migrate, the second major side effect of this new etching process was the spontaneous delamination of multilayer particles of $Ti_3C_2T_x$ to produce suspensions, simply by shaking; these had a characteristic green color (Fig. 4.7a). Deposition of dilute suspensions onto anodized alumina membranes (Fig. 4.7b) confirmed that the suspensions were indeed

composed of nanosheets; these could be made into bulk films *via* filtration (Fig. 4.7c) or dropcasting (Fig. 4.7d). TEM analysis of deposited nanosheets (not included in this work; see ref. [79] for details) showed that the nanosheets were of large lateral size (2-3 μm, Fig. 4.7e) and were largely single-layer (Fig. 4.7f).

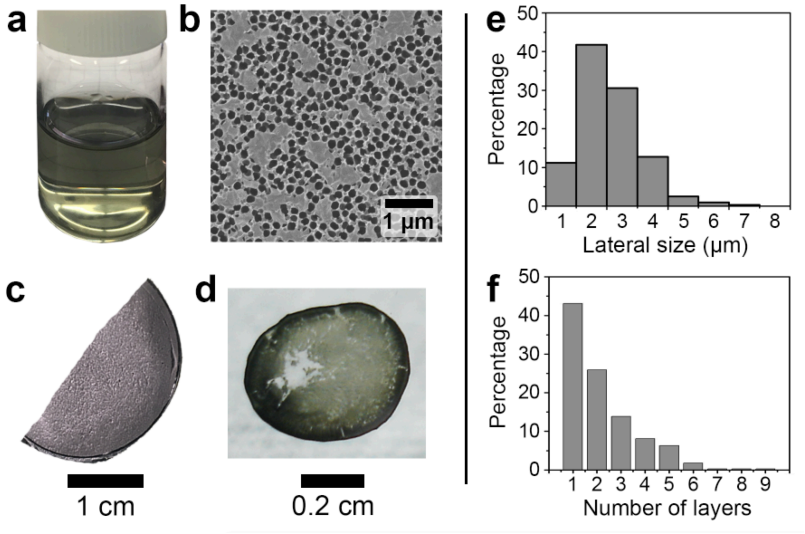

Figure 4.7: Delaminated LiF+HCl $Ti_3C_2T_x$. a) A suspension of nanosheets has a characteristic green color. b) SEM image of nanosheets deposited on an anodized alumina membrane. c) Photograph of a $Ti_3C_2T_x$ film produced by filtration of suspension. d) Drop-cast film on glass showing a persistence of the green color even after drying. e,f) TEM analysis of size and thickness distributions from over 300 nanosheets.

The impact of this new processing technique on production of MXene nanosheet suspensions has been quite large (the paper that introduced it has 489 citations at time of writing), and the it has become the dominant process for $Ti_3C_2T_x$ nanosheet production in many new publications. Such suspensions are critical for processes including film production through filtration, spin-coating,[83,83] spray-coating,[84] polymer composite production,[80] electrospinning,[85] *etc*. Since its development, there have been refinements of the system to produce higher nanosheet

concentrations, *e.g.* by using higher concentrations of LiF and HCl for shorter times.[161,162]

As an aside to the flexibility of this procedure, we have gone on to produce nanosheet suspensions of Ti_2CT_x,[83] and Mo_2CT_x,[77] as well as $(Mo_{2/3}Ti_{1/3})_3C_2T_x$, $(Mo_{1/2}Ti_{1/2})_4C_3T_x$, $Ta_4C_3T_x$, and $Nb_4C_3T_x$ (the latter group from unpublished preliminary results). Photographs of the suspensions and UV-vis spectra of $Ti_3C_2T_x$ and Ti_2CT_x are shown in Fig. 4.8 to showcase the modulation of optical properties by MXene structure and composition.

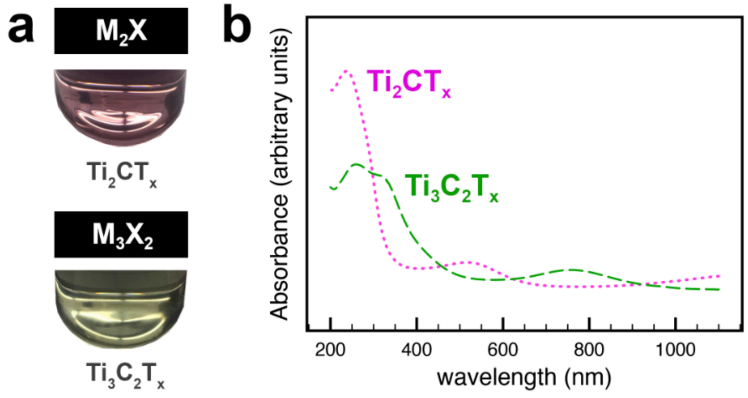

Figure 4.8: a) True-color photographs of suspensions of MXene nanosheets of $Ti_3C_2T_x$ and Ti_2CT_x, both produced by LiF+HCl method. b) UV-Vis spectra of the same solutions. The y-axis is absorbance but the absorbance values are not absolute.

At this juncture, since the work revolves around distinctions between multilayer particles and single nanosheets, it is important to note a few things about MXene structure. First, although the parent symmetry of MAX is $P6_3/mmc$, it is not necessarily preserved upon etching of the A layer to form MXene, and is definitely not preserved when nanosheets are delaminated and randomly restacked. This disruption in symmetry is caused by small rotations and translations of the sheets

relative to one another. Thus, to be precise, lowest-order basal reflections in MXene should not be necessarily constrained to (002), because that is a limitation from the $P6_3/mmc$ space group. Second, it was long assumed that the disappearance of the {110} reflection is evidence of such disruption of the unit cell (i.e. shearing of nanosheets).[4,78,79,81,163,164,165] After comparison to similar phenomena in other materials,[166,167,168,169] we have conclusively shown that the reason for the disappearance of the {110} reflection is due to orientation/textural effects and not from nanosheet shearing, as the planes of atoms that give rise to {110} reflections are present in high amounts even in single nanosheets. This was accomplished by obtaining diffraction patterns from typical filtered films of $Ti_3C_2T_x$ in non-standard orientations (typically, they are laid in a horizontal position, or flat on the substrate). The XRD patterns obtained when the films were flat on top of, normal, and at ≈ 57 ° to the substrate are shown in Fig. 4.9a, b and c, respectively. In the first column, in Fig. 4.9a, the film is measured in a standard horizontal orientation (see schematics below the diffraction patterns). The experimental data are displayed as curves, with powder XRD patterns generated using CrystalDiffract as vertical lines. The preferential orientation of the MXene nanosheets is apparent, with only (00*l*) (basal) reflections present (the peak at ~ 18° comes from a higher-order (00*l*) reflection of a second hydrated phase present as an impurity, evident by a small shoulder on the lowest-angle basal reflection). In Fig. 4.9b, the film has been oriented vertically, with the film perpendicular to the beam (in transmission). Here, there are two major reflections, corresponding to {010} and {110} plane families, which are aligned well to satisfy the Bragg condition in this orientation. In Fig. 4.9c, the angle of 57º to the

substrate was chosen because it should place {01*l*} reflections in the path of the detector if they are present (for a more detailed treatment of this reasoning, see ref. [170]). The resulting XRD pattern shows only a small hump where these reflections would be expected, but no distinct peaks.

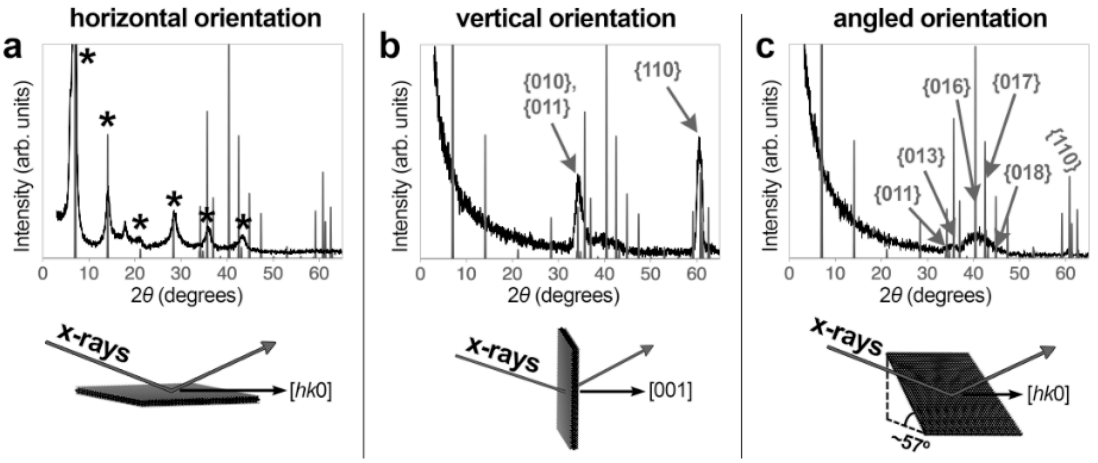

Figure 4.9: Top panels: XRD patterns (dark traces) of the same $Ti_3C_2T_x$ filtered film in various orientations. Lighter lines are calculated XRD powder patterns. Asterisks denote {00*l*} series of reflections. The orientation of the films, in schematics at bottom, are a) typical horizontal, b) vertical (transmission), and c) parallel to the beam but with one side angled at 57 degrees.

To confirm the conclusions reached from the powder diffractometer, we performed wide-angle x-ray scattering (WAXS) on the same $Ti_3C_2T_x$ film in transmission mode (as in Fig. 4.9b), presented in Fig. 4.10. Apart from two artifacts in the ring pattern (Fig. 4.10a, marked as white arrows), the pattern shows full rings, confirming the random rotational disorder of the MXene nanosheets in the film. The pattern was processed into an averaged 1D intensity *vs*. *q* curve (Fig. 4.10b) to compare to the powder XRD patterns from Fig. 4.9. The peaks in this pattern (and labeled rings in Fig. 4.10a) correspond to the plane families of: (i.) (00*l*) (ii.), {010}

(iii.), {01*l*} and (iv.) {110}. Importantly, in the full WAXS pattern we see no significant peaks for {01*l*} planes, and only a broad hump instead.

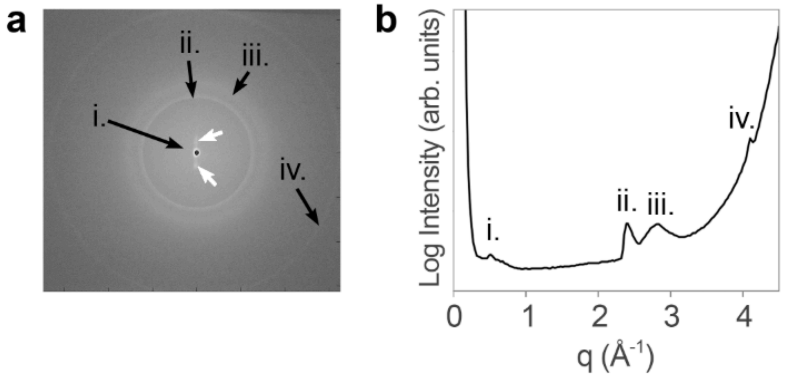

Figure 4.10: a) WAXS photographic plate of $Ti_3C_2T_x$ filtered film in transmission mode. The white arrows at center denote artifacts from the film. The marked rings arise from (i) (00*l*), (ii) {010}, (iii) {01*l*}, and (iv) {110} reflections. b) 1-dimensional plot of intensity *vs* scattering vector *q* ($Å^{-1}$); the plot was generated by averaging the intensity of a polar transformation of the plate in (a) and calibrating *q* to a pattern collected from silicon powder at the same conditions. The marked regions i through iv are the same as in (a).

This low-intensity hump is observed around the location of a number of expected {01*l*} reflections ({011}, {013}, {014}, {016}, {017}, {018}, and {019}, region iii.), but no significant peaks are observed, hence there is expected to be little significant preservation (or re-forming *via* ordered restacking) of the original $P6_3/mmc$ unit cell. The absence of strong reflections in this region, as well as in the angled film from the standard powder diffractometer experiments, shows that there is no long-range order of the nanosheets' stacking, as these reflections originate from higher symmetry such as $P6_3/mmc$ (and are indeed observed in ML $Ti_3C_2T_x$, exhibiting well-ordered stacked nanosheets, presented earlier in this chapter).[150] We remind the reader that this is a hexagonal crystal system, and these plane families are shown for simplicity in {*hkl*} notation; to better understand the relation of the

families to one another they should be converted to {*hkil*} notation. Using both the standard diffractometer and WAXS results, we calculate the *a* parameter (2 x d_{110}) as 3.06 Å. This is in decent agreement with the literature.[68] It also demonstrates the ability to measure the *a* lattice parameter of filtered films with ease, something that has not been reported in publications that analyze these films with powder diffractometry. With improved accuracy, this could make for an easy way to study changes in film structure as a result of intercalation or composite formation.

Section Summary

In response to the limited means by which MXenes could be produced early on, new etching systems were pioneered for the reasons of increased safety and potential for ion pre-intercalation for electrochemical energy storage applications. Multiple systems were explored, with LiF+HCl being the most effective. Unexpected outcomes of this etchant system were the facile production of a clay-like material that could be shaped and rolled into large-scale films (which showed excellent performance in electrochemical capacitors), the discovery of clay-like swelling on the unit-cell scale, and the production (shortened in time by an order of magnitude) of high-concentration suspensions of MXene nanosheets that are critical as the basis for many further processing methods. The latter has essentially reshaped how suspensions of $Ti_3C_2T_x$ are produced in the field of MXenes. As a contribution to structural understanding, an early misconception on the interpretation of the presence of {110} reflections was revisited and corrected.

Future Work

The best achievement of the HCl+LiF system is its ability to produce high concentration suspensions of $Ti_3C_2T_x$ and Ti_2CT_x, and it shows much promise as a gentle etching method to produce MXene nanosheet suspensions of other compositions. However, our experiments here were focused on optimization rather than deep understanding. It is in the interest of the community to better understand, for example, the effects of solubility of added salts and how that solubility affects the reaction parameters and products. Currently, the growth in the number of synthesized MXenes with new elemental compositions outpaces the methods by which they can be successfully delaminated into concentrated suspensions, so there is much work to be done here on refining etchants and conditions. Further, the vibrant and diverse colors of the nanosheets produced to date offer an enticing project to understand their optical physics, effects from transmission but also reflection of light.

4.1.2 - Hydrofluoric Acid and Halide Salts

While the general system HCl+LiF showed excellent performance for specific tasks such as producing suspensions of MXene nanosheets and making electrodes, some of the major limitations were the kinetics of etching (requiring higher temperatures / longer times than systems using HF) and some level of unpredictability of ionic composition - with such high levels of available H^+ by using concentrated HCl, for example, there may be interference with desired cation intercalation. For the latter, given the concentrations of HCl used, and the developing knowledge of ion exchange in MXenes, the possibility of exchange between Li^+ and H^+ (or H_3O^+) likely led to inconsistencies in the interlayer distribution of multiple cations. This

work was moving in the direction of studying clay-swelling phenomena, where control of ionic composition is paramount, so we decided to return to a primarily HF-based etching system, with additions of salts to provide ions during etching. This naturally leads to choices in both the cationic and anionic composition of the salt which must be understood and optimized.

Because intercalated cations are of the foremost importance when dealing with applications, their compositional control was the first to be explored. At this stage, XRD was used as the primary tool to verify a single-phase material. It was clear from the work of the previous section that different cations can trigger observable changes in the basal spacing. Fig. 4.11a shows the result of etching with 10 % HF and 5 equivalents of LiCl (for 24 h at 25 ºC). In contrast to essentially all contemporary diffraction patterns of MXene (see reference [2] for an example of typical diffraction patterns from $Ti_3C_2T_x$ produced by HF), this system led to a structure that was very well matched in both peak positions and intensities by a single-phase pattern calculated simply by setting a fixed basal spacing, with all expected peaks present. Crystallographic data for the structure were space group $P6_3/mmc$, a = 3.042 Å, c = 24.512 Å, i.e. a basal spacing of 12.25 Å. When other cations were used, substituting either NaCl or TMACl for LiCl (Fig. B1b), the resulting diffraction patterns showed far less ordered structures, although there was clearly change occurring - e.g. when TMACl was present, the basal spacing increased to 14.3 Å. Based primarily on diffraction data for our target of a single-phase system, we determined Li^+ to be the best cation present during the etching. This could partially be due to solubility differences between LiCl and other chloride salts in the HF solution. Methods of

introducing other cations to the interlayer space will be developed in later sections through the process of ion exchange.

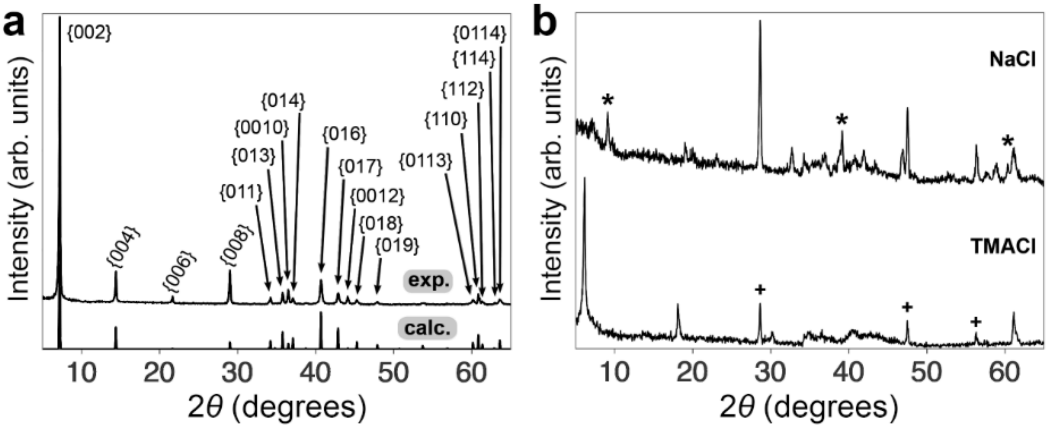

Figure 4.11: a) Experimental (top) and calculated (bottom) powder XRD patterns for $Ti_3C_2T_x$ etched with HF+LiCl. b) Powder XRD patterns of $Ti_3C_2T_x$ etched with HF+NaCl (top) or TMACl (bottom). Asterisks denote the (002) reflection of residual unreacted Ti_3AlC_2; plus signs denote crystalline Si added as an internal standard.

Focusing on Li-based etching systems, we finalized our compositional study by varying the anion, using HF combined with either LiF, LiCl, LiBr, or LiI. LiF is highly insoluble in HF, producing less reliable results and many impurities, and was already covered in Fig. 4.3. XRD from the latter three (24 h at 25 ºC) are shown in Fig. 4.12. In the ambient-atmosphere state (Fig. 4.12a), the patterns from LiBr and LiI samples were similar to LiCl, displaying the same peaks, although the peaks for the LiCl sample were qualitatively sharper. Differences were found, however, when the samples were exposed to liquid water (Fig. 4.12b). The LiCl sample basal spacing swelled to 16.2 Å, but neither the LiBr nor the LiI samples showed any change from their starting point of 12.25 Å. According to EDS analysis of the powders in Fig. 4.12c, the LiCl sample retains Cl in the structure while the others do not retain

detectable amounts of Br or I. At this point, a possible explanation for this could be that Cl, and not Br or I, is able to react with MXene to from a surface termination, acting as a steric spacer to give more room in the interlayer space for enhanced water diffusion. In support of this, allowing the LiBr and LiI samples to sit in liquid water for 2 days did show a trace of the 16.2 Å spacing forming, which would be consistent with much lower diffusivity of water; further, there have been recent publications on the potential for Cl surface terminations to have steric effects allowing for greater diffusivity, in the area of Li^+ diffusion.[57]

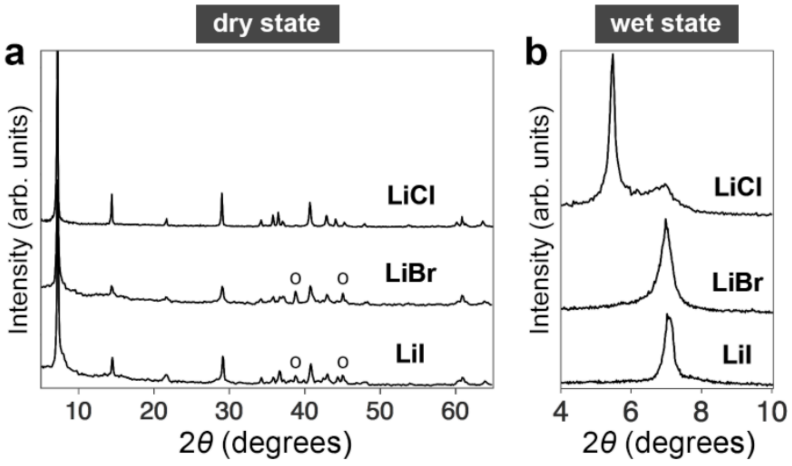

Figure 4.12: XRD patterns, a) in the dry (ambient atmosphere / 50 % RH) state of $Ti_3C_2T_x$ etched with HF+LiCl (top), HF+LiBr (middle) and HF+LiI (bottom) – open circles denote LiF salt impurities; b) of the basal region of the same materials in the hydrated state (exposed to liquid water).

Based on the facts that LiCl samples showed the dynamic swelling response to liquid water that LiBr or LiI samples did not, and that the system HF + LiCl produced the most phase-pure MXene, that system was chosen as a starting point for all future work. A set of experiments probing the effect of varying the equivalents of LiCl

during the etching, as well as its effect during washing, were set up to optimize and better understand the system. First, etchings were set up with 10 % HF and 1, 3, 4, 7, 9, or 20 equivalents of LiCl. XRD of the resulting MXene from these etchings is shown in Fig. 4.13a in the ambient state and in Fig. 4.13b in the wet state. Given the consistent etching conditions of 24 h and 25 ºC, 5 equivalents LiCl was determined to be optimal because lower amounts resulted in less-ordered structures (as judged by the 00*l* peaks), while higher amounts resulted in the continued presence of unreacted MAX phase, likely due to reduction in the effective concentration of HF from reaction of it with LiCl to precipitate the far less soluble LiF.

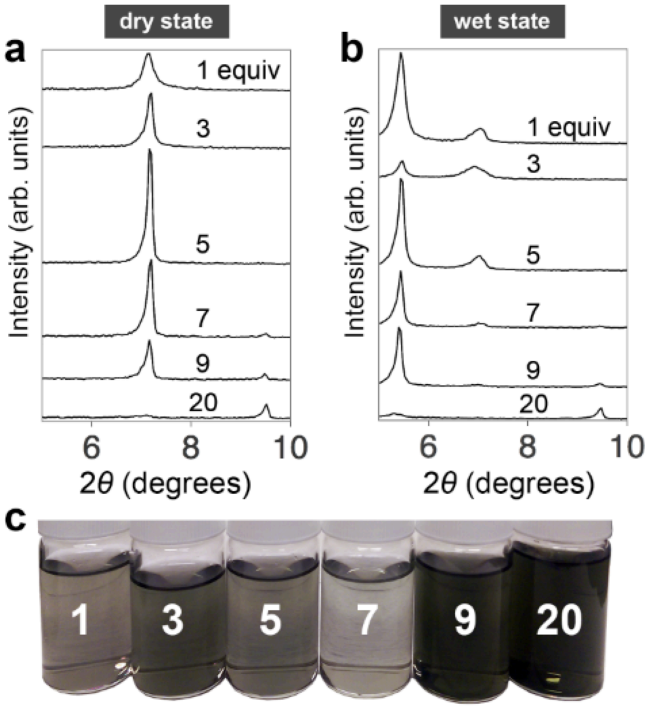

Figure 4.13: Powder XRD patterns of the basal region of $Ti_3C_2T_x$ etched by HF+LiCl, at various loadings of LiCl into the etchant (equivalents per Ti_3AlC_2). a) In the dry state (ambient atmosphere / 50 % RH); b) hydrated state (exposed to liquid water). c) Photographs of supernatants from late in the washing step, showing spontaneous delamination to different degrees depending on the amount of LiCl used in the etching.

As observed with HCl + LiF from before, Fig. 4.13c shows photographs of green suspensions obtained during the washing, at pH toward neutral; this is indicative of some degree of spontaneous delamination of particles, although in much lower concentrations here. There seems to be some mild correlation between the degree of swelling with H_2O as judged by Fig. 4.13b and the concentration of the suspension, but this was not explored further, as the goals of coupling HF with salts were rather to make ordered, crystalline structures to study ion exchange.

With the etching conditions set at 10 % HF, 24 h, 25 ºC, and 5 equivalents LiCl, we investigated what happens during the critical washing steps following the etching process, by removing aliquots of sample as washing proceeded (and measuring the pH of the supernatant above the aliquot) and obtaining diffraction data, in the ambient and wet states; these data follow in Fig. 4.14. It is clear that during washing, not only are acids and byproducts removed from around the MXene particles, but that change is also happening to the interlayer spacing. Fig. 4.14a shows that the strong ordering of the interlayer is not developed until the MXene is washed to pH ~ 5. The low-pH fractions show that the interlayer is initially somewhat disordered, with the potential presence of *e.g.* AlF_3, CO_2, HF, and other species. The regions where order is lost (pH 0-1.5) coincide with visually-observed gas release in the form of bubbles during washing. Fig. 4.14b shows that, for all samples where a peak for basal spacing of 12.5 Å is present, addition of liquid water activates swelling to 16 Å.

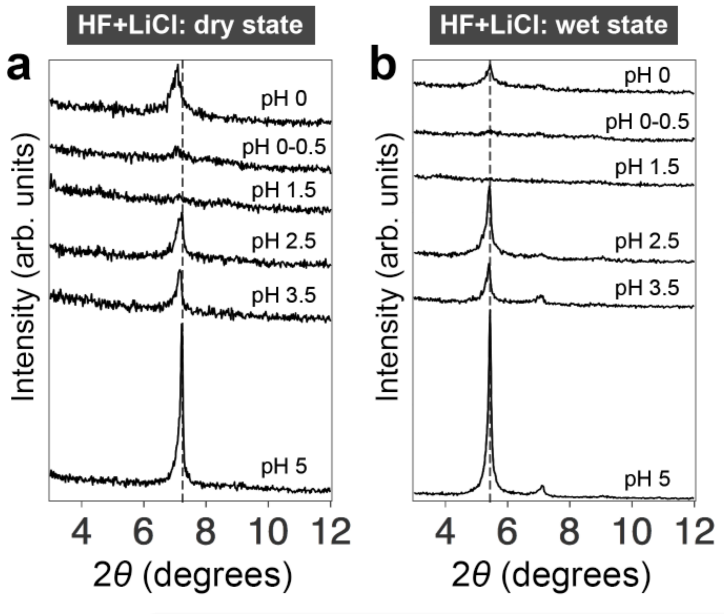

Figure 4.14: Powder XRD patterns of the basal region of $Ti_3C_2T_x$ etched by HF+LiCl (5 equivalents), at each stage in the washing procedure, with the increasing pH measured roughly by pH test strips. a) Dry state (ambient atmosphere / 50 % RH); basal spacing ~ 12.3 Å. b) Hydrated state (exposed to liquid water), basal spacing ~ 16.2 Å.

The fact that the samples at pH 0 (*i.e.* no washing) display some ordering and water-swelling behavior, and that the ordering is highest at the end of the washing, suggests either that intercalation of ions occurs mainly during the washing steps, or that the ions are present primarily from the etching and the structure is refined during washing. In order to help shed light on this question, we prepared an etching of 10 % HF alone (24 h, 25 ºC) and did the same analysis, but using 1 M LiCl (aqueous) instead of distilled water for the washing; these data are presented in Fig. 4.15 in both the ambient and wet states. If the bulk of intercalation of ions occurred during the washing, we should see the same kind of results as in the previous figure. However, looking at the wet state in Fig. 4.15b, the only time swelling is observed is when LiCl

is introduced at very low pH, and even then the structural changes are very subdued; the effect is no longer seen as the pH is raised.

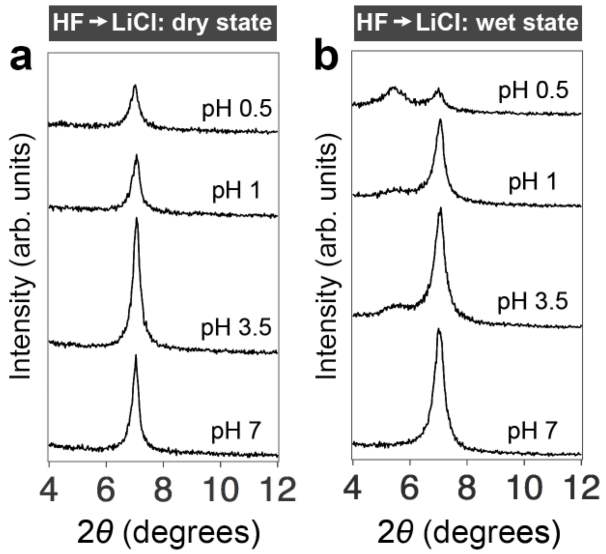

Figure 4.15: Powder XRD patterns of the basal region of $Ti_3C_2T_x$ etched by HF10 and washed with 1 M LiCl, at each stage in the washing procedure, with the increasing pH measured roughly by pH test strips. a) Dry state (ambient atmosphere / 50 % RH); basal spacing is ~ 12.6 Å. b) Hydrated state (exposed to liquid water), basal spacing is ~ 12.6 Å, with a small peak at 16.2 Å.

Section Summary

Due to the capabilities of producing more ordered single-phase structures for further study, we returned to HF with the addition of salts during the etching process to control intercalation of cations. Salts such as NaCl and tetramethylammonium chloride had only limited success, while LiCl proved the best additive, demonstrating the same type of crystalline swelling as observed in the previous section. Neither LiBr nor LiI produced a structure that demonstrated swelling to a high degree. It was found that the optimal addition of LiCl to 10 % HF etchant was 5 equivalents per Ti_3AlC_2.

Washing was further explored and shown to be a critical step in determining the degree of ordering of the structure, and it was shown that it is best to have LiCl present during the etching process, as it is not easily introduced after etching with HF alone.

Future Work

There are many new questions generated by the results in this section that can be explored. We currently have a good idea of what kind of etchant systems produce what products, but we have very little knowledge about what actually happens during the etching, apart from e.g. some computational studies,[156,157] and observations of potential etching byproducts such as AlF_3 and H_2.[66,171] For example, we still do not know the exact functionality of Cl, though it is always present in the final MXene when it is used in the etchant (this is clear from EDS); some combinations of acids and salts may work better for certain MXene compositions than others; and the exact role of the balance of ions in the delamination of MXenes is currently unresolved.

4.2 - Ion Exchange

With the ultimate goal of understanding how structural properties of MXene change with different intercalated cations, and with failed attempts at making highly ordered, single-phase $Ti_3C_2T_x$ intercalated with cations other than Li^+ by etchant additives alone, we began with Li-$Ti_3C_2T_x$ produced by HF+LiCl and attempted ion exchange. This process involves soaking the material containing interlayer ions in a solution of salt with the desired replacement ion, and allowing the ions to diffuse to replace one another, as is common in clay minerals.[20]

4.2.1 - Ion Exchange: Alkali and Alkaline Earth Metals

Because the alkali and alkaline earth series cations are so prevalent in clay minerals and are used frequently for electrochemical energy storage applications, these series were a natural starting point for MXene. The controlled insertion of these cations was accomplished by etching Ti_3AlC_2 with 10 % HF and 5 equivalents LiCl (24 h, 25 ºC), washing initially with HCl to remove traces of LiF impurity (the low-soluble salt LiF produced by the reaction HF + LiCl = HCl + LiF), and soaking the MXene powders in a 1 N solution of the chloride salt of the desired cation for 24 h. At the end of this period the powders were washed with distilled water to remove traces of the salt, leaving only intercalated cations. X-ray photoelectron spectroscopy, carried out by Dr. Joseph Halim,[150] verified that:

1. The Li 1s region shows no signal in samples etched with HF alone, but shows signal attributable to intercalated Li^+ from $Ti_3C_2T_x$ etched in HF + LiCl (Fig. 4.16a)

2. After ion-exchange is performed (using Na and Rb as examples because the binding energy regions for these cations in the XPS spectra did not interfere with those of other elements), the signal from the Li 1s region disappears, followed by appearance of signal in the Na 1s and Rb 3d regions, respectively (Fig. 4.16b, c)

3. The number of intercalated cations present per Ti_3C_2 unit was found to be between roughly 0.16 and 0.3. The relevance of this value will be discussed in further sections. These values are in line with original reports of $Ti_3C_2T_x$ reacted with KOH to intercalate K^+ (with the number of cations at ~ 0.32).[9]

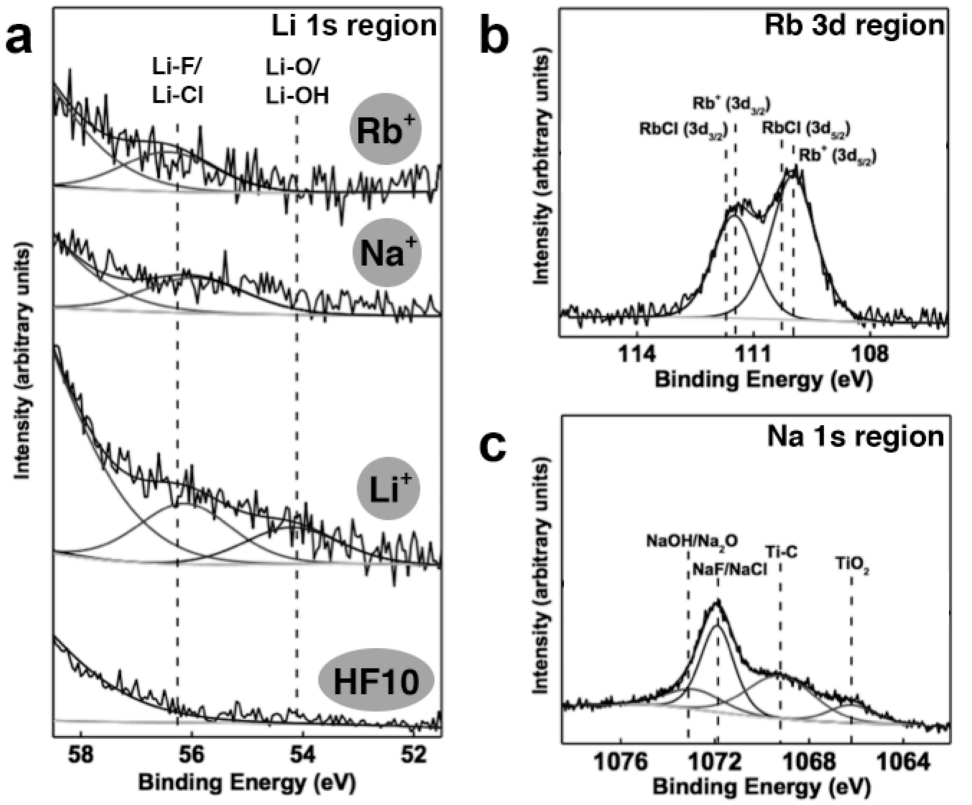

Figure 4.16: Un-sputtered XPS spectra of, a) Li 1s region of $Ti_3C_2T_x$ produced by HF10, HF+LiCl, HF+LiCl followed by NaCl exchange, and HF+LiCl followed by RbCl exchange. Li-F/Li-Cl peaks arise from salt impurities; Li-O/Li-OH peaks arise from the presence of cationic Li^+. b) Rb 3d region of $Ti_3C_2T_x$ produced by HF+LiCl followed by RbCl exchange. c) Na 1s region of $Ti_3C_2T_x$ produced by HF+LiCl followed by NaCl exchange. Original data from ref [150].

Thus chemical means verified that cations are present in the structure where we intended, and that they are truly exchanged in the presence of other cations. Fig 4.17a shows the effect of the HCl pre-wash on the Li-$Ti_3C_2T_x$ – a water-only wash leaves traces of LiF salt (bottom pattern, marked with open circles), while the pre-wash with HCl followed by cation intercalation results in retaining of the original structure, with the removal of the salt traces (top pattern). The middle pattern is Li-$Ti_3C_2T_x$ that was subjected to an HCl pre-wash but then not re-washed with LiCl

solution. The structure is more reminiscent of un-intercalated $Ti_3C_2T_x$, with a broad basal reflection at ~ 10 Å. This result opens the possibility that H^+ or H_3O^+ from HCl may be able to exchange with cations, and upon drying may not remain hydrated, thus collapsing the structure.

As to the reversibility of the exchange, in a separate experiment, Li-$Ti_3C_2T_x$ (basal spacing of 12.25 Å) was made and exchanged with $MgCl_2$ according to the methodology above; an aliquot of the now Mg-$Ti_3C_2T_x$ was removed and saved for XRD, and then the bulk of the Mg-$Ti_3C_2T_x$ was exchanged with LiCl. XRD of the 00*l* region in Fig. 4.17b shows the results of the exchange, where basal spacing of Mg-$Ti_3C_2T_x$ has shifted to 15.0 Å, and returns to its original position when the Mg^{2+} is again swapped for Li^+. It is very clear from this initial result that cation intercalation can have drastic effects on structure, but also that ion exchange is a reversible process whereby that can be readily controlled.

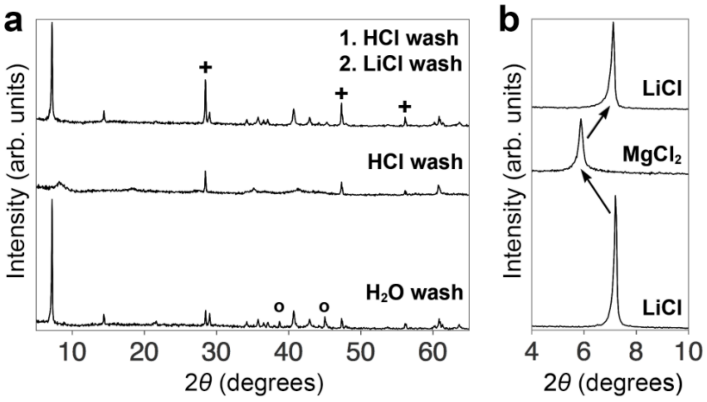

Figure 4.17: Powder XRD patterns of $Ti_3C_2T_x$ etched with HF+LiCl; a) Following etching, washed with water only (bottom), with basal spacing of 12.5 Å; the same etching, followed by washing with HCl and then water (middle), with basal spacing of 10.5 Å; the same etching, followed by washing with HCl, then LiCl, then water, with basal spacing of 12.5 Å. b) followed by washing with HCl, then LiCl, then water (bottom pattern); after exchange with $MgCl_2$ (middle pattern); after re-exchange with LiCl (top pattern). Basal spacings modulate between 12.5 Å and 15 Å.

This exchange methodology was extended to allow for the full series of Li^+, K^+, Na^+, Rb^+, Mg^{2+}, and Ca^{2+} to be intercalated. All except for Rb^+ were chosen for further structural study. The materials were subjected to *in-situ* controlled-humidity XRD at Indiana University under the guidance of Dr. David Bish. The results from these experiments are shown in Fig. 4.18 - all three panels display the same data, presented in different ways to give a more complete picture. For each experiment, the sample was introduced as a wet paste and equilibrated at ~ 95 % RH; after data were gathered, the humidity was reduced with stepwise equilibrations until 0 % RH, after which it was raised again to get a sense of the reversibility of the process. Fig. 4.18a shows the evolution of diffraction intensity (colored; highest intensity is represented as red, yellow, then green and blue) along 2θ (x-axis) as the humidity is varied (y-axis) from 95 % to 0 %, back to 95 %, in the direction indicated by the arrow. Fig. 4.18b shows more typical plots of intensity against 2θ to show the shape of the peaks. Finally, Fig. 4.18c shows 2θ values of the peak centers plotted against relative humidity.

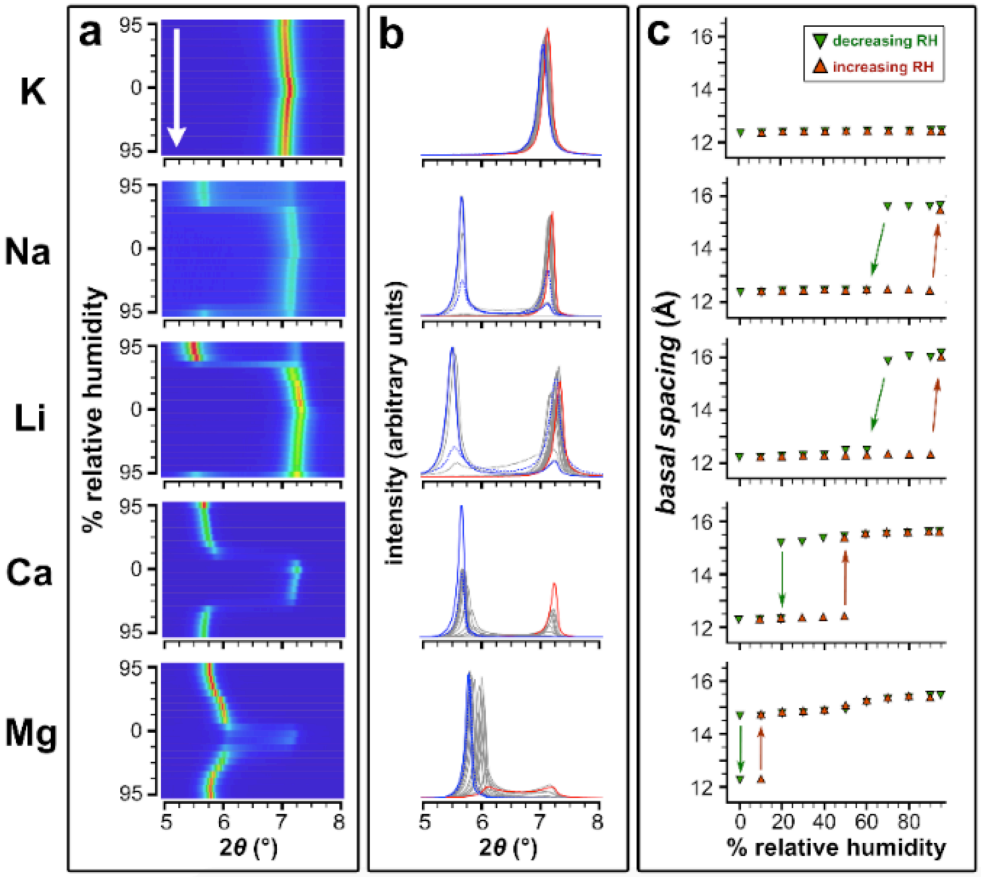

Figure 4.18: XRD data for Li-$Ti_3C_2T_x$ after exchange with various metal cations as relative humidity is varied and given time for equilibration. a) 2-dimensional plots showing diffraction intensity (red = most intense) as a function of 2θ and as the humidity is varied in the direction of the arrow (starting at 95 %, decreasing to 0 %, and increasing again to 95 %). b) The same data, presented in more standard form, that allows peak shape to be seen. c) Basal spacing extracted from the XRD data plotted against relative humidity.

At 0 % RH, all samples display a basal spacing of ~ 12.5 Å. Taking non-intercalated $Ti_3C_2T_x$ to be ~ 10 Å,[2] this gives a difference of 2.5 Å, which is close to the van der Waals diameter of the H_2O molecule at 2.76 Å.[172] At higher humidities, they display basal spacing values of roughly 2.5-3 Å higher, corresponding to a further H_2O molecule diameter. Thus it has been suggested that water intercalation can be visualized as filling the interlayer with a layer of H_2O, after which the interlayer expands at high humidity to accommodate another layer of H_2O. More

realistically, these are likely not layers but rather hydration shells of the cations filled to varying degrees.[10] Because the coordination of H_2O around metal centers may adopt different structures, e.g. planar, tetrahedral, octahedral, this can result in the same basal spacing as discreet layers of H_2O, and can explain why in some cases the layer spacing is not quite in H_2O diameter multiples, why there is some variability between ion types, and finally why there is some continuous variability in the basal spacing over the course of the humidity changes. In the clay literature, the phase containing 1 'layer' of H_2O can be referred to as 1W, with the 'bilayer' phase as 2W.[23]

The asymmetry in the plots along the humidity axis demonstrates that the rehydration response is energetically different than dehydration. This is further shown in Fig. 4.18c, with the hysteresis clearly visible. The best explanation for this is that once H_2O is removed and the layers collapse, there is an energy barrier to separate them again upon H_2O intercalation, with a higher RH (higher H_2O activity) required. This has already been discussed in the clay literature.[24,173] Further, it is clear that the transition from 1W to 2W phases happens at different RH for the various cations. Ordering the cations by this transition correlates to increasing cation hydration enthalpy, which is understandable because cation hydration is at the heart of the phenomenon. These results were obtained after equilibration with the humid air had completed, so while the 1W/2W transition is observed, we still do not have enough information to determine whether it is a continuous or discontinuous transition. To answer this question, Li-$Ti_3C_2T_x$ was hydrated with liquid water to ensure the 2W phase and placed in a sample holder exposed to ambient atmosphere (~ 50 % RH). XRD was then recorded every 4 minutes while the sample dried. The results,

presented in Fig. 4.19, show that the transition is discontinuous, with no smooth shifting of the peaks; there is in fact a region around the 0.5 h mark where both phases exist simultaneously. This implies a process of pillaring - because there is a discontinuous jump in *c*-LP, it is most likely that H_2O is removed without change in MXene structure up until the point where there remain only a few pillars of hydrated cations that support the layers. Eventually, these collapse as H_2O from the pillars leaves, resulting in collapse of the structure down to 1W.

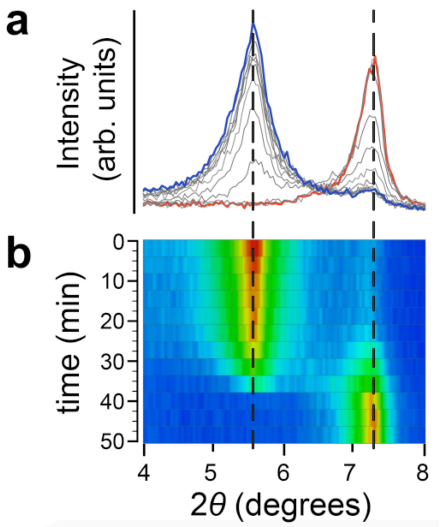

Figure 4.19: XRD data for Li-$Ti_3C_2T_x$ showing evolution over time as the sample is dried in 50 % RH atmosphere. a) Standard XRD patterns of basal region. b) 2D plots of the same data, showing diffraction intensity (red = most intense) as a function of time. Note the existence of only two fixed basal spacings, and the coexistence of the phases around the halfway point of ~ 0.5 h.

To get a better idea of what was happening as H_2O left the structure, and the effects of cation chemistry, TGA was performed on samples Li-$Ti_3C_2T_x$, K-$Ti_3C_2T_x$, Na-$Ti_3C_2T_x$, and Ca-$Ti_3C_2T_x$. The samples were first equilibrated in ambient atmosphere (~ 50 % RH, 25 ºC), and then heated stepwise to 120 ºC, with time for

equilibration at each temperature step. To be able to compare the TGA curves, we made the assumption that after 120 ºC, H_2O held by cations should be gone and any leftover H_2O would come from elsewhere in the interlayer, and in a relatively small amount, so all samples should have more or less the same mass fraction of MXene at close to 100 %; thus normalizing the mass fraction of all samples to 100 % as the final value allowed us to extrapolate the fraction of water that was lost at the beginning of the temperature ramps. This is shown in Fig. 4.20a. The completion of the first temperature step, at 27 ºC and under dry N_2 (~ 0 % RH), should roughly approximate the conditions after equilibration at 0 % RH in the XRD experiments (Fig. 4.19). It is clear that Ca-$Ti_3C_2T_x$ loses the largest amount of H_2O during this step, which is consistent with that material having the greatest change in basal spacing. It is also clear that the mass loss is continuous over the same range that the shift in basal spacing is discontinuous, as may be expected from a pillared system.

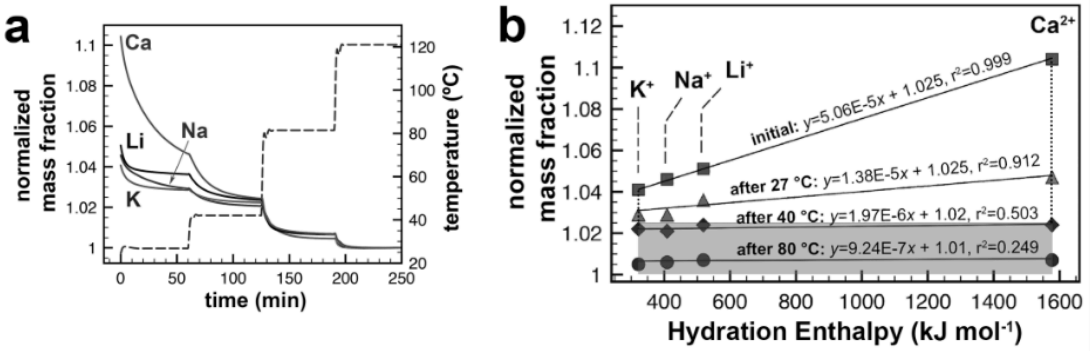

Figure 4.20: a) TGA analysis under dry nitrogen from 27 ºC to 120 ºC for samples Li-, K-, Na-, and Ca-$Ti_3C_2T_x$, stepwise. Dashed line is the temperature curve as a function of time (actual data). All samples have been assumed fully dried after 120 ºC and normalized to mass fraction = 1, so that initially, amounts above 1 represent intercalated water. b) Mass fraction > 1 for each sample at each temperature step, plotted against the hydration enthalpy of the intercalated cation. Shaded region represents H_2O loss that is likely not involved in cation hydration (e.g. as H_2O adsorbed to MXene surface groups).

At the completion of the first temperature step of the TGA, the different cation-intercalated MXenes have lost varying amounts of H_2O. One issue to address is whether the H_2O lost originates from the interlayer or from other areas such as inter-particle pores. The clay literature suggests that, given the equilibration at 50 % RH, most of the desorbable H_2O should originate from the interlayer space.[174] The normalized mass fraction lost after each temperature step is plotted against cation hydration enthalpy in Fig. 4.20b, starting at the initial mass fraction at time $t = 0$. The initial values make it clear that the H_2O lost is directly related to hydrated cations, as the relative amount present in the structure correlates linearly with cation hydration enthalpy. This correlation persists up to 40 ºC, after which all samples lose roughly the same amount of H_2O. This we deem to be H_2O that is more strongly adsorbed and not associated with cation hydration; it may be in the form of H_2O adsorbed to MXene surface groups.[56] Assuming that the final mass is nearly all from the MXene host structure, with an approximation of the molar mass of $Ti_3C_2T_x$ at 204 g mol^{-1} (for the formula Ti_3C_2OF; the mass of the intercalated cations can be included but was found to have nearly negligible impact on the results), the mass of H_2O and therefore the number of H_2O molecules per Ti_3C_2 unit can be calculated; the total mass of H_2O lost is split into parts that are dependent on the cations and that are inherent to the structure.[150] These results are shown in Table 4.1 and compare well with literature data for clay minerals.[175,176,177] Both the higher amounts of H_2O present for the divalent cations and the fact that H_2O persists after cation-bound H_2O has been removed are consistent with more recent studies.[100]

Table 4.1: H_2O per Ti_3C_2OF formula unit.

ion	*# ions per Ti_3C_2* [a]	*MW of MXene/ion complex (g mol^{-1})*	*# H_2O per Ti_3C_2 (non-ion-associated)* [b]	*# H_2O per Ti_3C_2 (ion-associated)* [c]
K^+	0	203.6	0.28	0.18
	0.3	210.5	0.29	0.18
Na^+	0	203.6	0.28	0.23
	0.3	215.4	0.29	0.25
Li^+	0	203.6	0.28	0.28
	0.3	205.7	0.29	0.29
Ca^{2+}	0	203.6	0.28	0.90
	0.15	209.6	0.29	0.92

[a] Endpoints 0 and 0.3 are chosen to bracket our results and show the minor effect of accounting for ions in the molecular weight
[b] Calculated from H_2O mass loss after ion-dependent region (see text for explanations)
[c] Calculated from initial ion-dependent H_2O mass (see text for explanations)

Bray and Redfern[178] demonstrated that an Avrami analysis could be applied to thermal data from Ca-montmorillonite, a clay mineral that is intercalated with Ca^{2+} and shows swelling, to investigate the kinetics and mechanism of H_2O diffusion in the material. The equation

$$\ln(-\ln(1-\alpha)) = m \ln k + m \ln t \qquad \text{(Equation 4.1)}$$

where t is in seconds and α is a parameter for the extent of reaction, from 0 to 1, can be used with TGA data. From linearization, the parameters k (a rate constant) and m (a value relating to mechanism) can be extracted. For dehydration at 20 and 30 ºC in dry N_2, Bray and Redfern found that their Ca-montmorillonite gave m values between 0.6 (associated with a 2D diffusion-controlled process) and 1.0 (a first-order process). Their interpretation was that of a first-order process that was slowed by diffusion in the interlayer space. For Li-$Ti_3C_2T_x$, K-$Ti_3C_2T_x$, Na-$Ti_3C_2T_x$, and Ca-$Ti_3C_2T_x$, we have calculated α at each time t using the initial value of mass percent as $\alpha = 0$ and the value of the mass percent near equilibrium, after exposure to dry N_2 atmosphere at 27 ºC, as $\alpha = 1$. Linearizations for our materials are plotted in Fig. 4.21a, with a

constrained range for α of 0.15 to 0.5. From these, we have extracted k and m according to the previous Avrami equation. These values are presented in Table 4.2, along with literature values from Bray and Redfern.[178] Looking at Ca-$Ti_3C_2T_x$, the values are quite similar to Ca-montmorillonite; it is reasonable to conclude that the same mechanics of H_2O loss are occurring in MXene.

The work in this section represents an important link between MXenes and clay minerals, and some justification for calling them 'conductive clays' – they have been conclusively demonstrated to undergo humidity-dependent crystalline swelling. Further, they can also be linked to the layered dichalcogenides, which have been shown to exhibit the same behavior when intercalated with similar cations.[179]

Table 4.2: Avrami analysis on $Ti_3C_2T_x$ and Ca-montmorillonite

sample	*Temperature (°C)*	*k*	*m*
K-$Ti_3C_2T_x$	27	0.0025	0.88
Na-$Ti_3C_2T_x$	27	0.0011	0.78
Li-$Ti_3C_2T_x$	27	0.0037	0.95
Ca-$Ti_3C_2T_x$	27	0.00097	0.80
Ca-montmorillonite[a]	20	0.0008	0.99
Ca-montmorillonite[a]	30	0.0033	0.86

[a] From Bray and Redfern[178]

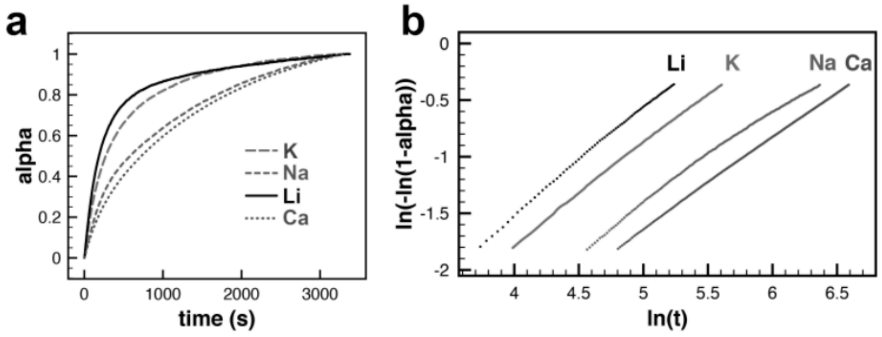

Figure 4.21: Avrami analysis for the initial temperature hold of 27 ºC for Li-, K-, Na-, and Ca-$Ti_3C_2T_x$. a) The parameter α, or extent of reaction, as a function of time. b) α data truncated between α = 0.15 to 0.5 and linearized according to Equation 4.1 to extract k and m values.

Pressure-Driven H_2O Intercalation

In some layered materials such as graphite oxide, clay minerals, and layered titanates,[180,181,182] it has been demonstrated that, somewhat counterintuitively, when compressive stress is applied, intercalants (primarily H_2O, but also small molecules *e.g.* alcohols) can be forced to intercalate, causing *expansion* of the basal spacing. Naturally, the overall volume of the system must still decrease as the pressure is increased. For the case of H_2O, there has been speculation that a pressure-induced dissociation of functional groups in the interlayer causes an osmotic gradient which draws the solvent in.[183] This explanation may be consistent with the demonstration of pressure-induced proton transfer in some materials.[184] The exact mechanisms have not been elucidated fully to date, though a simple view is that the solvent is simply able to adapt a higher-density configuration inside the interlayer.[185] Based on some of our early observations that cold-pressed discs of MXene showed higher basal spacing than the starting powders, we set out to see if the behavior would be similar

to other materials, and to determine what effects ion intercalation might have on the phenomenon.

In our initial trials, $Ti_3C_2T_x$ was produced by etching with HF10 alone (24 h, 25 ºC). After washing, the powders were allowed to equilibrate for 24 h in ambient atmosphere (~ 50 % RH) to make a source material that had uniform H_2O content. The MXene was then equilibrated at 0, 30, 55, 80, or 100 % RH, with humidity controlled by the saturated salt solution method.[146] The samples under atmosphere of lower than 50 % RH should then be expected to lose H_2O and those at higher than 50 % RH should gain it. After 3 days, the powders were collected and divided into two groups: the first was measured by XRD without further processing, and the second was pressed into free-standing discs at ~ 300 MPa, followed by XRD. These results are shown in Fig. 4.22a,b. The powders before pressing show very little order along the basal direction, with only some minor changes from humidity. However, upon pressing, a striking behavior emerges: the 0 % RH powders demonstrate the same basal spacing, but at a higher diffraction intensity (which is likely due to particle alignment effects at the surface of the disc),[2] while the 100 % RH powders show a basal spacing expansion to nearly 15 Å; intermediate humidities resulted in multiple phases present: 10 Å, 12.5 Å, or 15 Å. These spacings correspond to rough dimensions of H_2O molecules as discussed earlier.

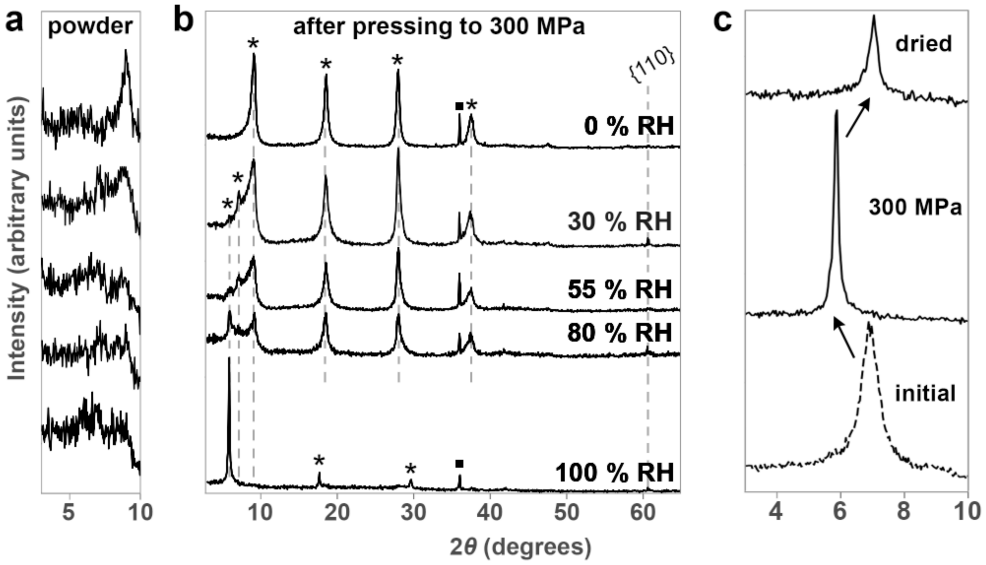

Figure 4.22: Humidity-dependent XRD of uniaxially-pressed MXene discs. XRD (CuK_α radiation) of $Ti_3C_2T_x$ equilibrated at various RHs. (a) Powders directly after equilibration (note that all reflections are (00*l*)). (b) Same powders, after uniaxial pressing to 300 MPa to form discs. Asterisks denote (00*l*) reflections, and squares denote (111) reflections from a small TiC impurity. (c) Initial wet paste directly after preparation (bottom), after pressing to 300 MPa to form a disc (middle), and after drying the disc over P_2O_5 for 48 h (top). All reflections are (00*l*).

To verify that the effect was caused by H_2O intercalation, we first took $Ti_3C_2T_x$ that was fresh from etching and washing (before being allowed to dry), which XRD showed to have a basal spacing of 12.5 Å (Fig. 4.22c, bottom trace). This verifies that even the presence of liquid water is not enough to spontaneously swell the material to the full 15 Å spacing, so that pressure is required to achieve the spacings we observe. Upon compressing the wet powders into a disc, the 15 Å spacing is observed (Fig. 4.22c, middle trace). When the disc was dried in an atmosphere of 0 % RH and measured again (Fig. 4.22c, top trace), the basal spacing subsequently decreased from 15 Å to 12.5 Å, or roughly the diameter of a H_2O molecule, as discussed earlier in this section. From these results H_2O intercalation and de-intercalation are clearly the cause of the changes in spacings.

Believing that the same behavior would be observed *in-situ* under high-pressure conditions in a Diamond Anvil Cell (DAC), as the literature suggested, we collaborated with Dr. Vadym Drozd from Florida International University. $Ti_3C_2T_x$ multilayers were first loaded into the DAC with enough water to wet the powders, which we believed was closer to the hydration conditions in the pressed-disc experiments. A pressurerization-depressurization cycle to 5 GPa, with *in-situ* monitoring of the basal spacing (Fig. 4.23b, triangles), showed only compression of the interlayer distance. The experiment was then repeated with excess H_2O as a pressure-transmitting medium (Fig. 4.23b, circles; diffraction patterns in Fig. 4.23a). This time, an *expansion* was indeed observed around 0.1-0.3 GPa, which is in the same range as the pressures applied in the pressed-disc experiments. After this expansion, the basal spacing was compressed, with about the same slope as that observed in the experiment with less H_2O. The initial expansion, however, was only to 12.8 Å, a change of +0.3 Å, which is far less than that observed in the pressed-disc experiments. Upon release of all stress in the DAC, the spacing increased further to 13.2 Å. A possible explanation is that H_2O is forced into the interlayer space at low pressures, causing an initial expansion, but the expansion is restricted by the applied pressure; once the pressure is released, the full expansion becomes apparent. This is still, however, almost 2 Å less than that observed from the discs.

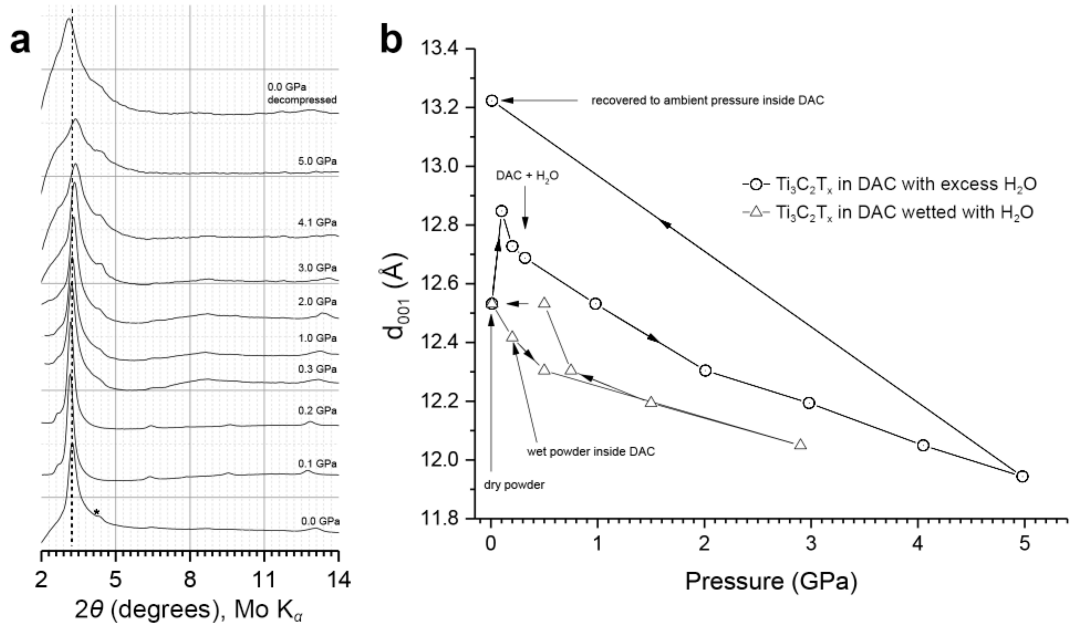

Figure 4.23: Pressure-dependent *in situ* X-ray diffraction. (a) XRD patterns (Mo K_α radiation) of $Ti_3C_2T_x$ collected in a DAC at various pressures up to ≈ 5 GPa using water as pressure transmitting medium (in other words, a large excess of water). The asterisk (*) denotes the (002) reflection of a small amount of residual Ti_3AlC_2. All other reflections are MXene {00*l*}. (b) Basal spacing as a function of external pressure for $Ti_3C_2T_x$ in two experiments with different amounts of water: excess H_2O (open circles) and a small amount of H_2O (open triangles). Note that the maximum expansion here is almost 2 Å *smaller* than those reported in Fig. 4.22.

We started to investigate the discrepancy between the *ex-* and *in situ* structural changes by looking more closely at the *ex-situ* pressed discs. The main difference between the two experimental setups is that the discs pressed in the steel die uniaxially will have strong interactions between MXene and the metal of the die components, leading to shear stresses from deviatoric components of the stress. Due to the limited penetration depth achievable with our diffractometer, we attempted to characterize the structure of the MXene in the internal parts of the discs where the deviatoric stresses should not be so high. We attempted this at various depths within the disc by using a blade to scrape off thin layers, followed by XRD of the disc. The

results of this are shown in Fig. 4.24. Discs pressed from 0 % RH powders (Fig. 4.24a) showed relatively high intensity reflections to a much deeper depth than those pressed from 100 % RH powders (Fig. 4.24b). The latter showed little structural order beyond the surface, confirming that whatever causes the large basal expansion, it seems to be primarily happening at the disc/die interface.

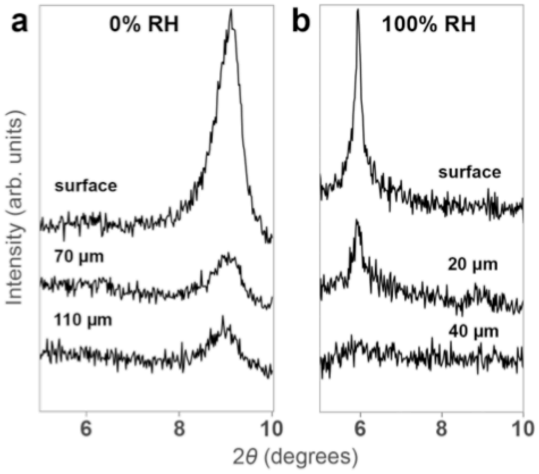

Figure 4.24: Depth-profile X-ray diffraction of pressed discs. XRD (Cu K_α radiation) of $Ti_3C_2T_x$ pressed into discs at 300 MPa. Powders were equilibrated at, (a) 0 % or, (b) 100 % RH before pressing. In each case, further XRD was taken after indicated approximate depths of material indicated on plot had been scraped from the surface to obtain an approximation of the depth profile. All reflections are (00*l*).

We then imaged the surfaces of various discs using SEM. At 100 % RH, the surface consists of highly sheared nanosheets that resemble a delaminated film (Fig. 4.25a). The interior of the disc consists of particles that have some degree of shear, but are still retained in multilayer stacks (Fig. 4.25b). At 0 % RH, the surface consists of mostly intact multilayer particles (Fig. 4.25d). At intermediate humidity, there are traces of both particles with low shear and areas of high shear (Fig. 4.25c).

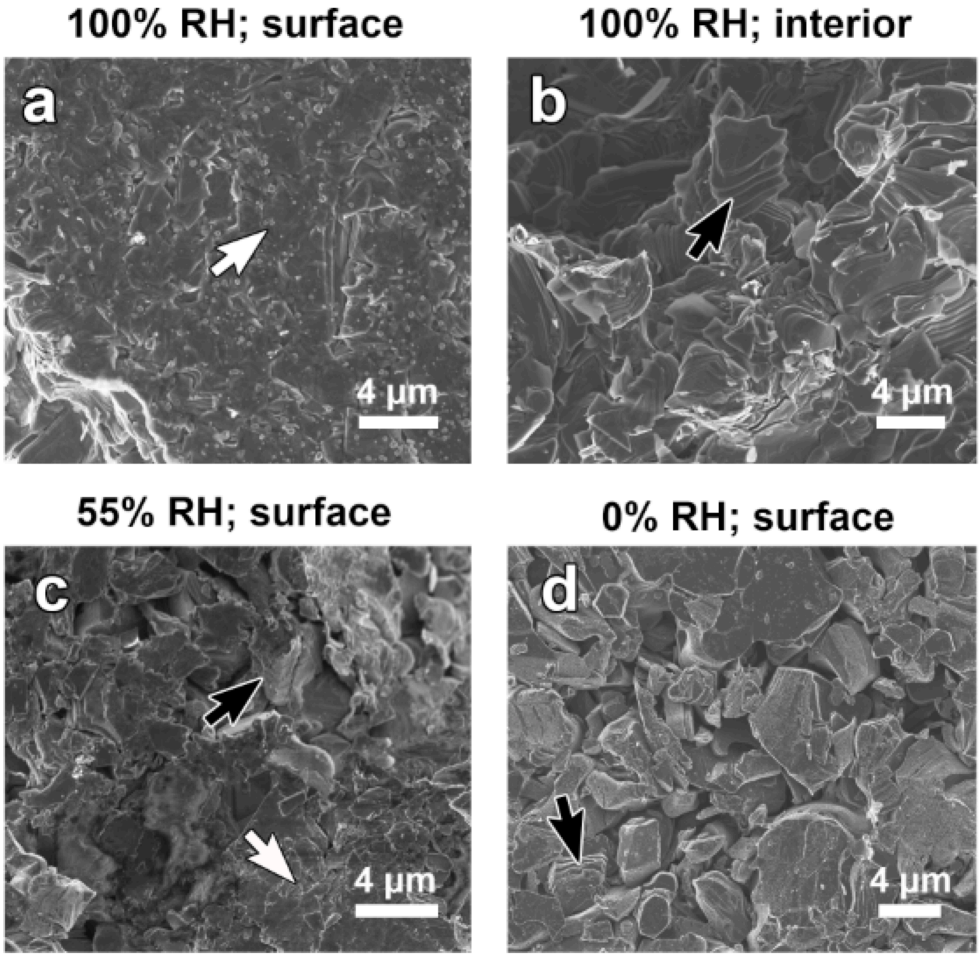

Figure 4.25: SEM images of various pressed discs made with powders that had been equilibrated, prior to pressing, at various labeled RHs. (a) and (b) are from the surface and interior, respectively, of the same disc at 100 % humidity. (c) and (d) are from the surfaces of discs at 55 % and 0 % RH, respectively. Examples of multilayer particles at various states of shear are labeled with black arrows; regions of extreme shear are labeled with white arrows.

Combining these insights with the humidity-controlled XRD data, it seems that there is a good correlation between shear of the multilayer particles and whether the basal spacing expands. This was given further support when MXene that was ejected along the inside seam of the die was collected and analyzed. This material would not have experienced the same kind of stress as the rest of the disc, but due to the small size of the seam, would have experienced high shear stresses. A diagram of

the die and location where the material was collected is shown in Fig. 4.26a. XRD of this material (Fig. 4.26b) showed that the material indeed expanded to 15 Å, and SEM confirmed that the nanosheets were highly sheared (Fig. 4.26c).

A shearing effect in clay minerals that experience pressure-induced basal expansion has been observed in DAC, but the authors did not show whether the shear was the cause of the expansion or simply correlated.[181] Work on zeolites shows that, while structurally different than our layered materials, pressure can induce changes in the structure of nanopores that allow for increased accessibility to H_2O (again, performed in a DAC), leading to entrance of the solvent into the structure.[186] Thus, while we do not have evidence for determination of a mechanism for the insertion of H_2O at high pressure into MXene, there are precedents for plausible explanations that may be explored later. It may be the case for MXene that after H_2O has entered the structure, lubricity is increased and the sheets are easier to slide apart. Recent results suggest that at least the mobility of water increases with an increase in basal spacing – when diffusion coefficients for interlayer water contained in K-$Ti_3C_2T_x$ and Mg-$Ti_3C_2T_x$ were compared, the former was measured at 4.2×10^{-12} m^2 s^{-1}, and 11.1×10^{-12} m^2 s^{-1} for the latter (compared to 6.9×10^{-12} m^2 s^{-1} for un-intercalated $Ti_3C_2T_x$).[100] The DAC results suggest, however, that this simple explanation is not so straightforward, as the magnitude of expansion from the *ex-situ* experiments was not replicated by the *in-situ* compression, which may have lacked the kind of shear stress component from a rough steel die interface. The fact that the expansion to 15 Å in the pressed discs persists for a long time, or requires desiccation to remove, may be explained by the high degree of shearing shown in Fig. 4.25a; the turbostratic

arrangement of flakes may create more tortuous diffusion paths, leading to a higher energy barrier to diffusion of H_2O.[120]

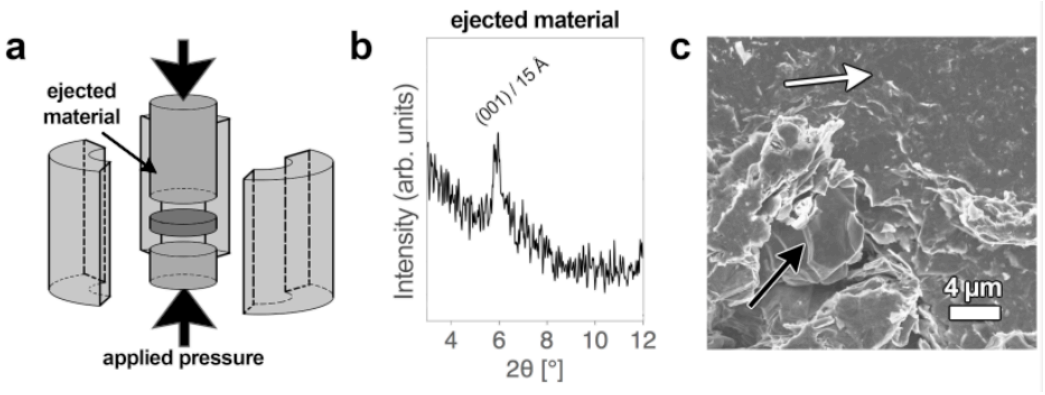

Figure 4.26: Analysis of material ejected from the side of the die. (a) Schematic showing the setup of disc pressing in a steel die with 3-part walls. The large arrows indicate the direction of the uniaxial pressure, and the small arrow shows the location of MXene collected that was ejected from the main pressing area and up along the inside of the die walls. The MXene disc is shown in dark grey at the center. (b) XRD of the same material, showing the same expansion as observed on the surface of the disc. (c) SEM image of the collected material, showing large areas with nanosheets that have slipped relative to each other into a turbostratically-disordered surface (white arrow) and particles with only minor shear (black arrow).

It has been observed that the presence of ions in MXene, specifically K^+, can reduce the mobility of H_2O in the interlayer and cause MXene sheets to be difficult to move in relation to one another.[99] In order to test whether this would have an effect on the pressure behavior, the humidity-controlled *ex-situ* XRD experiments were replicated with K-$Ti_3C_2T_x$. This was produced *via* alkali ion exchange protocol described earlier in this section. From Fig. 4.18 it is known that K-$Ti_3C_2T_x$ has very little structural response to humidity changes; thus there was essentially no difference between the un-pressed powders after humidity equilibration. Upon pressing, there was essentially no change in the basal spacing (Fig. 4.27a). SEM was again

performed, showing that even under 100 % RH conditions, pressing K-$Ti_3C_2T_x$ powders resulted in a disc surface composed almost entirely of undisturbed multilayer particles (Fig. 4.27b).

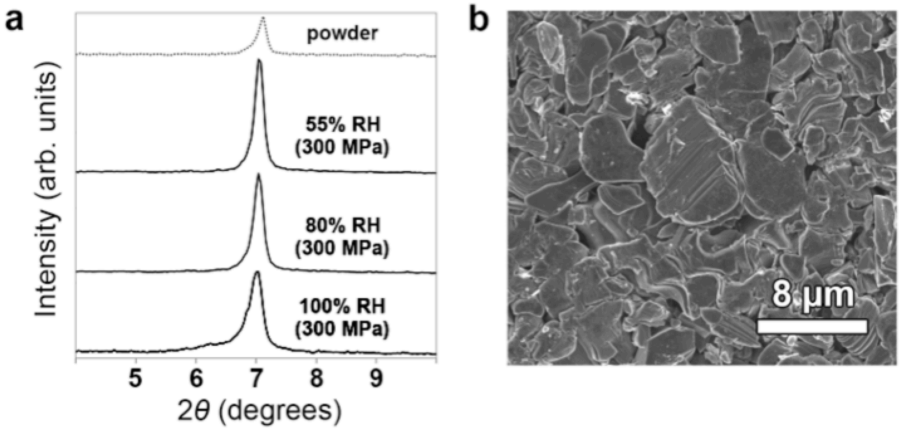

Figure 4.27: Humidity-dependent *ex situ* X-ray diffraction after K^+ intercalation. Effect of K^+ ions intercalated into $Ti_3C_2T_x$. (a) XRD of $Ti_3C_2T_x$ discs pressed at 300 MPa from powders that were equilibrated at various relative humidities. All reflections are MXene (00*l*). (b) SEM micrograph of the top surface of the 100% RH disc, showing no evidence of major nanosheet slipping.

The fact that, under the same 100 % humidity conditions and following pressing, the basal spacing of $Ti_3C_2T_x$ expands to 15 Å while that of K-$Ti_3C_2T_x$ does not change from its initial 12.5 Å, coupled with the fact that no shear is observed in SEM, both add weight to the idea of K^+ 'gluing' the MXene sheets together and give support to the idea that shear may be a causal effect in the expansion.

While $Ti_3C_2T_x$ etched with HF10 alone typically yields a maximum basal spacing of 12.5-13.5 Å, when it is delaminated and restacked into films in the presence of H_2O it can demonstrate a basal spacing of 15 Å,[115] the same observed in our work. Using the same pressing methodology as described earlier, some trials with

$Ti_3C_2T_x$ produced by HCl+LiF showed 10 Å basal spacing after pressing. Other production techniques such as spray-coating (involving delaminated nanosheets) gave values of 14.75 Å, and thick films produced by filtering nanosheet suspensions produced by HCl+LiF showed the same value before the films were dried. Finally, reports on single nanosheets of $Ti_3C_2T_x$ with a layer of H_2O molecules between the nanosheet and substrate had a height of 15±2 Å as measured by atomic-force microscopy. These collected values are summarized, with references, in Table 4.3. The common thread between these is that all the systems involve nanosheets that have their basal surfaces directly exposed to H_2O, allowing a layer to adsorb. If the nanosheets are restacked and each surface has a layer of H_2O, then a bilayer of H_2O is trapped in the restacked structure. Going back to the idea of shear in the $Ti_3C_2T_x$ systems, it might stand to reason that shear in the presence of water while the discs are being pressed exposes the basal planes of $Ti_3C_2T_x$ to H_2O, allowing for a full hydration.

On a practical note, the conductivity of MXene powders is often measured by pressing the powders into freestanding discs followed by four-point probe measurements on the surface. The results here show that if the humidity is not carefully controlled during the pressing, the surface morphology could be very different between samples, which may lead to inconsistencies in the conductivity of the material. The conductivity would also be a function of the sample thicknesses. It is for thus better to work with filtered or spin-cast films.[8]

Overall, we have established two potential mechanisms for insertion of H_2O under pressure in $Ti_3C_2T_x$: first, from the *in situ* DAC results, it is clear that quasi-

isostatic stress in H_2O medium can indeed lead to higher basal spacings. This is similar to other materials in the literature, and could arise from a number of reasons, but the most likely seems to be pressure-induced dissociation of proton-containing surface groups. Second, a simple model of shearing of nanosheets in the presence of H_2O may lead to exposure of basal surfaces to hydration, and the process of H_2O intercalation may have a feedback effect of increased lubricity, allowing more facile nanosheet slipping. For this second model it is important to note that there are two factors: a kinetic and a thermodynamic. The role of shear stress may simply affect the kinetic barrier, allowing the system to achieve equilibrium. For example, if, as our results strongly indicate, one assumes that the lowest energy state for K-$Ti_3C_2T_x$ is one water layer, and that this configuration is present from the start, then no amount of shear should change the interlayer spacing, as observed. If the basal surfaces prefer to each be hydrated by a monolayer of water but are kinetically blocked from doing so, shearing them may reduce the kinetic barriers.

Table 4.3: Comparison of basal spacings of $Ti_3C_2T_x$ made by different methods

Etching System	*Processing*	*basal spacing (Å)*	*Δd (Å)* [d]	*Ref.*
10 % HF	Undisturbed multilayer stacks, dry	~ 10 [a]	0	[2,5]
10 % HF	Undisturbed multilayer stacks, still wet	13.5 [a]	3.5	[115]
10 % HF	Delaminated and restacked	15.1 [a]	5.1	[115]
HCl + LiF	Disc (pressed at 300 MPa)	15.0 [b]	5	[79]
HCl + LiF	Spray-coated film (from delaminated suspension)	14.75 [a]	4.75	[84]
HCl + LiF	Thick film *via* filtration of delaminated suspension	15.2 [a]	5.2	[120]
HCl + LiF	Spincoating (single- to few-layer flakes)	15±2 [c]	5	[187]
10 % HF	Disc (pressed at 300 MPa)	15	5	this work

[a] From reported $d_{(002)}/2$.
[b] Pressed-disc data from the same study, but not published in the accompanying reference.
[c] Monolayer with H_2O *via* atomic-force microscopy.
[d] Measured as expansion from fully-collapsed dry structure with d = 10 Å.

To get an idea of how MXene compares to other materials in the magnitude of pressure-induced expansion, we have collected a number of values in Table 4.4. Note that Δd can be defined either as an expansion from the totally collapsed structure or continued expansion from an already-hydrated phase. We have included both in the table for clarity. Based on this survey, it is clear that other materials exhibit expansion both on the same order as MXene, and also that the expansion often occurs on the order of multiples of the approximate diameter of the H_2O molecule.

Table 4.4: Basal spacings of select pressure-expanded materials from the literature

Material	*Δd (Å)*	*Pressure (GPa)*	*Ref*
$Ti_3C_2T_x$	2.5 [a] / 5 [b]	0.3 (uniaxial, *ex-situ*) [c]	This work
	0.16 [a] /2.66 [b]	0.32 (quasi-hydrostatic) [d]	
	0.69 [a] / 3.19 [b]	after unloading from 4.98 (quasi-hydrostatic)	
Na-fluorohectorite (a clay mineral)	2 [a]	2.5 (hydostatic) [d]	188
Kaolinite	1.5 [a] / 2.4 [b]	0.1 (hydrostatic, over 65 h) [d]	15
Graphite oxide (GO)	2.5 [a] / 6.9 [b]	1.25 (hydrostatic) [d]	180

[a] Δd defined as difference between the phase after pressure is applied and highest d spacing observed from ambient-pressure hydration.
[b] Δd defined as difference between pressure-hydrated phase and dried, fully-collapsed structure.
[c] Maximum pressure applied (*ex-situ* experiments)
[d] Pressure at which the expansion was observed to occur

Section Summary

We have developed robust protocols for reliably intercalating alkali and alkaline earth metal cations into $Ti_3C_2T_x$. We have begun to characterize the intercalated complexes in terms of the relative amounts of cations present and the thermal properties of H_2O adsorbed in the interlayers. Further, we have fully explored the effects of humidity (reversible H_2O intercalation) on the structure of these materials. Finally, we have discovered a shear-induced basal spacing expansion in $Ti_3C_2T_x$, which can be suppressed by K^+ intercalation. The phenomenon is not only interesting for the field of MXenes, as it may have great importance to applications where rolling or shaping of multilayer MXene is needed, but the addition of a new material to those that show this behavior allows a new opportunity to gain better understanding of this general phenomenon. Overall, alkali and alkaline earth cations show great promise in providing the researcher tools to tailor many desired properties of MXene.

Future Work

First and foremost, the cations explored in this section, while offering exciting new properties and understanding, are limited in scope. There are many other potential elements that could be intercalated to offer new properties. Importantly, nearly all understanding in this project is generated for the MXene $Ti_3C_2T_x$. While this is a good start, there are many other MXene compositions with exciting properties that need to be thoroughly investigated for cation intercalation. Some studies have begun in our research group into the intercalation of similar cations into select other MXene compositions (e.g. Ti_2CT_x and Nb_2CT_x), but these studies are reserved for future work.

4.2.2: Ion Exchange: Transition Metals

After a better understanding of simple mono- and divalent cation intercalation was developed, we sought to develop intercalation protocols for transition metal cations. The transition metals have precedent in other layered material literature, and understanding their intercalation chemistry is important both for control of the chemistry of the intercalated complex (many of these cations can hold multiple charges and may be a way to endow MXene with magnetic properties) and for environmental applications, such as heavy metal sequestration (they have already been demonstrated to interact with heavy metals such as chromium,[115] lead,[62] and mercury[116]). As an alternate route to these goals, there has been work to produce nanocomposites of transition and other heavy metals with MXenes, such as with iron

oxide,[118] noble metals such as Ag, Au, and Pd,[189] and even f-block metals such as U.[190] This work was kept brief due to higher priority of other studies.

The general protocol was the same as for alkali cations, namely using solutions of chloride salts to replace Li^+ in Li-$Ti_3C_2T_x$. We investigated the divalent cations Fe^{2+}, Co^{2+}, Mn^{2+}, and Ni^{2+}. Diffraction data (Fig. 4.28) shows basal spacings of 14.8–15.5 Å, which are comparable to data from the divalent alkaline earth cations Mg^{2+} and Ca^{2+}, suggesting similar hydration effects. EDS analysis (Table 4.5) of Co(II)-$Ti_3C_2T_x$, Mn(II)-$Ti_3C_2T_x$, and Ni(II)-$Ti_3C_2T_x$ suggests that an approximation for the number of cations present per Ti_3C_2 unit is between 0.06 and 0.09, which compare favorably with the values of 0.1-0.3 for alkali-intercalated $Ti_3C_2T_x$ from Section 4.2.1 (the numbers of intercalated transition metal cations must be halved for comparison to alkali metals due to the difference in charge). The chemical intercalations were performed by Matthias Agne (Drexel University).

Table 4.5: EDS analysis of $Ti_3C_2T_x$ intercalated with divalent transition metal cations

	Atoms per Ti_3C_2 unit		
Element	*Co(II)-intercalated*	*Mn(II)-intercalated*	*Ni(II)-intercalated*
C	1.97	1.92	2.16
O	1.87	1.74	1.92
F	1.37	1.34	1.64
Al	0.09	0.11	0.11
Cl	0.03	0.04	0.04
Ti	3.00	3.00	3.00
M^{2+} cation	**0.09**	**0.09**	**0.06**

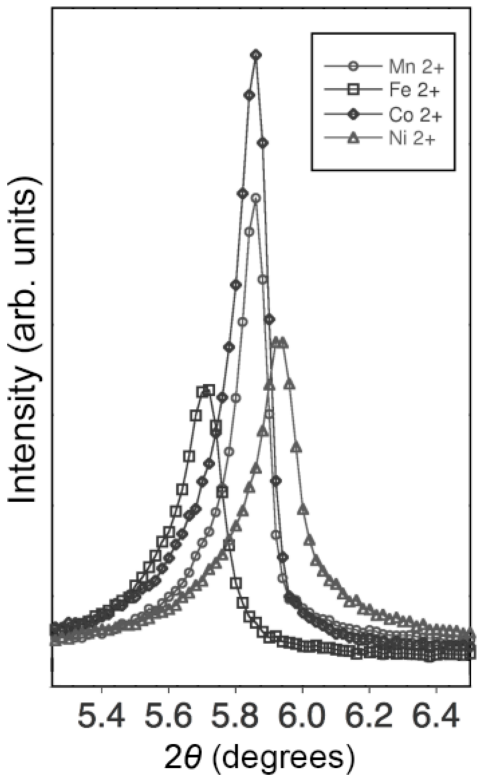

Figure 4.28: Powder XRD of the basal region for Li-$Ti_3C_2T_x$ that has been ion-exchanged with Mn^{2+}, Fe^{2+}, Co^{2+}, and Ni^{2+}.

Section Summary

We have demonstrated the applicability of ion-exchange protocols developed in the previous section for a greater diversity of cations here in the form of transition metals. Of note are that structural changes (suggesting similar hydration phenomena) and amounts of intercalated cations are comparable to alkali and alkaline earth intercalants. We leave exploring the properties of transition metal-MXene complexes for future study.

Future Work

The limited number of transition metal cations investigated here have only been shown to intercalate. With broadening of transition metal (and beyond) intercalation protocols and deep investigation into the resulting MXene properties, we may see some very interesting results in aspects such as electrical or magnetic properties.

4.2.3: Ion Exchange: Alkylammonium Cations

In order to round out our study of cation exchange, we turned finally to trimethylalkylammonium cations, which are widely used in the literature for layered materials such as clay minerals,[12] layered titanates,[191] dichalcogenides,[39] and others. These cations have a positive charge, so that they are exchangeable, and organic functionalities which can be tailored easily to a large amount of structures and functionalities. They have been used, for example, to hydrophobize interlayer spaces,[12,192] help in gas adsorption and retention,[193] cause large-scale and tuned swelling,[11] and even to synthesize nanomaterials.[194] The general form for trimethylalkylammonium cations is shown in Fig. 4.29a; the specific structures we have chosen to work with are shown in Fig. 4.29b. The charged N-containing head stays the same while the length of the alkyl tail is varied. Nomenclature has been chosen as C_1 (a tail of $-CH_3$) through C_{16} (a tail of $-(CH_2)_{15}CH_3$), with the variable n_c denoting the number of carbon atoms in the tail. In almost all cases in the following experiments, the bromide salt of the cation is used; C_{14} is the exception and was a chloride salt due to commercial availability. We found no difference in performance between the two types of salts.

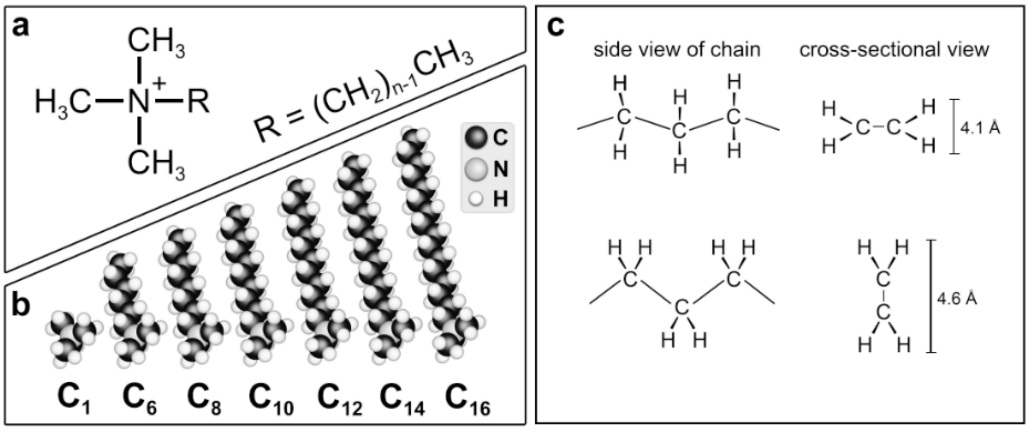

Figure 4.29: Structure of alkylammonium (AA) cations. a) General structure. b) Space-filling models of AA cations used in this study. c) Depending how the cation alkyl chain sits in the interlayer, the approximate cross-sectional height is 4.1 Å if the chain sits flat (top) and 4.6 Å if the chain sits on its side (bottom).[195]

In our first set of experiments, as before, Li-$Ti_3C_2T_x$ was produced. In this case it was dried in ambient atmosphere after it was made (~ 50 % RH) before intercalation. Fig. 4.30a shows the results of intercalation with 1 M solutions of the salts of C_6, C_8, and C_{12} for 24 h at 25 ºC. Despite the difference in chain length, all $Ti_3C_2T_x$ samples have the same basal spacing of 14.6 Å. The reason for this is that the cations likely sit flat in the interlayer space; in this configuration, they will all have roughly the same cross-sectional height of roughly 4.1–4.6 Å (Fig. 4.29c).[195] In the next experiment, the intercalation process was carried out at 55 ºC instead of 25 ºC (Fig. 4.30b). Here we did see the basal spacing begin to be a function of the cation chain length, with the peak showing corresponding to 18.8 Å; however, the C_{12} material is not phase-pure. The final panel, Fig 4.30c, shows the result when the MXene was not allowed to dry first; here, even with ion-exchange at 25 ºC, a single-phase material is finally observed for C_{12}. The evidence suggests that if Li-$Ti_3C_2T_x$ is

allowed to dry in ambient atmosphere before ion exchange, while some entry of cations can occur (according to Fig. 4.30a), there is an energy barrier that must be overcome with higher temperature. These problems do not arise when Li-$Ti_3C_2T_x$ is used as a starting material but is not allowed to dry first (the Li-$Ti_3C_2T_x$ used in Sections 4.2.1 and 4.2.2 was not dried prior to ion exchange). Our recommendations for ion exchange are to avoid pre-exchange drying of the MXene.

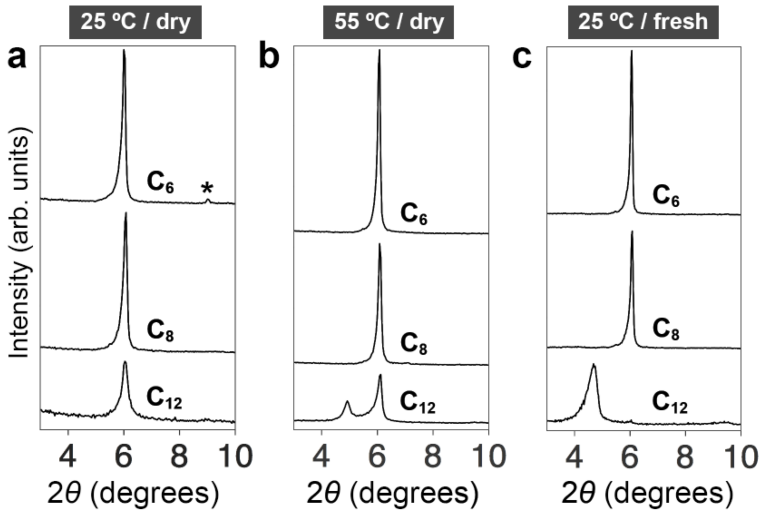

Figure 4.30: Powder XRD patterns of the basal region of Li-$Ti_3C_2T_x$ that has been exchanged with cations C_6, C_8, and C_{12}. a) Exchange performed on pre-dried MXene powders at 25 ºC. b) The same as (a) but at 55 ºC. c) Exchange performed on MXene powders that had never been dried after washing, at 25 ºC. Asterisks denote the {002} reflection of residual unreacted Ti_3AlC_2.

Based on this initial success, we prepared a series of $Ti_3C_2T_x$ intercalated with alkylammonium cations C_1, C_6, C_8, C_{10}, C_{12}, and C_{16}. Their XRD patterns are shown in Fig. 4.31a, with the corresponding Δd values at right of figure. Clearly, the basal spacing is independent of chain length until C_{10}-C_{12}, when the spacing begins to increase dramatically. Samples C_1–C_8 show roughly the same basal spacing, with a transition beginning at C_{10}, a higher expansion at C_{12}, and a huge expansion at C_{16}.

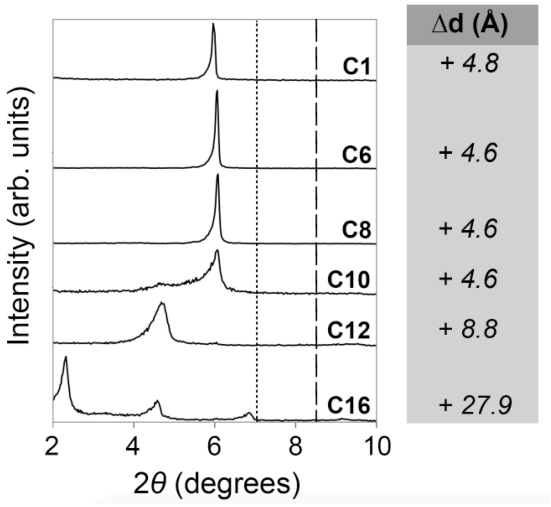

Figure 4.31: XRD patterns of the basal region of Li-$Ti_3C_2T_x$ exchanged with cations C_1–C_{16}. The increase in basal spacing (per interlayer) is shown at right.

From the series of intercalated $Ti_3C_2T_x$ in Fig. 4.31, samples C_1 and C_{16}, selected as endpoints, show that the intercalation of AA cations does not result in the kind of dynamic response to H_2O as was observed for alkali cations (Fig. 4.32a). Even after drying at 0 % RH, neither sample shows changes to the interlayer spacing. This is proof that the interlayer spacings discussed in Fig. 4.30 result solely from the AA cations and are independent of humidity conditions. Further, SEM images in Fig. 4.32b show that intercalation of AA cations preserves the multilayer stacked morphology, even for lattice expansions of nearly 28 Å. This expansion is somewhat in agreement with the crystallographic length of the C_{16} cation,[196] though from out current data it is not possible to ascertain whether the chains stand upright or not. Reports in the literature note that there are many conformations available to intercalants containing long alkyl chains.[197] Interestingly, from SEM images (Fig. 4.33), it appears that even up to the high lattice expansion of 28 Å, the multilayer stacked morphology is preserved.

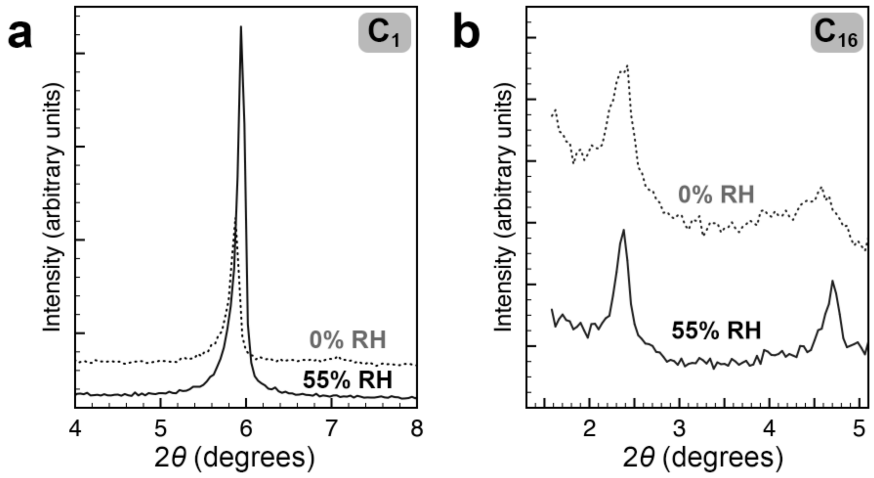

Figure 4.32: XRD patterns of the basal region at ambient atmosphere (solid trace; 55 % RH) and after drying at 0 % RH (dotted trace) for Li-$Ti_3C_2T_x$ exchanged with cations a) C_1 and b) C_{16}.

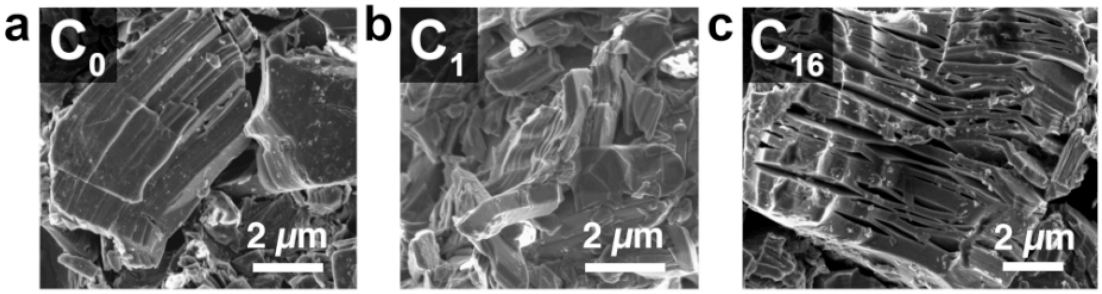

Figure 4.33: SEM images of a) $Ti_3C_2T_x$ (no intercalant) and Li-$Ti_3C_2T_x$ exchanged with AA cations b) C_1 and c) C_{16}, showing preservation of stacked, multilayer morphology.

The explanation for the curious structural behavior in Fig. 4.30 (namely the fact that the basal spacing remains constant from C_1 to C_8 and begins to change around C_{10}) has been explored in other materials - we will focus specifically on clay minerals, studied by Lagaly and Weiss.[198] In that work, intercalated silicates of the mica type are taken to have a fixed amount of negative charge per formula unit, f.u., which is counterbalanced by AA cations (the same way as in MXene). The minimum layer separation is taken to be approximately the cross-sectional height of an AA

cation (Fig. 4.29c). Thus, a minimum volume of the interlayer space per f.u. can be calculated using the host's lattice parameters and the cation height. Given a fixed charge density in this space (and therefore a fixed number of cation sites), there is a simple argument that the cation chain length is free to increase (illustrated schematically in Fig. 4.34a) up until the point when the volume is filled (Fig. 4.34b). At this point, in order to accommodate the increasing volume of the cations, the host layers must move farther apart (Fig. 4.34c); the length of the cation chains at this point is called the critical chain length or *critical* n_c. From this model it is expected that the layer separation should be independent of chain length (sitting at the minimum separation defined by the cation cross-sectional height) until critical n_c is reached, at which point the separation will be affected by the chain length. It follows that intercalating cations with increasing chain length and observing the critical n_c should allow one to work backwards and calculate the charge density per f.u. This is exactly the number of cations per f.u., assuming complete ion exchange. This process is discussed in great detail (though the reader may find it helpful to have a working knowledge of German) in the work of Lagaly *et al*.[195,198] The concern of whether it is realistic to assume a fixed charge density in the material depends on how the material holds its charge; for the case of clay minerals and layered double hydroxides, a fixed charge density is inherent to the material due to the permanent replacement of ions in the host structure, while in MoS_2 it may depend on the conditions of the initial alkali intercalation,[38] though this is a finer point.

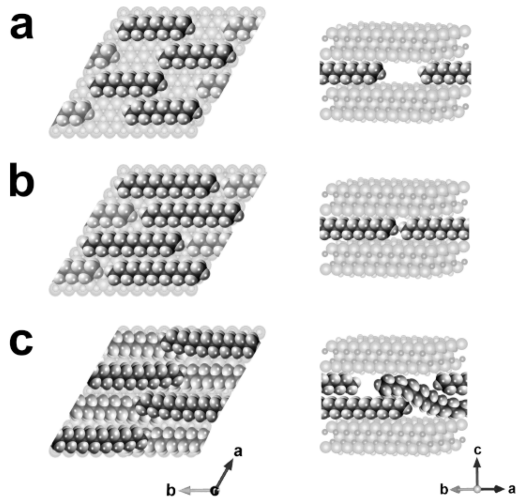

Figure 4.34: Schematics of volume filling by cations, of a fixed number per formula unit, in a layered material as cation chain length increases, with top views (left) and side views (right). a) The interlayer contains free space until the cation chain lengths increase to the point where, b) they fill the volume completely. c) As chain length continues to increase, the interlayer separation increases to accommodate the cations.

The volume filling argument requires that some nuances be understood before it is applied to MXene. It is somewhat complicated by MXene's surface terminations, as variances in surface termination size (*e.g.* between F and Cl)[57] distribution (whether random or partially ordered), or completeness of coverage may make the free volume difficult to determine. We have chosen to simplify our analysis by making the assumption that the MXene is covered by uniform, level planes of surface terminations. This is not completely realistic but approximates the volume decently. Further, the available volume of the unit cell is most simply calculated by assuming that $Ti_3C_2T_x$ at a basal spacing of 10 Å is fully collapsed, and observed Δd values represent the full height of the free interlayer space. However, if there already existed a separation, *s,* in the collapsed structure, this additional distance may need to be taken into account (see Fig. 4.35). We have run our analysis both with, and without,

this additional height *s* (where *s* is determined from the literature)[68] - "Model 1" uses the simple expansion Δd, and "Model 2" uses the expansion $\Delta d + s$.

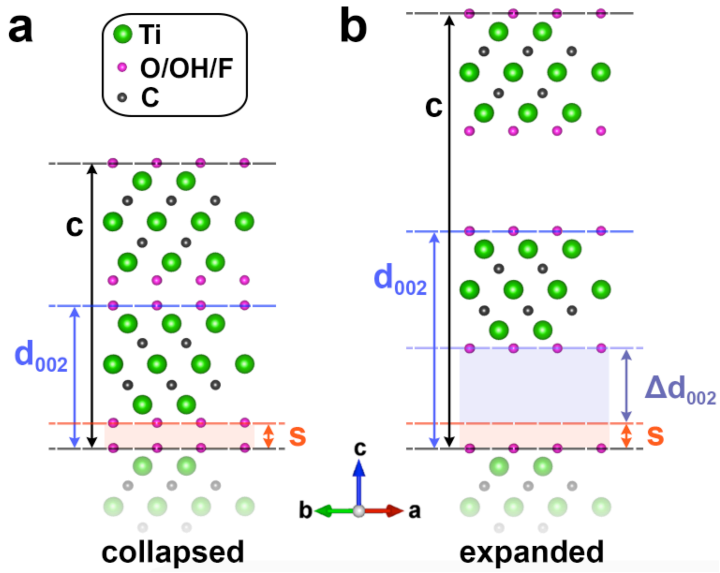

Figure 4.35: Idealized structure of $Ti_3C_2T_x$, showing a) collapsed and b) expanded structures. Interlayer separation can be taken either as exclusive (Δd only) or inclusive (Δd + *s*) of some level of separation, *s*, that may exist in collapsed structure (i.e. it may not be fully collapsed).

In order to perform the volume-packing analysis, we need to know the volume of the MXene interlayer space and the volume that each cation occupies.

Interlayer Volume:

The interlayer volume is simply area multiplied by height. The area occupied per Ti_3C_2 f.u. can be calculated from the unit cell parameter *a* as:

$$A_{occpied} = 2 \times ((3)/4)1/2 \times a^2 \qquad \text{(Equation 4.2)}$$

The interlayer separation is either inclusive or exclusive of the additional height *s* (encapsulated in general height *h*). The volume of the interlayer is found by multiplying $A_{occupied}$ by *h*:

$$V_{interlayer} = h \times (3)^{1/2}/2 \times a^2 \qquad \text{(Equation 4.3)}$$

Cation Volume:

Because we are looking for the volume of a cation and not the salt, we look to *N,N*-diimethylalkylamines, which are commercially available, and are similar to our cations (with the exception of the lack of one methyl group), and have known densities. From these data (obtained from Sigma Aldrich), the molar, and hence approximate molecular, volume can be easily calculated according to:

$$V\,[\text{per molecule, Å}^3] \approx 1\text{x}10^{24}\ \text{MW}\ (N_A\,\rho)^{-1} \qquad \text{(Equation 4.4)}$$

The molecular volumes were tabulated based on chain length and subjected to linear regression, and the line of best fit ($r^2 = 0.999$) was

$$V\,[\text{per molecule, Å}^3] \approx 27.17\ n_c + 123.99 \qquad \text{(Equation 4.5)}$$

Finally, because the cations have a fractional occupancy of the structure (from previous sections, the number of cations per Ti_3C_2 was of the order of 0.1-0.3), we have a correction factor of ξ for the cation volume, giving the formula of $[AA]_{\xi}Ti_3C_2T_x$.

The interlayer space is completely filled when:

$$V_{interlayer} = V_{cation}\ \text{x}\ \xi \qquad \text{(Equation 4.6)}$$

Combining Equations 4.3 and 4.5 into Equation 4.6, we can solve for ξ to find the cation number per Ti_3C_2 as a function of the chain length n_c:

$$\xi = h \times (3)^{1/2}/2 \times a^2/(27.17 \times n_c + 123.99) \qquad \text{(Equation 4.7)}$$

As noted earlier, these are approximate cation volumes due to the lack of one methyl group, but we have found that approximating the addition of this group to the volume had negligible effect on the results. Experimentally from Fig. 4.31, our critical n_c falls between 10 (the onset of structural expansion) and 12 (completed expansion). Using these values with Equation 4.7, we find ξ to be 0.09-0.1 for Model 1 and 0.13-0.15 for Model 2. We note that early reports of this method used area covered on the basal planes and the projected area of AA cations,[198] but we find the volume-filling approach to be more intuitive.

In looking to substantiate our simple modeling with advanced methods, we worked with Dr. Vadym Mochalin, who was able to create three groups of models using density functional theory (DFT) and molecular dynamics (MD). These models corresponded to the cation-intercalated samples C_1, C_6, and C_{10}. From earlier in the discussion, there are two factors that may cause the interlayer volume to fill; one is a fixed number of cations but increase in chain length; the other is an increasing number of cations, given a fixed chain length. For this modeling we assume the latter. Beginning with C_{10} (our experimental critical n_c), a unit cell of $Ti_3C_2(OH)_2$ was packed with cations and the basal spacing was determined at various values of ξ. Plotting the expansion against ξ (Fig. 4.36a), it is clear that there is are three distinct regions: Region i with a smaller slope, a transition at Region ii, and Region iii, with a larger slope. The discontinuity in expansion becomes clear from Fig. 4.36b, where the molecular dynamics snapshots seem to show a quasi-bilayer of cations forming. This is confirmed by the profile of nitrogen concentration along the *c* direction of the unit cell (Fig. 4.36c); while Region i shows a sharp profile, Region ii causes broadening,

and Region iii clearly shows that there are two distinct distributions of nitrogen, or in other words, that they are no longer contained in a single plane. The transition, Region ii, was taken as the critical ξ, with a value of 0.123. We note that this is quite close to the results from our simple model. The calculations were repeated for C_1 and C_6 (the same types of data are shown in Fig. 4.37), yielding critical ξ values of 0.333 and 0.210, respectively.

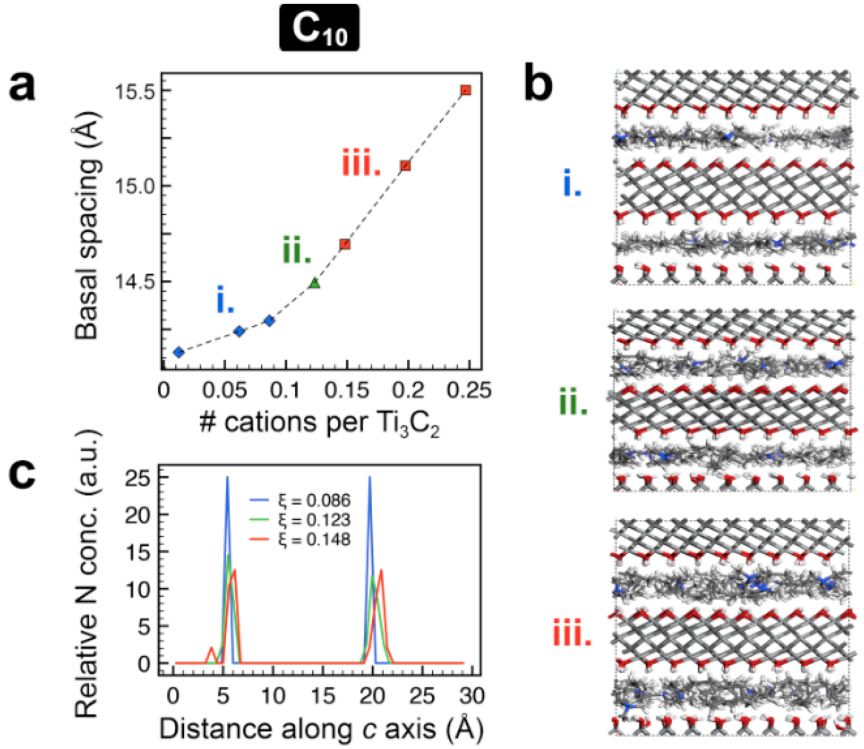

Figure 4.36: DFT / MD results for $Ti_3C_2T_x$ intercalated with C_{10} cations. a) Calculated basal spacing as a function of number of cations per Ti_3C_2 formula unit. Regions marked denote cation packing in (i) quasi-monolayer, (ii) transition region, and (iii) quasi-bilayer. b) MD snapshots of the regions i-iii from (a). c) Profile of relative nitrogen concentration along *c* axis for a value of ξ in each region i-iii. Sharp single peaks at a given distance represent uniform distribution of cations in a plane (monolayer); broadened or multiple peaks at a given distance represent disruption of that plane.

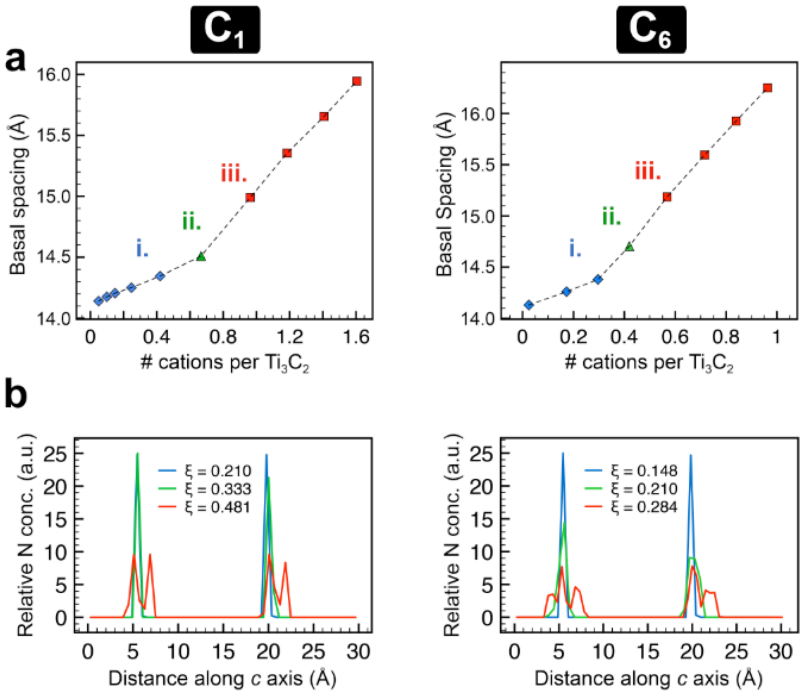

Figure 4.37: DFT / MD results for $Ti_3C_2T_x$ intercalated with C_1 and C_6 cations. a) Calculated basal spacing as a function of number of cations per Ti_3C_2 formula unit. Regions marked denote cation packing in (i) quasi-monolayer, (ii) transition region, and (iii) quasi-bilayer. b) Profile of the relative nitrogen concentration along the *c* axis for a value of ξ in each region i-iii. Sharp single peaks represent uniform distribution of cations in a plane (monolayer); broadened or multiple peaks at a given distance represent disruption of that plane (e.g. a bilayer).

These results fit into the bigger picture when Model 1 and Model 2 are plotted as expected critical n_c as a function of ξ, in Fig. 4.38. When the pairs of n_c, and ξ from the computational study are plotted here, even though they were derived by approaching the system as having a critical ξ rather than using a critical n_c, they fall nicely between the ranges from our simple models. Finally, the combination of these models explain the existence of multiple phases of C_{12}-$Ti_3C_2T_x$ from Fig. 4.30. Due to the energy barrier of cation insertion likely present in the pre-dried MXene, the number of exchanged AA cations would be less than the cation capacity of the MXene, and thus would shift ξ to lower values, in the cation monolayer region.

Higher temperatures of exchange for the dried MXene, and finally using non-dried MXene, allow for full cation exchange.

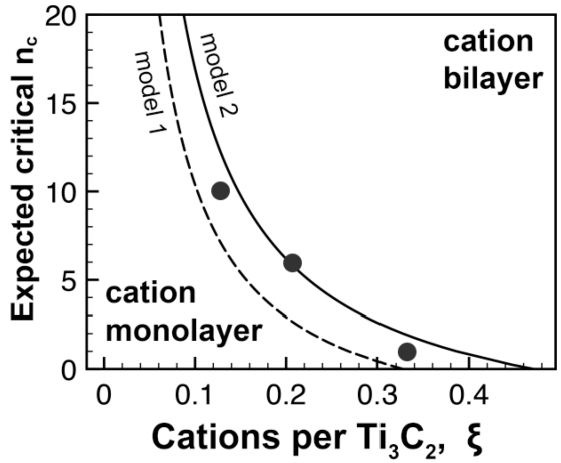

Figure 4.38: Plot of Equation 4.7 for Models 1 and 2. This is essentially a phase diagram - given the conditions of a critical chain length n_c and the number ξ of cations per formula unit, the models show regions where a cation monolayer or bilayer is expected. The separation line represents the area where the critical value of either n_c (for fixed cation amounts) or ξ (for fixed cation chain length) is reached. The results where critical ξ were determined from the DFT / MD studies of cations of given chain length n_c are plotted as solid circles here to illustrate their good fit to the models.

With the simple models and the computational studies mostly in agreement as to the value of ξ, we decided to compare a few more analytical techniques to test the robustness of these values. Fig. 4.39 shows results from EDS carried out on pressed discs of C_0 through C_{12}. Looking specifically at the carbon signal, a rough calculation suggests that there should be 2 carbons per Ti_3C_2, plus an addition contribution from the cations as:

$$C_{additional} = \xi \times (n_c + 3) \qquad \text{(Equation 4.8)}$$

The additional 3 C atoms come from the three methyl groups attached to N. Plotting the experimental C/Ti ratio with calculated values at various ξ (as $2 \times C_{additional} / 3$), it is clear that a value of 0.12 for ξ produces an excellent fit of the data.

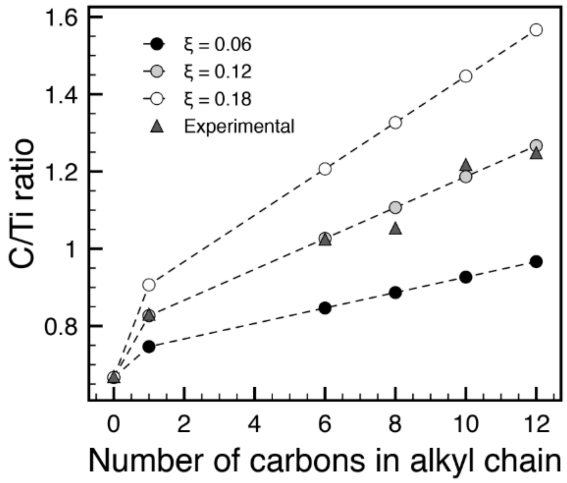

Figure 4.39: EDS data for $Ti_3C_2T_x$ without intercalation (C_0) or intercalated with cations C_1-C_{12}. Experimental data for the ratio C:Ti signal are plotted as solid triangles, with calculated data at various ξ (according to Equation 4.8) plotted as circles. Multiple values of ξ are used to demonstrate how much the fit can be expected to deviate for even small changes in ξ.

Further, XPS analysis of N content (see Ref [151] for full experimental details) gives ξ values of 0.14, 0.15, and 0.10 for C_6, C_8, and C_{10}, respectively. Finally, elemental analysis (Laboratory Testing, Inc., Pennsylvania, USA) conducted on C_6 and C_{12} gave values of 0.11 for both (based on N content). A summary of all experimental and computational values of ξ is provided in Table 4.6 at the end of the section. These are in good agreement with recent reports of intercalated cations as well, with ξ of 0.14 (based on K^+ and Mg^{2+}, produced *via* cation exchange of Li-$Ti_3C_2T_x$).[100]

We then explored the effect of cation chain length on two more physical properties: density and electrical conductivity. Fig. 4.40 shows the density of cation-intercalated MXenes plotted against n_c. Experimental values were determined by forming cold-pressed discs and measuring the mass and dimensions to determine volume and, therefore, density. These values were modeled simply assuming

$$\text{density} = f \times m_{uc} / V_{uc} \qquad \text{(Equation 4.9)}$$

where V_{uc} is the unit cell volume, and m_{uc} is the unit cell mass: $2 \times AA_{\xi}Ti_3C_2T_x$. With ξ values set at 0.12; f is a densification correction factor, set at 0.85 to account for porosity. As most particles are the same size and shape, the porosity of the discs should be relatively consistent. V_{uc} is calculated using the u.c. parameters a and c, with c being the experimental values of the AA-intercalated samples. It seems from Fig. 4.40 that the calculated density is a decent match until the higher values of n_c, around 14-16. This may arise from incomplete exchange due to slowed kinetics.

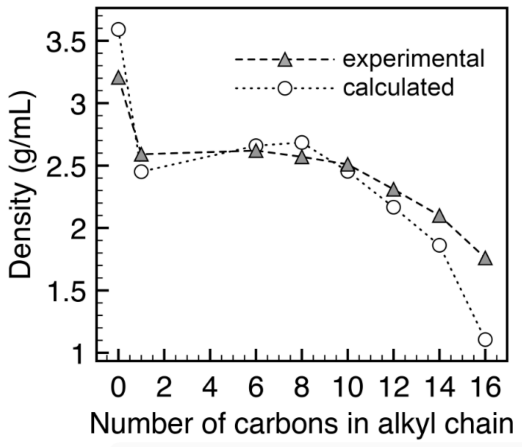

Figure 4.40: Density of $Ti_3C_2T_x$ intercalated with cations C_1-C_{16} (determined by measuring mass, thickness, and area of uniform samples of pressed discs) is plotted as triangles. Density calculated by a simple model assuming 85 % densification of the discs is plotted as circles.

The electrical conductivity was measured on the same discs by four-point probe method, and these results are presented in Fig. 4.41. There seems to be a general trend of increasing resistivity with increasing basal spacing, albeit with some erratic points. These could arise from inconsistencies in intercalation or densification. However, it is clear that it is practically possible to modulate the conductivity of $Ti_3C_2T_x$ *via* tunable cation intercalation.

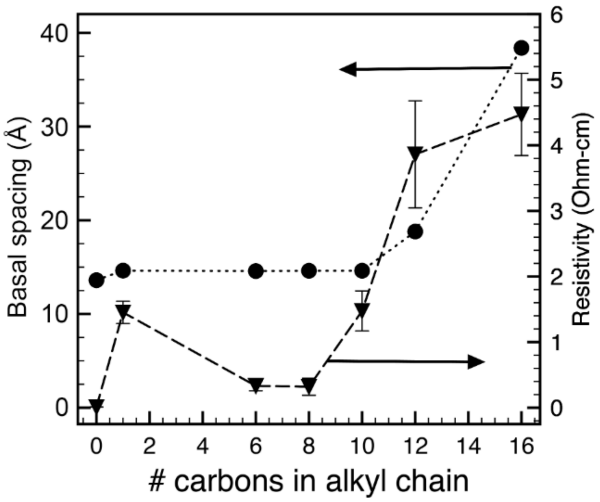

Figure 4.41: Combined plot of the basal spacing (left axis) and resistivity (right axis; measured *via* four-point probe) on cold-pressed discs of $Ti_3C_2T_x$ intercalated with cations C_1-C_{16}.

With the basal spacing a potentially important factor in conductivity modulation, and the fact that there are only certain spacings that arise from the experiments in Fig. 4.31, we set about to see if it would be possible to use blends of cations of different n_c to more carefully tune the spacing. Due to time constraints we leave this as simply a proof-of-concept. Cations C_6 and C_{14} were chosen and intercalated according to the previous procedures. This yielded basal spacings of 14.5 Å and 22.1 Å, respectively.

Then, instead of a 0.1 M solution of one cation, a mixture of 0.05 M solutions of C_6 and C_{14} was used for the intercalation. The resulting structure showed a basal spacing of 19.2 Å (Fig. 4.42), which is close to the mean of the two spacings, 18.3 Å. The diffraction peak of the mixed sample is notably broader than that of the endpoints. It is likely that the interlayer space has less order than the other samples due to mixing effects of the two differently sized cations. It is less likely, but also possible, that we are observing interstratified layers of pure C_6 or C_{14}-intercalated $Ti_3C_2T_x$, which could give rise to an averaged peak. There is precedence for this in the clay literature for various hydration phases,[10] but the self-organization required for this to be the case here seems unlikely to happen.

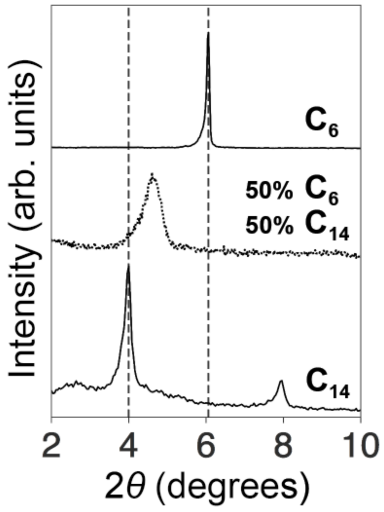

Figure 4.42: XRD patterns of the basal region of $Ti_3C_2T_x$ intercalated with C_{14} (bottom), C_6 (top), and a mixture of both C_6 and C_{14} (middle).

Based on some studies that expanding the interlayer separation, through surface termination sterics[57] or pillaring,[104,105,199] may be a route to improve ion accessibility for electrochemical energy storage, we tested C_0-, C_1-, C_6-, and C_{10}-

$Ti_3C_2T_x$ as active material in electrochemical capacitors, with sulfuric acid, H_2SO_4, as the electrolyte (this work was performed by Sankalp Kota and is detailed in Ref. [151]). Fig. 4.43a shows cyclic voltammetry (CV) performed on these materials, at 5 mV/s. The area of the CV loop showed an increase between C_0- and C_1-$Ti_3C_2T_x$, but there was a significant decrease in area for C_{10}-$Ti_3C_2T_x$. When the capacitance was measured at 2 mV/s (Fig. 4.43b), there was a 12 % increase in capacitance due to the intercalation of C_1, but C_{10} showed a 29 % decrease. In Fig. 4.43c, the intercalated samples show a general trend of decreasing capacitance as n_c is increased, and converge to a similar value at 50 mV/s, which suggests that at that high rate all have the same type of charge storage mechanism, namely in the electrical double layer at the MXene surface or shallow sites in the interlayer. Our interpretation is that there is a modest pillaring effect of C_1, but when n_c is increased, surface sites become blocked, leading to a decrease in capacitance. The alkyl chains are non-polar, which may also hamper diffusion of the sulphuric acid electrolyte (hydrophobization effects of AA cation intercalation in other materials were discussed earlier). As noted from Fig. 4.41, there may also be a moderate increase in resistance for the material as n_c is increased, impeding charge transfer. We leave this study with the fact that we have at least shown tunable modulation of the capacitance (even though it is not in the desired direction), but also note that, while we did not have success improving the capacitance in H_2SO_4, organic electrolytes may be more compatible with these hydrophobic pillars. Recent work has suggested alternate routes to improvement in capacitance of Li-ion capacitors, by using AA cations to pre-tune interlayer spacing as a template, followed by reaction with Sn^{4+} ions to make permanent pillars.[110]

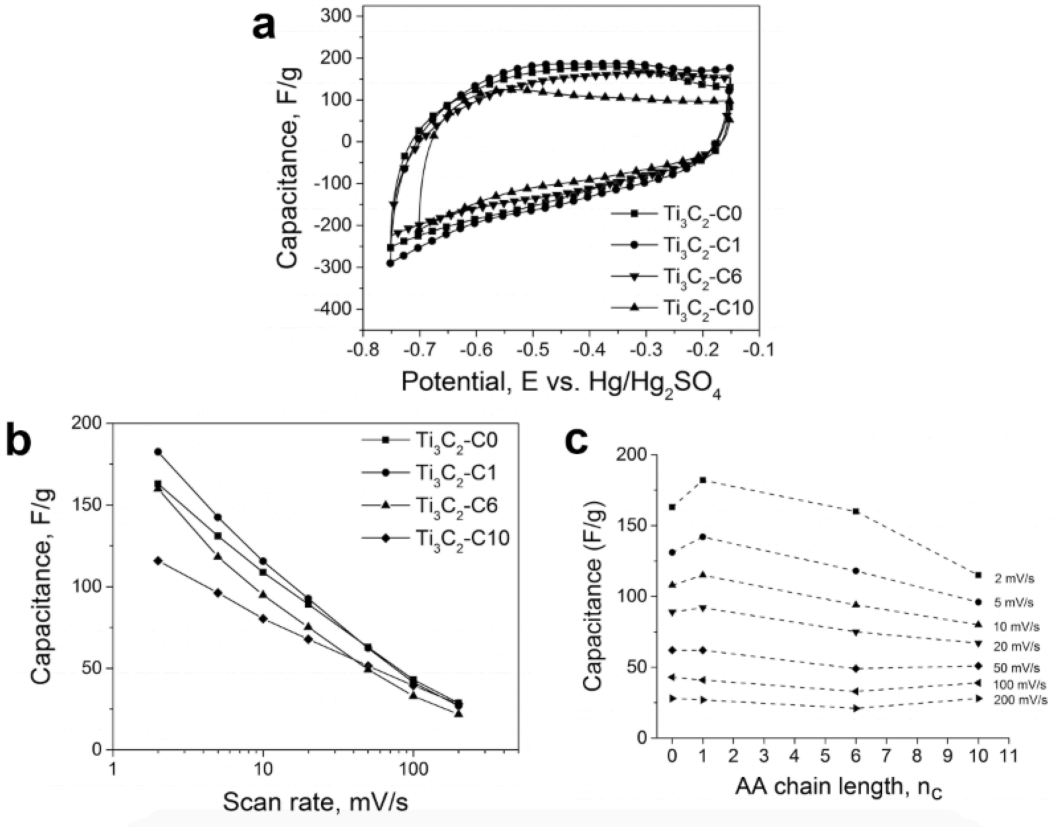

Figure 4.43: a) Cyclic voltammetry (CV) performed on electrodes containing $Ti_3C_2T_x$ intercalated with C_1, C_6, an C_{10}, or in an unintercalated state (C_0; as-synthesized from HF alone), in sulfuric acid electrolyte. b) Capacitance of same materials as a function of CV scan rate. c) Capacitance of same materials at various scan rates plotted against the cation alkyl chain length n_c.

Finally, the methodology of a series of varied-n_c cation intercalation was repeated on $Ti_3C_2T_x$ produced by the different etching system of $LiF+H_2SO_4$, and on two other MXene compositions produced by HF+LiCl, *viz*. Ti_2CT_x and Nb_2CT_x, to get a sense of general applicability and to try to determine ξ to see how it varied. XRD patterns from these studies are shown in Fig. 4.44. It is clear that the same type of discontinuous expansion effects are present, with a transition region at C_{10} for $Ti_3C_2T_x/LiF+H_2SO_4$ and for Ti_2CT_x. Nb_2CT_x shows a transition region at C_{12}.

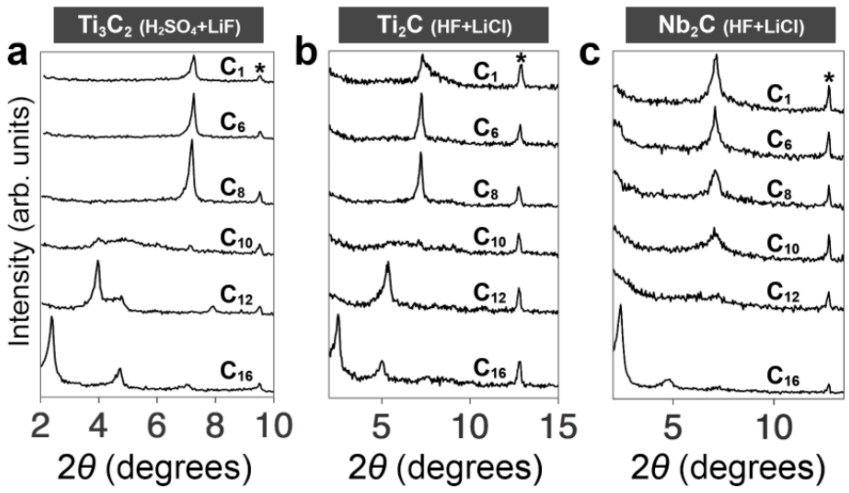

Figure 4.44: Low angle XRD patterns of MXene that has been exchanged with cations C_1-C_{16} for, a) $Ti_3C_2T_x$ produced by H_2SO_4+LiF, b) Ti_2CT_x produced by HF+LiCl, and c) Nb_2CT_x produced by HF+LiCl. Asterisks denote the {002} reflection of residual unreacted MAX phase, that unsurprisingly do not vary.

Taking the aforementioned transition regions as the critical n_c values and making sure to calculate interlayer volumes using the specific unit cell parameters of these new MXenes, Fig. 4.45 shows the same type of analysis as earlier (here the previously-used 'Model 2' involving extra care in interlayer separation determination was skipped for brevity). Based on these results, the cation density ξ was determined to be 0.10 for $Ti_3C_2T_x$/LiF+H_2SO_4, 0.09_5 for Ti_2CT_x, and 0.09_5 for Nb_2CT_x (these are summarized with earlier values in Table 4.6).

It follows that the values of ξ for multiple MXene compositions across multiple synthesis methods seem to be fairly uniform and constant, and this AA intercalation method may be recommended for use in determining ξ of MXenes in the future. The accuracy of determination of ξ can be improved by selecting cations with smaller differences in alkyl chain length around the transition region, i.e. by using C_9, C_{10}, C_{11} instead of C_8, C_{10}, C_{12}. As a final note to the applications of AA cation

intercalation, such intercalated phases in clays have been shown to cause the intensity of basal diffraction peaks to increase 100-fold.[200] For etchings of new MXene compositions where yields may be too low and be missed by normal XRD methods, AA intercalation could help to boost intensities enough for detection of successful etching.

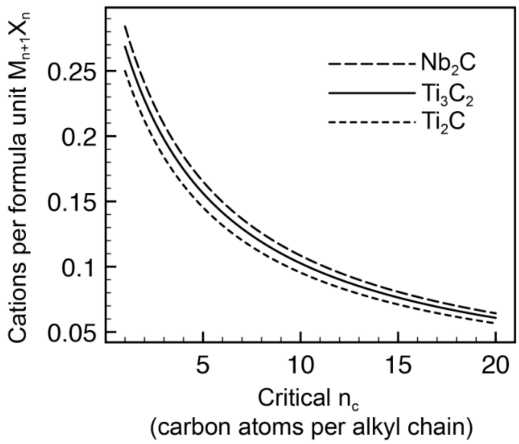

Figure 4.45: Plots of the simple model of cation packing (from Equation 4.7 as in Fig. 4.38, but with adjusted calculations for the different *a* lattice parameters of the new MXene compositions) for $Ti_3C_2T_x$ produced by H_2SO_4+LiF and Ti_2CT_x and Nb_2CT_x produced by HF+LiCl. From the data in Fig. 4.44, the critical n_c was selected as 10, 10, and 12 for the three respective MXenes.

Table 4.6: Summarized data for number of cations ξ per Ti_3C_2

MXene	*Method*	ξ
$Ti_3C_2T_x$ / HF+LiCl	Simple model 1	0.09-0.1
	Simple model 2	0.13-0.15
	XPS	0.14 (C_6), 0.15 (C_8), 0.10 (C_{10})
	EDS	0.12
	Elemental Analysis	0.11 (C_6 and C_{12})
	Computational methods	0.123
$Ti_3C_2T_x$ / H_2SO_4+LiF	Simple model 1	0.1
Ti_2CT_x / HF+LiCl		0.09_5
Nb_2CT_x / HF+LiCl		0.09_5

Section Summary

Organoammonium cations show great promise for modulation of MXene properties. In the limited scope of this section, we have used AA cation intercalation to determine the cation exchange capacity, ξ, mitigate humidity effects on structure, and modulate conductivity and capacitance. The cation exchange capacity is a very important parameter in linking MXenes to clay minerals and in its use in applications where exchange is necessary.

Future Work

The AA cations used here are just a tiny fraction of the functionalities available, so there is much room to explore in this subject with the potential for very exciting properties. The same chemistry may be used to insert intercalants that change structure upon exposure to light,[14,201] hydrophobize the interlayer space (possibly allowing for dispersion in nonpolar solvents),[12] or allow for redox chemistry.[202]

CHAPTER 5 - SUMMARY AND FUTURE DIRECTIONS

This project has laid the foundations of controlled intercalation of desired cations into MXene and evaluated the potential dynamic structural response to various stimuli. In doing so it has given quantitative and qualitative links between MXenes and clay minerals as well as layered dichalcogenides. The overall branches of the intercalation studies have included:

1. Initial works on improving the safety of etching, by exploring alternatives to HF in the form of acid and salt combinations. As a result of these studies, MXene was produced in a form that could be molded like clay and readily rolled into freestanding films. The groundwork for other cations and crystalline swelling was laid.
2. Alkali and alkaline earth metal cations: Li^+, Na^+, K^+, Rb^+, Cs^+; Mg^{2+}, Ca^{2+}. From these, we have learned that the intercalated cation can attract H_2O molecules in accordance with its hydration enthalpy; the H_2O then go on to swell the structure and increase the basal spacing, in line with results from both clay minerals and layered dichalcogenides. Further, we have found evidence of pseudo-negative compressibility along the *c* direction of $Ti_3C_2T_x$, where H_2O enters and expands the structure even with coaxial increases in compressive stress; we have attributed this, potentially, to shearing of the nanosheets; the intercalation of ions such as K^+ suppresses this effect.
3. Transition metal cations: along the same lines as for alkali and alkaline earth cations, we have demonstrated intercalation of transition metal cations;

however, due to the scope of this project, additional effects that might accompany their intercalation (such as magnetic properties) have not been able to be explored.

4. Alkylammonium cations: the intercalation of organocations of the form $[(CH_3)_3NC_nH_{2n+1}]^+$ (where n ranges from 1 to 16) was successful. Discontinuous changes in basal spacings were observed to correlate with the chain length (described by n); this was described by a simple volume-packing analysis, as well as the modern computation techniques of density functional theory combined with molecular dynamics. The results were used to obtain a cation exchange capacity value for $Ti_3C_2T_x$. Electrical conductivity was strongly affected by the intercalation; an increase in resistivity was roughly correlated with increase in basal spacing. Further, the intercalations and analysis methodology were applied to both Ti_2CT_x and Nb_2CT_x, as well as $Ti_3C_2T_x$ etched by H_2SO_4+LiF.

In the end, based on the results from this work, we can definitively say that MXenes *do* behave like 'conductive clays', and hope that we have convinced the reader as to why this is the case.

Future outlook

There are many paths that are unexplored in MXene, especially with it being such a new material. We outline here some, in relation to this project, that we believe are especially worth exploring in future work.

1. *Deeper investigation into cation / H_2O interactions*. It is clear that there is much work to be done to better understand phenomena at play in interactions between MXene, cations, and H_2O; this work has only provided a foundation, and there are many advanced characterization techniques available such as NMR, neutron and x-ray diffraction combined with PDF analysis, Raman spectroscopy, *etc*. The amount of quality publications recently on this topic is suggestive that the field will be invested in these investigations.
2. *Exploration of new cations.* The clay minerals, transition metal dichalcogenides, and other layered material literatures demonstrate many cation intercalations that have not yet been explored in MXenes. Based upon the diversity of structural tunings that we have achieved through three groups of cations, we believe that an incredibly worthwhile study would be a more thorough screening of intercalable cations. One of the most interesting groups of metal cations are the heavy metals. Transition metal intercalation may have promise to endow MXene with magnetic or redox properties. For remediation purposes, we have already seen successful exploration of MXenes as adsorbents of metals such as Cr, Pb, Hg (as described in Chapter 2), and believe this will continue with fruitful research. Further, studies of cation and H_2O intercalation on MXenes could help to fill in gaps of knowledge in other materials that display the same phenomena.
3. *Organoammonium cations.* In this study we have presented alkylammonium cation intercalations of a rather limited form. The structural and functional diversity of ammonium cations is immense. For example, cations containing

azobenzene moieties have been shown to alter the basal spacing of other layered materials in real time with application of light, as discussed in earlier chapters. With a material such as MXene, with high electrical conductivity, that is partially dependent upon basal spacing, this could add a great depth for electronics applications *e.g.* in photo-switching, in addition to the ability to dynamically tune nanopore size for intercalation purposes. With that said, many of the effects proposed through organic cation intercalation can probably be accomplished as well with the growing sub-field of MXene/polymer composites, especially given the vast tailorability of synthetic polymer chemistry; we expect to see much growth of the field in this direction.[85,203,204,205,206]

4. *Extension to other MXenes*. One of the most obvious future pursuits is to apply the methodologies described herein to other MXenes. This work was relatively limited to $Ti_3C_2T_x$; since there are now so many MXene compositions (the number of which is growing yearly), extension of ion intercalation protocols to the compositional diversity of MXenes will surely yield very promising control over properties. Exploring some of the same phenomena reported in this work on other MXene compositions should help to answer questions that have arisen with $Ti_3C_2T_x$.

Concluding remarks

This work has sought, from the start, to link MXenes to clay minerals (and other layered materials). To do this, it has involved resurrecting some parts of earlier literatures and applying them to MXenes, and has been focused on establishing the groundwork for a select group of phenomena. With this, there has been a focus on less-sophisticated characterization techniques to establish a framework of what is best to explore with more advanced techniques later. Given the pace of advancement of MXene research, especially in the area of applications, it is our hope that more energy is devoted to using these results with a broad range of techniques to advance the basic science of MXene structure and properties, as these are fundamentally important to developing the material in applications.

LIST OF REFERENCES

1. Heiligtag, F. J. & Niederberger, M. The fascinating world of nanoparticle research. *Mater. Today* **16,** 262–271 (2013).

2. Naguib, M. *et al.* Two-Dimensional Nanocrystals Produced by Exfoliation of Ti_3AlC_2. *Adv. Mater.* **23,** 4248–4253 (2011).

3. Yang, J. *et al.* Two-Dimensional Nb-Based M_4C_3 Solid Solutions (MXenes). *J. Am. Ceram. Soc.* **99,** 660–666 (2016).

4. Anasori, B. *et al.* Two-Dimensional, Ordered, Double Transition Metals Carbides (MXenes). *ACS Nano* **9,** 9507–9516 (2015).

5. Naguib, M. *et al.* Two-Dimensional Transition Metal Carbides. *ACS Nano* **6,** 1322–1331 (2012).

6. Borysiuk, V. N., Mochalin, V. N. & Gogotsi, Y. Bending rigidity of two-dimensional titanium carbide (MXene) nanoribbons: A molecular dynamics study. *Comput. Mater. Sci.* **143,** 418–424 (2018).

7. Xie, Y. & Kent, P. R. C. Hybrid density functional study of structural and electronic properties of functionalized $Ti_{n+1}X_n$ (X=C, N) monolayers. *Phys. Rev. B* **87,** 235441 (2013).

8. Dillon, A. D. *et al.* Highly Conductive Optical Quality Solution-Processed Films of 2D Titanium Carbide. *Adv. Funct. Mater.* **26,** 4162–4168 (2016).

9. Lukatskaya, M. R. *et al.* Cation Intercalation and High Volumetric Capacitance of Two-Dimensional Titanium Carbide. *Science* **341,** 1502–1505 (2013).

10. Norrish, K. The swelling of montmorillonite. *Discuss Faraday Soc* **18,** 120–134 (1954).

11. Zhu, J., He, H., Guo, J., Yang, D. & Xie, X. Arrangement models of alkylammonium cations in the interlayer of HDTMA+ pillared montmorillonites. *Chin. Sci. Bull.* **48,** 368–372 (2003).

12. de Paiva, L. B., Morales, A. R. & Valenzuela Díaz, F. R. Organoclays: Properties, preparation and applications. *Appl. Clay Sci.* **42,** 8–24 (2008).

13. Cases, J. M. *et al.* Mechanism of adsorption and desorption of water vapor by homoionic montmorillonite. 1. The sodium-exchanged form. *Langmuir* **8,** 2730–2739 (1992).

14. Fujita, T., Iyi, N. & Klapyta, Z. Preparation of azobenzene-mica complex and its photoresponse to ultraviolet irradiation. *Mater. Res. Bull.* **33,** 1693–1701 (1998).

15. Wada, N., Raythatha, R. & Minomura, S. Pressure effects on water-intercalated kaolinite. *Solid State Commun.* **63,** 783–786 (1987).

16. A.M. Hermann. Electrical Resistivity of Intercalated Molybdenum Disulfide. *Solid State Commun.* **13,** 1065–1068 (1973).

17. White, G. N. & Zelazny, L. W. Analysis and implications of the edge structure of dioctahedral phyllosilicates. *CLAYS CLAY Min. Clays Clay Min.* **36,** 141 (1988).

18. Marry, V., Turq, P., Cartailler, T. & Levesque, D. Microscopic simulation of structure and dynamics of water and counterions in a monohydrated montmorillonite. *J. Chem. Phys.* **117,** 3454–3463 (2002).

19. Bérend, I. *et al.* Mechanism of adsorption and desorption of water vapor by homoionic montmorillonites: 2. The Li^+, Na^+, K^+, Rb^+, and Cs^+-exchanged forms. *Clays Clay Miner.* **43,** 324–336 (1995).

20. Hendricks, S. B., Nelson, R. A. & Alexander, L. T. Hydration Mechanism of the Clay Mineral Montmorillonite Saturated with Various Cations. *J. Am. Chem. Soc.* **62,** 1457–1464 (1940).

21. Papelis, C. & Hayes, K. F. Distinguishing between interlayer and external sorption sites of clay minerals using X-ray absorption spectroscopy. *Colloids Surf. Physicochem. Eng. Asp.* **107,** 89–96 (1996).

22. Kharroubi, M. *et al.* Dehydration enthalpy of alkali-cations-exchanged montmorillonite from thermogravimetric analysis. *J. Colloid Interface Sci.* **329,** 339–345 (2009).

23. Tamura, K., Yamada, H. & Nakazawa, H. Stepwise hydration of high-quality synthetic smectite with various cations. *Clays Clay Miner.* **48,** 400–404 (2000).

24. Tambach, T. J., Bolhuis, P. G. & Smit, B. A Molecular Mechanism of Hysteresis in Clay Swelling. *Angew. Chem.* **116,** 2704–2706 (2004).

25. Stul, M. S. & Uytterhoeven, J. B. Interlamellar sorption of ethanol on montmorillonite clays with different layer charges. *J. Chem. Soc. Faraday Trans. 1 Phys. Chem. Condens. Phases* **71,** 1396–1401 (1975).

26. Amorim, C. L. G. *et al.* Effect of clay–water interactions on clay swelling by X-ray diffraction. *Nucl. Instrum. Methods Phys. Res. Sect. Accel. Spectrometers Detect. Assoc. Equip.* **580,** 768–770 (2007).

27. Ferrage, E., Lanson, B., Michot, L. J. & Robert, J.-L. Hydration Properties and Interlayer Organization of Water and Ions in Synthetic Na-Smectite with Tetrahedral Layer Charge. Part 1. Results from X-ray Diffraction Profile Modeling. *J. Phys. Chem. C* **114,** 4515–4526 (2010).

28. Izawa, H., Kikkawa, S. & Koizumi, M. Ion exchange and dehydration of layered [sodium and potassium] titanates, Na2Ti3O7 and K2Ti4O9. *J. Phys. Chem.* **86,** 5023–5026 (1982).

29. Sasaki, T. & Watanabe, M. Osmotic swelling to exfoliation. Exceptionally high degrees of hydration of a layered titanate. *J. Am. Chem. Soc.* **120,** 4682–4689 (1998).

30. Khan, A. I. & O'Hare, D. Intercalation chemistry of layered double hydroxides: recent developments and applications. *J. Mater. Chem.* **12,** 3191–3198 (2002).

31. Hou, X., Bish, D. L., Wang, S.-L., Johnston, C. T. & Kirkpatrick, R. J. Hydration, expansion, structure, and dynamics of layered double hydroxides. *Am. Mineral.* **88,** 167–179 (2003).

32. Sasaki, T. *et al.* A Mixed Alkali Metal Titanate with the Lepidocrocite-like Layered Structure. Preparation, Crystal Structure, Protonic Form, and Acid−Base Intercalation Properties. *Chem. Mater.* **10,** 4123–4128 (1998).

33. Iyi, N., Fujii, K., Okamoto, K. & Sasaki, T. Factors influencing the hydration of layered double hydroxides (LDHs) and the appearance of an intermediate second staging phase. *Appl. Clay Sci.* **35,** 218–227 (2007).

34. Wang, Q. & O'Hare, D. Recent Advances in the Synthesis and Application of Layered Double Hydroxide (LDH) Nanosheets. *Chem. Rev.* **112,** 4124–4155 (2012).

35. Williams, G. R. & O'Hare, D. Towards understanding, control and application of layered double hydroxide chemistry. *J. Mater. Chem.* **16,** 3065 (2006).

36. Mattheiss, L. F. Band structures of transition-metal-dichalcogenide layer compounds. *Phys. Rev. B* **8,** 3719 (1973).

37. Wang, Q. H., Kalantar-Zadeh, K., Kis, A., Coleman, J. N. & Strano, M. S. Electronics and optoelectronics of two-dimensional transition metal dichalcogenides. *Nat. Nanotechnol.* **7,** 699–712 (2012).

38. Somoano, R. B. Alkali metal intercalates of molybdenum disulfide. *J. Chem. Phys.* **58,** 697 (1973).

39. Robert Schöllhorn & Armin Weiss. Cation Exchange Reactions and Layer Solvate Complexes of Termary Phases MxMoS2. *J. -Common Met.* **36,** 229–236 (1974).

40. E. Benavente, M.A. Santa Ana, F. Mendizábal & G. González. Intercalation chemistry of molybdenum disulfide. *Chem. Mater.* **224,** 87–109 (2002).

41. Novoselov, K. S. *et al.* Electric field effect in atomically thin carbon films. *science* **306,** 666–669 (2004).

42. Nicolosi, V., Chhowalla, M., Kanatzidis, M. G., Strano, M. S. & Coleman, J. N. Liquid Exfoliation of Layered Materials. *Science* **340,** 1226419–1226419 (2013).

43. Forsman, W. C., Dziemianowicz, T., Leong, K. & Carl, D. Graphite intercalation chemistry: an interpretive review. *Synth. Met.* **5,** 77–100 (1983).

44. Geim, A. K. & Novoselov, K. S. The rise of graphene. in *Nanoscience And Technology: A Collection of Reviews from Nature Journals* 11–19 (World Scientific, 2010).

45. Wang, X., Feng, H., Wu, Y. & Jiao, L. Controlled Synthesis of Highly Crystalline MoS_2 Flakes by Chemical Vapor Deposition. *J. Am. Chem. Soc.* **135,** 5304–5307 (2013).

46. Joensen, P., Frindt, R. F. & Morrison, S. R. Single-layer MoS2. *Mater. Res. Bull.* **21,** 457–461 (1986).

47. Nowotny, V. H. Strukturchemie einiger verbindungen der übergangsmetalle mit den elementen C, Si, Ge, Sn. *Prog. Solid State Chem.* **5,** 27–70 (1971).

48. Barsoum, M. W. The $M_{n+1}AX_n$ phases: A new class of solids: Thermodynamically stable nanolaminates. *Prog. Solid State Chem.* **28,** 201–281 (2000).

49. Hu, C. *et al.* Mo_2Ga_2C: a new ternary nanolaminated carbide. *Chem Commun* **51,** 6560–6563 (2015).

50. Fashandi, H. *et al.* Ti_2Au_2C and $Ti_3Au_2C_2$ formed by solid state reaction of gold with Ti_2AlC and Ti_3AlC_2. *Chem. Commun.* **53,** 9554–9557 (2017).

51. Anasori, B. *et al.* Experimental and theoretical characterization of ordered MAX phases Mo_2TiAlC_2 and $Mo_2Ti_2AlC_3$. *J. Appl. Phys.* **118,** 094304 (2015).

52. Lu, J. *et al.* Theoretical and Experimental Exploration of a Novel In-Plane Chemically Ordered $(Cr_{2/3}M_{1/3})_2AlC$ *i*-MAX Phase with M = Sc and Y. *Cryst. Growth Des.* **17,** 5704–5711 (2017).

53. Halim, J. *et al.* Transparent Conductive Two-Dimensional Titanium Carbide Epitaxial Thin Films. *Chem. Mater.* **26,** 2374–2381 (2014).

54. Zhou, J. *et al.* A Two-Dimensional Zirconium Carbide by Selective Etching of Al_3C_3 from Nanolaminated $Zr_3Al_3C_5$. *Angew. Chem. Int. Ed.* **55,** 5008–5013 (2016).

55. Tao, Q. *et al.* Two-dimensional $Mo_{1.33}C$ MXene with divacancy ordering prepared from parent 3D laminate with in-plane chemical ordering. *Nat. Commun.* **8,** 14949 (2017).

56. Halim, J. *et al.* X-ray photoelectron spectroscopy of select multi-layered transition metal carbides (MXenes). *Appl. Surf. Sci.* **362,** 406–417 (2016).

57. Kajiyama, S. *et al.* Enhanced Li-Ion Accessibility in MXene Titanium Carbide by Steric Chloride Termination. *Adv. Energy Mater.* **7,** 1601873 (2017).

58. Enyashin, A. N. & Ivanovskii, A. L. Structural and Electronic Properties and Stability of MXenes Ti_2C and Ti_3C_2 Functionalized by Methoxy Groups. *J. Phys. Chem. C* **117,** 13637–13643 (2013).

59. Hope, M. A. *et al.* NMR reveals the surface functionalisation of Ti_3C_2 MXene. *Phys Chem Chem Phys* **18,** 5099–5102 (2016).

60. Persson, I. *et al.* On the organization and thermal behavior of functional groups on Ti_3C_2 MXene surfaces in vacuum. *2D Mater.* **5,** 015002 (2017).

61. Hu, T. *et al.* Chemical Origin of Termination-Functionalized MXenes: $Ti_3C_2T_2$ as a Case Study. *J. Phys. Chem. C* **121,** 19254–19261 (2017).

62. Peng, Q. *et al.* Unique Lead Adsorption Behavior of Activated Hydroxyl Group in Two-Dimensional Titanium Carbide. *J. Am. Chem. Soc.* **136,** 4113–4116 (2014).

63. Naguib, M., Unocic, R. R., Armstrong, B. L. & Nanda, J. Large-scale delamination of multi-layers transition metal carbides and carbonitrides "MXenes". *Dalton Trans* (2015). doi:10.1039/C5DT01247C

64. Hu, M. *et al.* High-Capacitance Mechanism for $Ti_3C_2T_x$ MXene by *in Situ* Electrochemical Raman Spectroscopy Investigation. *ACS Nano* (2016). doi:10.1021/acsnano.6b06597

65. Lukatskaya, M. R. *et al.* Probing the Mechanism of High Capacitance in 2D Titanium Carbide Using In Situ X-Ray Absorption Spectroscopy. *Adv. Energy Mater.* **5,** 1500589 (2015).

66. Osti, N. C. *et al.* Evidence of molecular hydrogen trapped in two-dimensional layered titanium carbide-based MXene. *Phys. Rev. Mater.* **1,** (2017).

67. Mashtalir, O., Naguib, M., Dyatkin, B., Gogotsi, Y. & Barsoum, M. W. Kinetics of aluminum extraction from Ti_3AlC_2 in hydrofluoric acid. *Mater. Chem. Phys.* **139,** 147–152 (2013).

68. Wang, H.-W., Naguib, M., Page, K., Wesolowski, D. J. & Gogotsi, Y. Resolving the Structure of $Ti_3C_2T_x$ MXenes through Multilevel Structural Modeling of the Atomic Pair Distribution Function. *Chem. Mater.* **28,** 349–359 (2016).

69. Khazaei, M., Arai, M., Sasaki, T., Estili, M. & Sakka, Y. The effect of the interlayer element on the exfoliation of layered Mo_2AC (A = Al, Si, P, Ga, Ge, As or In) MAX phases into two-dimensional Mo_2C nanosheets. *Sci. Technol. Adv. Mater.* **15,** 014208 (2014).

70. Xie, J., Wang, X., Li, A., Li, F. & Zhou, Y. Corrosion behavior of selected $M_{n+1}AX_n$ phases in hot concentrated HCl solution: Effect of A element and MX layer. *Corros. Sci.* **60,** 129–135 (2012).

71. Zhang, C. J. *et al.* Oxidation Stability of Colloidal Two-Dimensional Titanium Carbides (MXenes). *Chem. Mater.* **29,** 4848–4856 (2017).

72. Halim, J. An X-Ray Photoelectron Spectroscopy Study of Multilayered Transition Metal Carbides (MXenes). (2016).

73. Zhang, C. J. *et al.* Layered Orthorhombic $Nb_2O_5@Nb_4C_3T_x$ and $TiO_2@Ti_3C_2T_x$ Hierarchical Composites for High Performance Li-ion Batteries. *Adv. Funct. Mater.* **26,** 4143–4151 (2016).

74. Naguib, M. *et al.* One-step synthesis of nanocrystalline transition metal oxides on thin sheets of disordered graphitic carbon by oxidation of MXenes. *Chem. Commun.* (2014). doi:10.1039/c4cc01646g

75. Ghassemi, H. *et al.* In situ environmental transmission electron microscopy study of oxidation of two-dimensional Ti_3C_2 and formation of carbon-supported TiO_2. *J. Mater. Chem. A* **2,** 14339 (2014).

76. Zhang, X., Ma, Z., Zhao, X., Tang, Q. & Zhou, Z. Computational studies on structural and electronic properties of functionalized MXene monolayers and nanotubes. *J. Mater. Chem. A* **3,** 4960–4966 (2015).

77. Halim, J. *et al.* Synthesis and Characterization of 2D Molybdenum Carbide (MXene). *Adv. Funct. Mater.* **26,** 3118–3127 (2016).

78. Mashtalir, O. *et al.* Intercalation and delamination of layered carbides and carbonitrides. *Nat. Commun.* **4,** 1716 (2013).

79. Ghidiu, M., Lukatskaya, M. R., Zhao, M.-Q., Gogotsi, Y. & Barsoum, M. W. Conductive two-dimensional titanium carbide 'clay' with high volumetric capacitance. *Nature* **516,** 78–81 (2014).

80. Ling, Z. *et al.* Flexible and conductive MXene films and nanocomposites with high capacitance. *Proc. Natl. Acad. Sci.* **111,** 16676–16681 (2014).

81. Byeon, A. *et al.* Lithium-ion capacitors with 2D Nb_2CT_x (MXene) – carbon nanotube electrodes. *J. Power Sources* **326,** 686–694 (2016).

82. Zhao, M.-Q. *et al.* 2D titanium carbide and transition metal oxides hybrid electrodes for Li-ion storage. *Nano Energy* **30,** 603–613 (2016).

83. Ying, G., Dillon, A. D., Fafarman, A. T. & Barsoum, M. W. Transparent, conductive solution processed spincast 2D Ti_2CT_x (MXene) films. *Mater. Res. Lett.* **5,** 391–398 (2017).

84. Hantanasirisakul, K. *et al.* Fabrication of $Ti_3C_2T_x$ MXene Transparent Thin Films with Tunable Optoelectronic Properties. *Adv. Electron. Mater.* **2,** 1600050 (2016).

85. Mayerberger, E. A., Urbanek, O., Street, R. M., Barsoum, M. W. & Schauer, C. L. Preparation and characterization of polymer-$Ti_3C_2T_x$ (MXene) composite nanofibers produced via electrospinning. *J. Appl. Polym. Sci.* 45295 (2017).

86. Collini, P., Kota, S., Dillon, A. D., Barsoum, M. W. & Fafarman, A. T. Electrophoretic Deposition of Two-Dimensional Titanium Carbide (MXene) Thick Films. *J. Electrochem. Soc.* **164,** D573–D580 (2017).

87. Naguib, M. *et al.* On the Topotactic Transformation of Ti_2AlC into a Ti–C–O–F Cubic Phase by Heating in Molten Lithium Fluoride in Air. *J. Am. Ceram. Soc.* **94,** 4556–4561 (2011).

88. Li, Z. *et al.* Synthesis and thermal stability of two-dimensional carbide MXene Ti_3C_2. *Mater. Sci. Eng. B* **191,** 33–40 (2015).

89. Urbankowski, P. *et al.* Synthesis of two-dimensional titanium nitride Ti_4N_3 (MXene). (2016).

90. Lukatskaya, M. R. *et al.* Room-Temperature Carbide-Derived Carbon Synthesis by Electrochemical Etching of MAX Phases. *Angew. Chem.* **126,** 4977–4980 (2014).

91. Zhao, M.-Q. *et al.* Synthesis of Carbon/Sulfur Nanolaminates by Electrochemical Extraction of Titanium from Ti_2SC. *Angew. Chem.* n/a-n/a (2015). doi:10.1002/ange.201500110

92. Sun, W. *et al.* Electrochemical etching of Ti_2AlC to Ti2CT_x (MXene) in low-concentration hydrochloric acid solution. *J Mater Chem A* **5,** 21663–21668 (2017).

93. Wang, X. *et al.* New etching environment (FeF_3/HCl) for the synthesis of two-dimensional titanium carbide MXenes: a route towards selective reactivity vs water. (2017).

94. Yu, X. *et al.* Fluorine-free preparation of titanium carbide MXene quantum dots with high near-infrared photothermal performances for cancer therapy. *Nanoscale* **9,** 17859–17864 (2017).

95. Levi, M. D. *et al.* Solving the Capacitive Paradox of 2D MXene using Electrochemical Quartz-Crystal Admittance and In Situ Electronic Conductance Measurements. *Adv. Energy Mater.* **5,** 1400815 (2014).

96. Gao, Q. *et al.* Synergetic effects of K^+ and Mg^{2+} ion intercalation on the electrochemical and actuation properties of the two-dimensional Ti_3C_2 MXene. *Faraday Discuss.* **199,** 393–403 (2017).

97. Naguib, M., Mochalin, V. N., Barsoum, M. W. & Gogotsi, Y. 25th Anniversary Article: MXenes: A New Family of Two-Dimensional Materials. *Adv. Mater.* **26,** 992–1005 (2014).

98. Wang, X. *et al.* Atomic-Scale Recognition of Surface Structure and Intercalation Mechanism of Ti_3C_2X. *J. Am. Chem. Soc.* 150217105211008 (2015). doi:10.1021/ja512820k

99. Osti, N. C. *et al.* Effect of Metal Ion Intercalation on the Structure of MXene and Water Dynamics on its Internal Surfaces. *ACS Appl. Mater. Interfaces* 8859–8863 (2016). doi:10.1021/acsami.6b01490

100. Muckley, E. S. *et al.* Multimodality of Structural, Electrical, and Gravimetric Responses of Intercalated MXenes to Water. *ACS Nano* **11,** 11118–11126 (2017).

101. Osti, N. C. *et al.* Influence of metal ions intercalation on the vibrational dynamics of water confined between MXene layers. *Phys. Rev. Mater.* **1,** (2017).

102. Naguib, M. *et al.* MXene: a promising transition metal carbide anode for lithium-ion batteries. *Electrochem. Commun.* **16,** 61–64 (2012).

103. Berdiyorov, G. R. & Mahmoud, K. A. Effect of surface termination on ion intercalation selectivity of bilayer $Ti_3C_2T_2$ (T=F, O and OH) MXene. *Appl. Surf. Sci.* **416,** 725–730 (2017).

104. Sun, Y., Chen, D. & Liang, Z. Two-dimensional MXenes for energy storage and conversion applications. *Mater. Today Energy* **5,** 22–36 (2017).

105. Zhang, X., Zhang, Z. & Zhou, Z. MXene-based materials for electrochemical energy storage. *J. Energy Chem.* (2017). doi:10.1016/j.jechem.2017.08.004

106. Naguib, M. *et al.* New Two-Dimensional Niobium and Vanadium Carbides as Promising Materials for Li-Ion Batteries. *J. Am. Chem. Soc.* **135,** 15966–15969 (2013).

107. Liang, X., Garsuch, A. & Nazar, L. F. Sulfur Cathodes Based on Conductive MXene Nanosheets for High-Performance Lithium-Sulfur Batteries. *Angew. Chem. Int. Ed.* **54,** 3907–3911 (2015).

108. Er, D., Li, J., Naguib, M., Gogotsi, Y. & Shenoy, V. B. Ti_3C_2 MXene as a High Capacity Electrode Material for Metal (Li, Na, K, Ca) Ion Batteries. *ACS Appl. Mater. Interfaces* **6,** 11173–11179 (2014).

109. Wu, Y. *et al.* MoS_2-Nanosheet-Decorated 2D Titanium Carbide (MXene) as High-Performance Anodes for Sodium-Ion Batteries. *ChemElectroChem* **4,** 1560–1565 (2017).

110. Luo, J. *et al.* Pillared Structure Design of MXene with Ultralarge Interlayer Spacing for High-Performance Lithium-Ion Capacitors. *ACS Nano* **11,** 2459–2469 (2017).

111. Simon, P. Two-Dimensional MXene with Controlled Interlayer Spacing for Electrochemical Energy Storage. *ACS Nano* **11,** 2393–2396 (2017).

112. Lukatskaya, M. R. *et al.* Ultra-high-rate pseudocapacitive energy storage in two-dimensional transition metal carbides. *Nat. Energy* **2,** 17105 (2017).

113. Tang, Q., Zhou, Z. & Shen, P. Are MXenes Promising Anode Materials for Li Ion Batteries? Computational Studies on Electronic Properties and Li Storage Capability of Ti_3C_2 and $Ti_3C_2X_2$ (X = F, OH) Monolayer. *J. Am. Chem. Soc.* **134,** 16909–16916 (2012).

114. Eames, C. & Islam, M. S. Ion Intercalation into Two-Dimensional Transition-Metal Carbides: Global Screening for New High-Capacity Battery Materials. *J. Am. Chem. Soc.* **136,** 16270–16276 (2014).

115. Ying, Y. *et al.* Two-Dimensional Titanium Carbide for Efficiently Reductive Removal of Highly Toxic Chromium(VI) from Water. *ACS Appl. Mater. Interfaces* **7,** 1795–1803 (2015).

116. Shahzad, A. *et al.* Mercuric Ion Capturing by Recoverable Titanium Carbide Magnetic Nanocomposite. *J. Hazard. Mater.* (2017). doi:10.1016/j.jhazmat.2017.11.026

117. Zhang, Y.-J. *et al.* Adsorption of uranyl species on hydroxylated titanium carbide nanosheet: A first-principles study. *J. Hazard. Mater.* **308,** 402–410 (2016).

118. Zhang, Q. *et al.* Efficient phosphate sequestration for water purification by unique sandwich-like MXene/magnetic iron oxide nanocomposites. *Nanoscale* **8,** 7085–7093 (2016).

119. Zou, G. *et al.* Synthesis of urchin-like rutile titania carbon nanocomposites by iron-facilitated phase transformation of MXene for environmental remediation. *J. Mater. Chem. A* **4,** 489–499 (2016).

120. Ren, C. E. *et al.* Charge- and Size-Selective Ion Sieving Through $Ti_3C_2T_x$ MXene Membranes. *J. Phys. Chem. Lett.* **6,** 4026–4031 (2015).

121. Srimuk, P. *et al.* MXene as a novel intercalation-type pseudocapacitive cathode and anode for capacitive deionization. *J. Mater. Chem. A* **4,** 18265–18271 (2016).

122. Liu, H. *et al.* A novel nitrite biosensor based on the direct electrochemistry of hemoglobin immobilized on MXene-Ti_3C_2. *Sens. Actuators B Chem.* **218,** 60–66 (2015).

123. Lorencova, L. *et al.* Electrochemical performance of $Ti_3C_2T_x$ MXene in aqueous media: towards ultrasensitive H_2O_2 sensing. *Electrochimica Acta* **235,** 471–479 (2017).

124. Rakhi, R. B., Nayak, P., Xia, C. & Alshareef, H. N. Novel amperometric glucose biosensor based on MXene nanocomposite. *Sci. Rep.* **6,** (2016).

125. Zhu, X. *et al.* Alkaline intercalation of Ti_3C_2 MXene for simultaneous electrochemical detection of Cd(II), Pb(II), Cu(II) and Hg(II). *Electrochimica Acta* **248,** 46–57 (2017).

126. Chen, J. *et al.* CO_2 and temperature dual responsive "Smart" MXene phases. *Chem Commun* **51,** 314–317 (2015).

127. Xiao, B., Li, Y., Yu, X. & Cheng, J. MXenes: Reusable materials for NH_3 sensor or capturer by controlling the charge injection. *Sens. Actuators B Chem.* **235,** 103–109 (2016).

128. Lee, E. *et al.* Room Temperature Gas Sensing of Two-Dimensional Titanium Carbide (MXene). *ACS Appl. Mater. Interfaces* **9,** 37184–37190 (2017).

129. Ma, Y. *et al.* A highly flexible and sensitive piezoresistive sensor based on MXene with greatly changed interlayer distances. *Nat. Commun.* **8,** (2017).

130. Dong, Y. *et al.* Metallic MXenes: A new family of materials for flexible triboelectric nanogenerators. *Nano Energy* (2017). doi:10.1016/j.nanoen.2017.11.044

131. Han, M. *et al.* Ti_3C_2 MXenes with Modified Surface for High-Performance Electromagnetic Absorption and Shielding in the X-Band. *ACS Appl. Mater. Interfaces* **8,** 21011–21019 (2016).

132. Shahzad, F. *et al.* Electromagnetic interference shielding with 2D transition metal carbides (MXenes). *Science* **353,** 1137–1140 (2016).

133. Seyedin, S., Yanza, E. R. S. & Razal, J. M. Knittable energy storing fiber with high volumetric performance made from predominantly MXene nanosheets. *J. Mater. Chem. A* **5,** 24076–24082 (2017).

134. Hu, M. *et al.* MXene-coated silk-derived carbon cloth toward flexible electrode for supercapacitor application. *J. Energy Chem.* (2017). doi:10.1016/j.jechem.2017.10.030

135. Rasool, K. *et al.* Antibacterial Activity of $Ti_3C_2T_x$ MXene. *ACS Nano* **10,** 3674–3684 (2016).

136. Dai, C. *et al.* Biocompatible 2D Titanium Carbide (MXenes) Composite Nanosheets for pH-Responsive MRI-Guided Tumor Hyperthermia. *Chem. Mater.* **29,** 8637–8652 (2017).

137. Liu, G. *et al.* Surface Modified Ti_3C_2 MXene Nanosheets for Tumor Targeting Photothermal/Photodynamic/Chemo Synergistic Therapy. *ACS Appl. Mater. Interfaces* **9,** 40077–40086 (2017).

138. Xu, B. *et al.* Ultrathin MXene-Micropattern-Based Field-Effect Transistor for Probing Neural Activity. *Adv. Mater.* **28,** 3333–3339 (2016).

139. Ghidiu, M. *et al.* Synthesis and characterization of two-dimensional Nb_4C_3 (MXene). *Chem. Commun.* **50,** 9517 (2014).

140. Warren, B. E. *X-ray diffraction*. (Dover Publications, 1990).

141. Hendricks, S. X-Ray Interference in Partially Ordered Layer Lattices. *J. Chem. Phys.* **10,** 147 (1942).

142. Moore, D. M. & Hower, J. Ordered interstratification of dehydrated and hydrated Na-smectite. *Clays Clay Miner.* **34,** 379–384 (1986).

143. Merkel, S. & Yagi, T. X-ray transparent gasket for diamond anvil cell high pressure experiments. *Rev. Sci. Instrum.* **76,** 046109 (2005).

144. Chipera, S. J., Carey, J. W. & Bish, D. L. Controlled-Humidity XRD Analyses: Application to the Study of Smectite Expansion/Contraction. in *Advances in X-ray Analysis* **39,** 713–722 (Plenum Press, 1997).

145. Jayaraman, A. Diamond anvil cell and high-pressure physical investigations. *Rev. Mod. Phys.* **55,** 65 (1983).

146. Rockland, L. B. Saturated salt solutions for static control of relative humidity between 5° and 40° C. *Anal. Chem.* **32,** 1375–1376 (1960).

147. Mao, H. K., Bell, P. M., Shaner, J. W. & Steinberg, D. J. Specific volume measurements of Cu, Mo, Pd, and Ag and calibration of the ruby R_1 fluorescence pressure gauge from 0.06 to 1 Mbar. *J. Appl. Phys.* **49,** 3276–3283 (1978).

148. Hammersley, A. P., Svensson, S. O., Hanfland, M., Fitch, A. N. & Hausermann, D. Two-dimensional detector software: From real detector to idealised image or two-theta scan. *High Press. Res.* **14,** 235–248 (1996).

149. Pouchou, J. L. & Pichoir, F. Determination of Mass Absorption Coefficients for Soft X-Rays by use of the Electron Microprobe. in *Microbeam Analysis (D. E. Newbury, ed.)* 315 (San Francisco Press, 1988).

150. Ghidiu, M. *et al.* Ion-Exchange and Cation Solvation Reactions in Ti_3C_2 MXene. *Chem. Mater.* **28,** 3507–3514 (2016).

151. Ghidiu, M. *et al.* Alkylammonium Cation Intercalation into Ti_3C_2 (MXene): Effects on Properties and Ion-Exchange Capacity Estimation. *Chem. Mater.* **29,** 1099–1106 (2017).

152. Si, C., Zhou, J. & Sun, Z. Half-Metallic Ferromagnetism and Surface Functionalization-Induced Metal–Insulator Transition in Graphene-like Two-Dimensional Cr_2C Crystals. *ACS Appl. Mater. Interfaces* **7,** 17510–17515 (2015).

153. Pandey, M. & Thygesen, K. S. Two-Dimensional MXenes as Catalysts for Electrochemical Hydrogen Evolution: A Computational Screening Study. *J. Phys. Chem. C* **121,** 13593–13598 (2017).

154. Khazaei, M., Ranjbar, A., Arai, M., Sasaki, T. & Yunoki, S. Electronic properties and applications of MXenes: a theoretical review. *J. Mater. Chem. C* **5,** 2488–2503 (2017).

155. Tan, T. L., Jin, H. M., Sullivan, M. B., Anasori, B. & Gogotsi, Y. High-Throughput Survey of Ordering Configurations in MXene Alloys Across Compositions and Temperatures. *ACS Nano* **11,** 4407–4418 (2017).

156. Srivastava, P., Mishra, A., Mizuseki, H., Lee, K.-R. & Singh, A. K. Mechanistic Insight into the Chemical Exfoliation and Functionalization of Ti_3C_2 MXene. *ACS Appl. Mater. Interfaces* **8,** 24256–24264 (2016).

157. Mishra, A., Srivastava, P., Mizuseki, H., Lee, K.-R. & Singh, A. K. Isolation of pristine MXene from Nb_4AlC_3 MAX phase: a first-principles study. *Phys Chem Chem Phys* **18,** 11073–11080 (2016).

158. Xie, Y. *et al.* Role of Surface Structure on Li-Ion Energy Storage Capacity of Two-Dimensional Transition-Metal Carbides. *J. Am. Chem. Soc.* **136,** 6385–6394 (2014).

159. Borysiuk, V. N., Mochalin, V. N. & Gogotsi, Y. Molecular dynamic study of the mechanical properties of two-dimensional titanium carbides $Ti_{n+1}C_n$ (MXenes). *Nanotechnology* **26,** 265705 (2015).

160. Bak, S.-M. *et al.* Na-Ion Intercalation and Charge Storage Mechanism in 2D Vanadium Carbide. *Adv. Energy Mater.* **7,** 1700959 (2017).

161. Miranda, A., Halim, J., Barsoum, M. W. & Lorke, A. Electronic properties of freestanding $Ti_3C_2T_x$ MXene monolayers. *Appl. Phys. Lett.* **108,** 033102 (2016).

162. Lipatov, A. *et al.* Effect of Synthesis on Quality, Electronic Properties and Environmental Stability of Individual Monolayer Ti_3C_2 MXene Flakes. *Adv. Electron. Mater.* 1600255 (2016). doi:10.1002/aelm.201600255

163. Li, C., Kota, S., Hu, C. & Barsoum, M. W. On the Synthesis of Low-Cost, Titanium-Based MXenes. *J. Ceram. Sci. Technol.* **7,** 301–306 (2016).

164. Kim, S. J. *et al.* High mass loading, binder-free MXene anodes for high areal capacity Li-ion batteries. *Electrochimica Acta* **163,** 246–251 (2015).

165. Zhao, X. *et al.* Fabrication of layered Ti_3C_2 with an accordion-like structure as a potential cathode material for high performance lithium–sulfur batteries. *J Mater Chem A* **3,** 7870–7876 (2015).

166. Hishiyama, Y. & Nakamura, M. X-ray Diffraction in Oriented Carbon Films with Turbostratic Structure. *Carbon* **33,** 1399–1403 (1995).

167. Li, Z. Q., Lu, C. J., Xia, Z. P., Zhou, Y. & Luo, Z. X-ray diffraction patterns of graphite and turbostratic carbon. *Carbon* **45,** 1686–1695 (2007).

168. Joensen, P., Crozier, E. D., Alberding, N. & Frindt, R. F. A study of single-layer and restacked MoS2 by X-ray diffraction and X-ray absorption spectroscopy. *J. Phys. C Solid State Phys.* **20,** 4043 (1987).

169. Yang, D., Sandoval, S. J., Divigalpitiya, W. M. R., Irwin, J. C. & Frindt, R. F. Structure of single-molecular-layer MoS 2. *Phys. Rev. B* **43,** 12053 (1991).

170. Ghidiu, M. & Barsoum, M. W. The {110} reflection in X-ray diffraction of MXene films: Misinterpretation and measurement via non-standard orientation. *J. Am. Ceram. Soc.* **100,** 5395–5399 (2017).

171. Chen, B., Chang, F., Yang, J., Tang, H. & Li, C. Microstructure and phase transformation of Ti_3AC_2 (A = Al, Si) in hydrofluoric acid solution: Microstructure and phase transformation…. *Cryst. Res. Technol.* **49,** 813–819 (2014).

172. Barnes, W. H. The Crystal Structure of Ice between 0 degrees C. and-183 degrees C. *Proc. R. Soc. Lond. Ser. Contain. Pap. Math. Phys. Character* **125,** 670–693 (1929).

173. Tambach, T. J., Bolhuis, P. G., Hensen, E. J. M. & Smit, B. Hysteresis in Clay Swelling Induced by Hydrogen Bonding: Accurate Prediction of Swelling States. *Langmuir* **22,** 1223–1234 (2006).

174. Salles, F. *et al.* A calorimetric study of mesoscopic swelling and hydration sequence in solid Na-montmorillonite. *Appl. Clay Sci.* **39,** 186–201 (2008).

175. Tajeddine, L. *et al.* Hydration–dehydration behavior and thermodynamics of MX-80 montmorillonite studied using thermal analysis. *Thermochim. Acta* **604,** 83–93 (2015).

176. Foo, M. L., Klimczuk, T. & Cava, R. J. Hydration phase diagram for sodium cobalt oxide Na0.3CoO2·yH2O. *Mater. Res. Bull.* **40,** 665–670 (2005).

177. Johnston, D. Ambient temperature phase relations in the system Na1/3(H2O)yTaS2 (0<y<2). *Mater. Res. Bull.* **17,** 13–23 (1982).

178. H.J. Bray & S.A.T. Redfern. Kinetics of dehydration of Ca-montmorillonite. *Phys Chem Miner.* **26,** 591–600 (1999).

179. A. Lerf & R. Schöllhorn. Solvation Reactions of Layered Ternary Sulfides AxTiS2, AxNbS2, and AxTaS2. *Inorg. Chem.* **16,** 2950–2956 (1977).

180. Talyzin, A. V. *et al.* Colossal Pressure-Induced Lattice Expansion of Graphite Oxide in the Presence of Water. *Angew. Chem. Int. Ed.* **47,** 8268–8271 (2008).

181. You, S. *et al.* Pressure-Induced Water Insertion in Synthetic Clays. *Angew. Chem.* **125,** 3983–3987 (2013).

182. Nakano, S., Sasaki, T., Takemura, K. & Watanabe, M. Pressure-induced intercalation of alcohol molecules into a layered titanate. *Chem. Mater.* **10,** 2044–2046 (1998).

183. Talyzin, A. V., Sundqvist, B., Szabó, T., Dékány, I. & Dmitriev, V. Pressure-Induced Insertion of Liquid Alcohols into Graphite Oxide Structure. *J. Am. Chem. Soc.* **131,** 18445–18449 (2009).

184. Ortiz, A. U., Boutin, A., Gagnon, K. J., Clearfield, A. & Coudert, F.-X. Remarkable Pressure Responses of Metal–Organic Frameworks: Proton Transfer and Linker Coiling in Zinc Alkyl Gates. *J. Am. Chem. Soc.* **136,** 11540–11545 (2014).

185. Vakarin, E. V. & Talyzin, A. V. On the mechanism of negative compressibility in layered compounds. *Chem. Phys.* **369,** 19–21 (2010).

186. Lee, Y., Hriljac, J. A., Vogt, T., Parise, J. B. & Artioli, G. First structural investigation of a super-hydrated zeolite. *J. Am. Chem. Soc.* **123,** 12732–12733 (2001).

187. Mariano, M. *et al.* Solution-processed titanium carbide MXene films examined as highly transparent conductors. *Nanoscale* **8,** 16371–16378 (2016).

188. You, S. *et al.* Pressure-Induced Water Insertion in Synthetic Clays. *Angew. Chem. Int. Ed.* **52,** 3891–3895 (2013).

189. Satheeshkumar, E. *et al.* One-step Solution Processing of Ag, Au and Pd@MXene Hybrids for SERS. *Sci. Rep.* **6,** (2016).

190. Wang, L. *et al.* Rational control of the interlayer space inside two-dimensional titanium carbides for highly efficient uranium removal and imprisonment. *Chem. Commun.* **53,** 12084–12087 (2017).

191. Ide, Y., Sadakane, M., Sano, T. & Ogawa, M. Functionalization of Layered Titanates. *J. Nanosci. Nanotechnol.* **14,** 2135–2147 (2014).

192. Dékány, I., Krüger-Grasser, R. & Weiss, A. Selective liquid sorption properties of hydrophobized graphite oxide nanostructures. *Colloid Polym. Sci.* **276,** 570–576 (1998).

193. Volzone, C., Rinaldi, J. O. & Ortiga, J. Retention of gases by hexadecyltrimethylammonium–montmorillonite clays. *J. Environ. Manage.* **79,** 247–252 (2006).

194. Urbán, M., Kónya, Z., Méhn, D., Zhu, J. & Kiricsi, I. Mesoporous silicates as nanoreactors for synthesis of carbon nanotubes. *Phys. Chem. Commun.* **5,** 138–141 (2002).

195. Lagaly, G. t & Weiss, A. Anordnung und Orientierung kationischer Tenside auf Silicatoberflächen. *Kolloid-Z. Z. Für Polym.* **243,** 48–55 (1971).

196. Vidal, N. & Volzone, C. Influence of Organobentonite Structure on Toluene Adsorption from Water Solution. *Mater. Res.* **15,** 944–953 (2012).

197. Lagaly, G. Interaction of alkylamines with different types of layered compounds. *Solid State Ion.* **22,** 43–51 (1986).

198. Lagaly, G., Fernandez Gonzalez, M. & Weiss, A. Problems in layer-charge determination of montmorillonites. *Clay Miner.* **11,** 173–187 (1976).

199. Wang, X. *et al.* Pseudocapacitance of MXene nanosheets for high-power sodium-ion hybrid capacitors. *Nat. Commun.* **6,** 6544 (2015).

200. Lagaly, G. Characterization of clays by organic compounds. *Clay Miner.* 1–21 (1981).

201. Ogawa, M., Ishii, T., Miyamoto, N. & Kuroda, K. Photocontrol of the Basal Spacing of Azobenzene–Magadiite Intercalation Compound. *Adv. Mater.* **13,** 1107–1109 (2001).

202. Okuno, S. & Matsubayashi, G. Intercalation of Ferrocenylalkylammonium Cations into the Layered Lattice of $VOPO_4$. *J. Chem. Soc. Dalton Trans.* 2441–2444 (1992).

203. Sun, R. *et al.* Highly Conductive Transition Metal Carbide/Carbonitride(MXene)@polystyrene Nanocomposites Fabricated by Electrostatic Assembly for Highly Efficient Electromagnetic Interference Shielding. *Adv. Funct. Mater.* **27,** 1702807 (2017).

204. Naguib, M. *et al.* $Ti_3C_2T_x$ (MXene)–polyacrylamide nanocomposite films. *RSC Adv.* **6,** 72069–72073 (2016).

205. Zhang, H. *et al.* Preparation, mechanical and anti-friction performance of MXene/polymer composites. *Mater. Des.* **92,** 682–689 (2016).

206. Hong Ng, V. M. *et al.* Recent progress in layered transition metal carbides and/or nitrides (MXenes) and their composites: synthesis and applications. *J Mater Chem A* **5,** 3039–3068 (2017).

VITA

Michael Ghidiu
email: mghidiu@gmail.com

EDUCATION

Drexel University, Philadelphia, PA, USA 9/2013–6/2018
Ph.D. Materials Science & Engineering
University of Delaware, Newark, DE, USA 9/2008–5/2012
B.S. Chemistry

AWARDS

National Science Foundation Graduate Research Fellowship 3/2015
Drexel Provost Fellowship 9/2013

PRESENTATIONS

American Chemical Society Meeting
Talk 8/2016
International Conf. and Expo on Advanced Ceramics and Composites
Talk 1/2015
Materials Research Society Meeting
Poster 4/2015

PUBLICATIONS

1. Ghidiu, M.; Kota, S.; Drozd, V.; Barsoum, M.W. *Science Advances* **2018**, *4* (1).
2. Ghidiu, M.; Barsoum, M.W. *J. Am. Cer. Soc*. **2017**, *100* (12), pp 5395–5399.
3. Ghidiu, M.; Kota, S.; Halim, J.; Sherwood, A. W.; Nedfors, N.; Rosen, J.; Mochalin, V. N.; Barsoum, M. W. *Chemistry of Materials* **2017**, *29* (3), pp 1099–1106.
4. Zhao, M.-Q.; Torelli, M.; Ren, C. E.; Ghidiu, M.; Ling, Z.; Anasori, B.; Barsoum, M. W.; Gogotsi, Y. *Nano Energy* **2016**, *30*, 603–613.
5. Zhang, C. J.; Kim, S. J.; Ghidiu, M.; Zhao, M.-Q.; Barsoum, M. W.; Nicolosi, V.; Gogotsi, Y. *Advanced Functional Materials* **2016**, *26* (23), 4143–4151.
6. Yang, J.; Naguib, M.; Ghidiu, M.; Pan, L.-M.; Gu, J.; Nanda, J.; Halim, J.; Gogotsi, Y.; Barsoum, M. W. *Journal of the American Ceramic Society* **2016**, *99* (2), 660–666.
7. Hope, M. A.; Forse, A. C.; Griffith, K. J.; Lukatskaya, M. R.; Ghidiu, M.; Gogotsi, Y.; Grey, C. P. *Physical Chemistry Chemical Physics* **2016**, *18* (7), 5099–5102.
8. Ghidiu, M.; Halim, J.; Kota, S.; Bish, D.; Gogotsi, Y.; Barsoum, M. W. *Chemistry of Materials* **2016**, *28* (10), 3507–3514.
9. Dillon, A. D.; Ghidiu, M. J.; Krick, A. L.; Griggs, J.; May, S. J.; Gogotsi, Y.; Barsoum, M. W.; Fafarman, A. T. *Advanced Functional Materials* **2016**, *26* (23), 4162–4168.
10. Bentzel, G. W.; Ghidiu, M.; Griggs, J.; Lang, A.; Barsoum, M. W. *Corrosion Science* **2016**, *111*, 568–573.
11. Zhao, M.-Q.; Sedran, M.; Ling, Z.; Lukatskaya, M. R.; Mashtalir, O.; Ghidiu, M.; Dyatkin, B.; Tallman, D. J.; Djenizian, T.; Barsoum, M. W. *Angewandte Chemie International Edition* **2015**, *54* (16), 4810–4814.
12. Bentzel, G. W.; Ghidiu, M.; Anasori, B.; Barsoum, M. W. *Journal of the European Ceramic Society* **2015**, *35* (15), 4107–4114.

13. Pistner, A. J.; Lutterman, D. A.; Ghidiu, M. J.; Walker, E.; Yap, G. P.; Rosenthal, J. *The Journal of Physical Chemistry C* **2014**, *118* (26), 14124–14132.
14. Ghidiu, M.; Naguib, M.; Shi, C.; Mashtalir, O.; Pan, L. M.; Zhang, B.; Yang, J.; Gogotsi, Y.; Billinge, S. J.; Barsoum, M. W. *Chemical Communications* **2014**, *50* (67), 9517–9520.
15. Ghidiu, M.; Lukatskaya, M. R.; Zhao, M.-Q.; Gogotsi, Y.; Barsoum, M. W. *Nature* **2014**, *516* (7529), 78–81.
16. Pistner, A. J.; Lutterman, D. A.; Ghidiu, M. J.; Ma, Y.-Z.; Rosenthal, J. *Journal of the American Chemical Society* **2013**, *135* (17), 6601–6607.
17. Ghidiu, M. J.; Pistner, A. J.; Yap, G. P.; Lutterman, D. A.; Rosenthal, J. *Organometallics* **2013**, *32* (18), 5026–5029.